

**ÉCOLE DOCTORALE DE PHYSIQUE ET CHIMIE PHYSIQUE (ED182)**  
**IPCMS - UMR 7504 CNRS - Unistra**

# THÈSE

présentée par :

**Yaowei Hu**

soutenue le **3 mai 2022**

pour obtenir le grade de : **Docteur de l'université de Strasbourg**

Discipline/ Spécialité : **Physique - Chimie physique**

**Ultrafast electron microscopy of transient states  
in nanomaterials**

**THÈSE dirigée par :**  
**BANHART, Florian**

Professeur, Université de Strasbourg

**RAPPORTEURS :**  
**KAISER, Ute**  
**ALLOYEAU, Damien**

Professeur, Université d'Ulm  
Directeur de recherches, Université de Paris VII

---

**Examineur :**

**LEONARD, Jérémie**

Directeur de recherches, CNRS



**Land is apart but wind and moon are shared.**

**(山川异域 风月同天)**

## Acknowledgment

First of all, I would like to thank my supervisor Prof. Florian Banhart for giving me this position. I am very grateful for his guidelines, advices and patience. Furthermore, he always can help me deal with all the administrative program. I want to express my warmest thanks. At the same time, I need also thank Prof. Thomas W. Ebbesen for helping me apply my thesis scholarship.

I want to thank Prof. Ute Kaiser, Dr. Damien Alloyeau, and Dr. Jérémie Léonard for accepting to be my thesis jury members.

I would also like to thank Dr. Matthieu Picher. He always gives us good technical support. I am very grateful to him for giving me a solid introductory training in UTEM. I want to express my warmest thanks.

I also want to thank Prof. Stefan Haacke and Dr. Marc Schmutz for helping me finish my twice mid-defense documents.

I want to thank our colleagues in Bordeaux University. They provided very good quality SCO samples. I want to express gratitude to Dr. Guillaume Chastanet, Dr. Eric Freysz, Dr. Marlene Palluel, Dr. Nathalie Daro, and Prof. Cristian Enachescu.

I would also like to thank Dr. Maciej Lorenc for sharing the  $Ti_3O_5$  particle with us, and Dr. Maciej Lorenc gave us an inspired lecture in structural dynamics.

I would like to thank all the members of the IPCMS DSI department who helped me. I want to thank our former colleagues, Dr. Jun Sun, and Dr. Amir Khammari.

I also would like to thank my friends at the Explanade campus (Dr. Yongxiang Zheng) and Cronengbourg campus (Dr. Wenzhi Wang, Hui Zhang).

At last, I want to thank my family for giving me unconditional support.

## Contents

Acknowledgment.....	I
Contents .....	III
Chapter 1 .....	1
Introduction.....	1
Chapter 2.....	3
Ultrafast dynamics in transmission electron microscopy.....	3
2.1 The pump-probe method .....	4
2.2 Ultrafast transmission electron microscopy and nano-imaging techniques.....	6
UTEM in material science .....	10
UTEM in nano-optics .....	13
Electron pulse compression and attosecond electron pulses .....	15
2.3 Phase transitions in nanomaterials .....	16
Chapter 3.....	19
Ultrafast Transmission Electron Microscope .....	19
3.1 Transmission Electron Microscopy with short electron pulses.....	20
Properties of the electron pulses in the beam .....	20
Electron gun and Acceleration tube.....	22
Condenser lens system.....	25
Imaging system.....	27
Electron energy loss spectroscopy.....	28
3.2 Ultrafast laser pulse technique.....	30
The Ultrafast Transmission Electron Microscope used in this work .....	31
Chapter 4.....	37
Time-resolved experiments on single particles behavior of spin-crossover compounds .....	37
4.1 Crystal structure and molecular description of SCO materials .....	38
4.2 Microscopic models for spin-crossover compounds.....	40

The elastic model.....	41
4.3 Experimental results.....	42
Single SCO nanoparticle measurement in TEM.....	43
Single SCO nanoparticle behavior under continuous external heating.....	44
Radiation damage effects in SCO particles under the electron beam.....	48
4.4 Time-resolved measurements of single spin-crossover nanoparticles.....	49
Time-resolved measurements of SCO.....	50
Time-resolved measurements of SCO@AuNPs.....	53
Discussion of the results on SCO.....	56
Time-resolved Optical spectroscopy.....	57
Simulation of the plasmonic light field inside the composite particles Au@SCO.....	58
Simulation of collective effects due to elastic interactions in the SCO particles.....	61
Oscillations in the phase transition of SCO.....	62
4.5 Conclusion.....	64
Chapter 5.....	65
Photo-reversible phase transition in $Ti_3O_5$ .....	65
5.1 Crystal structure and electronic states in $Ti_3O_5$ .....	66
5.2 Thermal phase transformations in $Ti_3O_5$ observed by TEM.....	69
5.3 Photo-excited phase transition in TEM.....	75
5.4 Previous time-resolved experiments by optical techniques.....	80
Chapter 6.....	82
Other projects in UTEM.....	82
6.1 Melting processes in core-shell nanoparticles.....	83
6.2 Photothermal reduction of iron oxide nanocrystals.....	84
6.3 Reversible redox reaction in ceria nanoparticles.....	88
6.4 Ultrafast TEM using coherent electron pulses.....	91
PINEM experiment.....	91
Chapter 7.....	93
Conclusion of this thesis.....	93

Pending work.....	95
Résumé de thèse en français.....	96
Introduction .....	96
Dynamique des transformations dans des nanoparticules du type spin-crossover (SCO) 97	
Transitions de phase dans $Ti_3O_5$ sous impulsions laser étudiées par microscopie électronique.....	100
Conclusion .....	102
References .....	103

## Chapter 1

### Introduction

The timescales of dynamic processes in nature span over many orders of magnitude. While the timescale of biological and geological processes may range from days to years, the dynamics of electronic, atomic, and molecular processes appear in the sub-millisecond regime, such as electron jumping [1] or protein folding [2].

To give an overview of the large range of timescales of microscopic dynamics, photoexcitation in isolated atoms or diatomic molecules requires only 10-100 attoseconds [1]. This short timescale originates from the low mass of the electron, the high speed of light and the simplicity of the atomic structure. However, in more complex functional systems, dynamic processes may happen within a few femtoseconds to milliseconds [3]. For example, after a laser trigger, the transfer time of localized Mn-d electrons to itinerant carriers happens within less than 20 fs in a GaMnAs film [4]; the spin-orbital coupling is at the timescale of around 1 ps [3-5], and the successive lattice distortion via electron-phonon interaction happens within several ps [3-5]. The fluctuation of atomic rearrangements that promote phase transitions happens from tens of femtoseconds to hundreds of picoseconds [6]. Especially, between solid-state grains or in nanocrystalline materials, complex chemical reactions require bond breaking, atomic diffusion processes and bond formation, which takes from nanoseconds to microseconds [7].

Even in living organisms, the ultrafast dynamics is observed as a response to an external stimulus [2]. Fast vibrational or rotational motion and displacements in condensed matter play an important role [6, 8] because these physical processes provide the information for the understanding of collective excitations of atoms, molecular realignments as well as nucleation or growth phenomena [6]. However these dynamic processes happen between  $10^{-10}$ s and  $10^{-15}$ s [6, 8] so that it is impossible to study dynamics with continuous beams to probe transient states and measure the timescales of the transformations.

Transmission electron microscopy (TEM) is a powerful tool to explore the nanoscale [9]. After the correction of spherical aberration was employed, detailed imaging at the atomic scale is easily realized through TEM. Recently, a new scientific community formed in ultrafast transmission electron microscopy, which combines the nanoscale resolution of TEM and ultrafast optical techniques in order to achieve high spatial resolution and time resolution at same time. In 2005, Zewail et al. proposed a new stroboscopic method and boosted the field

[10]. In follow-up works, they improved the spatial resolution of ultrafast electron imaging to almost the atomic scale and the temporal resolution to the sub-picosecond [11]. After this pioneering work, several research groups have successfully been applying the powerful technique of ultrafast electron microscopy [10,11]. The basics of ultrafast TEM will be presented in chapter 2 of this thesis.

In 2014, a new setup of Ultrafast transmission electron microscopy (UTEM) has been installed at the IPCMS. After former colleagues' instrumental development, this UTEM can work at both the single-shot mode and stroboscopic modes. The time scale accessible in the stroboscopic mode is from 500 fs to 3 ns. In the single-shot mode, the time scale spans from 7 ns to more than 50 ms. Recently, we synchronized two nanosecond lasers and extended the timescale of stroboscopic experiments from 7 ns to 50 ms. Results achieved with this instrumental improvement will be presented in chapter 3 of this thesis.

I registered at the University of Strasbourg in November 2018, first as a PhD student at ISIS. In the beginning of 2019, I visited the UTEM group and decided to join Florian Banhart's group. M. Picher instructed me in the technical details and experimental procedures in UTEM. After that, under F. Banhart's guidelines, I have explored several ideas of new experiments in ultrafast electron microscopy of transient states in nanomaterials. At the beginning, we tried an experiment in photon induced near-field electron microscopy (PINEM), but results turned out not to be innovative enough compared with those already reported in the literature. In the following year, we tried a study on melting dynamics in nano-systems through ultrafast electron diffraction but the experimental difficulties were discouraging. In another attempt, we studied the reversible transition between  $\text{CeO}_2$  and  $\text{Ce}_2\text{O}_3$  through time-resolved electron energy loss spectroscopy (EELS). Furthermore, single-shot EELS on  $\text{Fe}_2\text{O}_3$  nanocrystals in the nanobeam diffraction (NBD) mode was tried by us. All of these preliminary studies, which did not lead to publishable results immediately, will be presented in chapter 6.

After these series of studies, I shaped my skills in UTEM and structural dynamics. Finally, in the last two years, we found the ideal systems for stroboscopic experiments. Photo-induced structural transformations of spin-crossover (SCO) nanoparticles and  $\text{Ti}_3\text{O}_5$  particles delivered new insights into the structural dynamics of nanomaterials. As the actual work of my thesis, these results will be presented in chapter 4 and chapter 5.

## Chapter 2

### Ultrafast dynamics in transmission electron microscopy

#### Contents

<a href="#">Chapter 2</a> .....	3
<a href="#">Ultrafast dynamics in transmission electron microscopy</a> .....	3
<a href="#">2.1 The pump-probe method</a> .....	4
<a href="#">2.2 Ultrafast transmission electron microscopy and nano-imaging techniques</a> .....	6
<a href="#">UTEM in material science</a> .....	10
<a href="#">UTEM in nano-optics</a> .....	13
<a href="#">Electron pulse compression and attosecond electron pulses</a> .....	15
<a href="#">2.3 Phase transition in nanomaterials</a> .....	16

The second chapter aims at giving a broad overview of the ultrafast processes in nanomaterials, starting with a brief historical review of different pump-probe techniques, and then introducing some of the key concepts in ultrafast transmission electron microscopy. After a description of the historical developments, the state of the art is enumerated with application examples from the literature, giving the context of this work.

## 2.1 The pump-probe method

With pulsed lasers, after inventing mode-locking and Q-switching techniques, it is possible to study ultrafast/fast processes. Short laser pulses or laser-induced electron pulses can probe the electron spins, atom dynamics and molecular vibrations. Laser pulses can excite electronic transitions or induce atom rearrangements up to phase transitions or melting. Probing of transition states can provide real time data to understand the dynamics of transitions. The pump-probe principle is shown in fig. 2.1. One laser pulse is used to excite the sample, and another pulse detects the transient properties and dynamics. A. Zewail did pioneer work, and received the Noble Prize for the contributions in femtochemistry which is based on pump-probe methods [8].

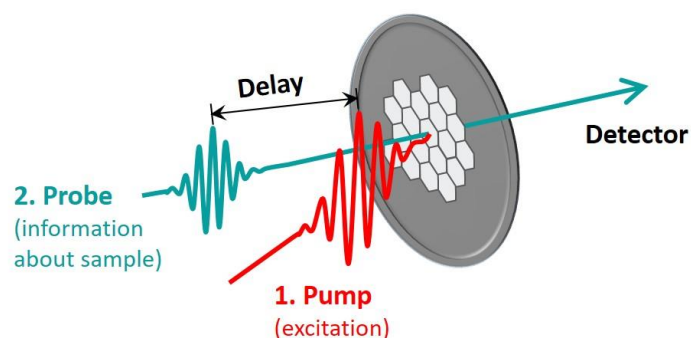


Fig. 2.1 Schematic of pump-probe method: 1. The pump pulse modulates the specimen to the excited state or a new state; 2. The probe pulse detects the transient state after an adjustable delay  $\Delta t$ .

Different wavelength and timescale response of different materials gives detailed insight into dynamic processes [3]. In 1995, Beaurepaire et al reported the ultrafast spin dynamics in ferromagnetic nickel which has been studied by the pump-probe method with a time resolution of 60 fs at a wavelength of 620 nm [12]. For longer wavelengths, THz pulses can excite quasi particles such as resonant phonons [13] and electromagnon excitations [14]. Recently, Schlauderer et al. reported the abruptly changing magnetic anisotropy and ballistic spin motion in antiferromagnetic  $\text{TmFeO}_3$  pumped by THz pulses and probed by near-infrared pulses with wavelength 808 nm and pulse duration 33 fs [15]. Cavalleria et al. used mid-infrared laser pulses with 14  $\mu\text{m}$  wavelength to excite lattice displacements through nonlinear phononics [16], where they measured the time-dependent anisotropic refractivity of the sample with near-infrared pulses. Also they reported photo-induced superconductivity by mid-infrared pulses, and measured the optical conductivity in the mid infrared [17, 18].

In 1991, Murnance et al. reported a technique of an intense laser pulse-induced high temperature plasma emitting ultrafast X-ray pulses [19]. Although the X-ray pulse brightness is low in this method, Rischel et al. did a pioneer work where femtosecond X-ray diffraction detected laser-heated transitions of cadmium crystals to a disordered state [20]. Based on the radiation from a relativistic electron beam through an undulator magnet, accelerator-based sources can generate short and bright X-ray pulses which can be used for femtosecond X-ray spectroscopies [21 - 25]. Synchrotron radiation beams of the third generation synchrotrons (European Synchrotron Radiation Facility, Grenoble) provide 20 ps pulses in uniform mode (quasi-continuous mode) and 73 ps in the single bunch mode [21]. X-ray pulses from free electron lasers reach the 10 fs scale [22, 23]. According to the measurement requirements, these techniques of X-ray pulses can provide information on the dynamics of electronic structures [3], atom rearrangements [3, 25], demagnetization [23] and magnetization switching processes [24]. Arguably, ultrafast X-ray diffraction is one of the most promising techniques to characterize materials. In fig. 2.2, the example of an X-ray probed photo-activated light sensitive protein is shown.

However, X-ray sources are very large facilities. Normally, the synchrotron radiation is produced in electron storage rings with 150 m diameter and 5 m undulators. The X-ray free electron laser is a linear accelerator with 1000 m length and 100 m undulators [2, 23]. There are only a few facilities of this type and access for users is limited to short periods of measurements.

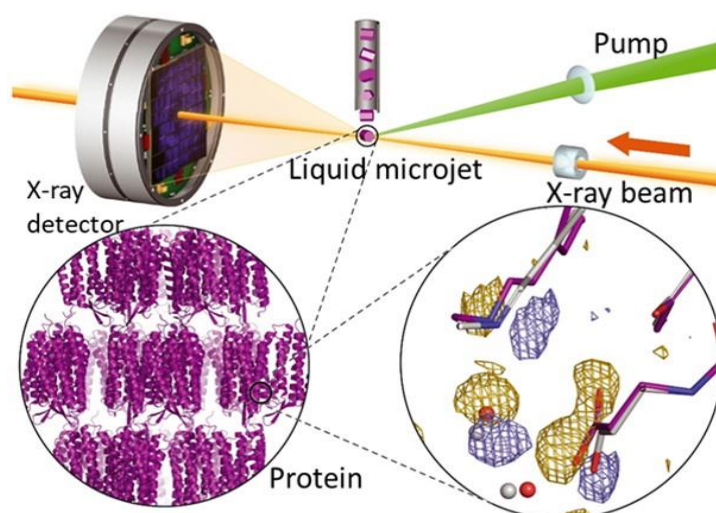


Fig. 2.2. Examples of a pump-probe technique. Time-resolved X-ray crystallography study of a protein: In this process, the droplet with microcrystals is at the overlapping point between the X-ray beam and the pump laser beam; Adapted from Brändén et al [2].

## 2.2 Ultrafast transmission electron microscopy and nano-imaging techniques

In this chapter, the historical development of ultrafast or dynamic TEM and some selected applications will be presented. UTEM combines the advantages of atom scale resolution [26] and pico- to femtosecond time resolution [27]. This gives us a chance to study electronic collective motions, lattice vibrations and phase transitions [28 - 32].

Fig. 2.3 presents the schematic of pump-probe method in TEM.

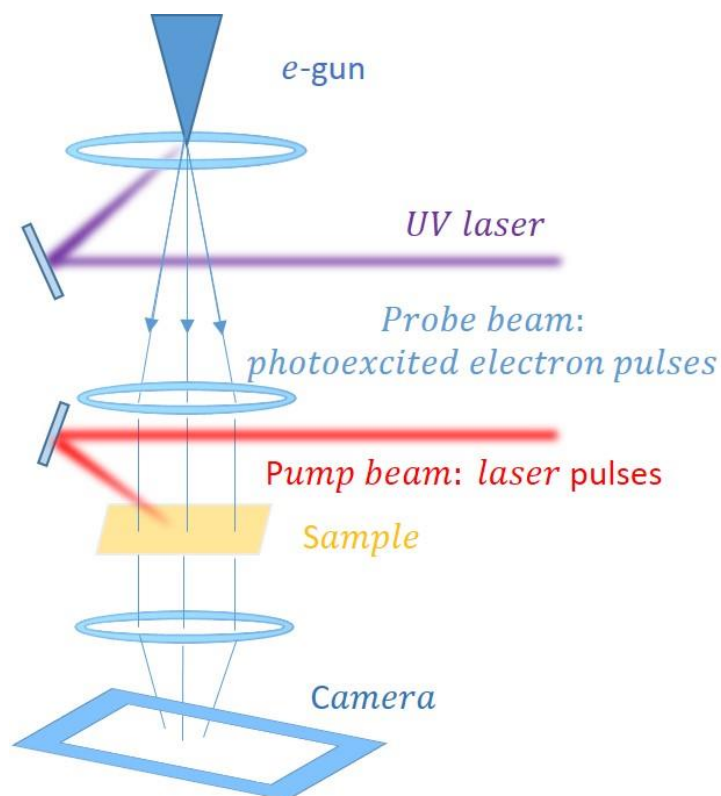


Fig. 2.3 The UTEM technique: one laser beam (red) is used to excite the sample; another UV laser beam (violet) is used to induce photoelectron pulses, which are used to probe the excited sample; the transmitted electrons are focused and recorded by a camera.

In 1980, Bostanjoglo et al. reported a method of TEM with 30 ns time resolution and realized bright field imaging with electron pulses [31]. The photo in fig. 2.4(a) shows the setup which was built by O. Bostanjoglo in the 1980s. Dömer et al. reported 10 ns electron pulses and 200 nm spatial resolution [33]. In these early works, Bostanjoglo and Dömer focused attention on the single-shot method which can produce an image with one intense electron pulse. Based on the pioneering work of O. Bostanjoglo, researchers from the Lawrence Livermore National Laboratory (LLNL) have further improved the illumination system of the dynamic TEM (DTEM). As shown in fig. 2.4 (b) and (c), the single shot mode achieved intense electron pulses with  $10^7$  counts in 30 ns pulses at LLNL [34]. In 2010, Reed et al. added an extra condenser lens below the acceleration tube and above the C1 lens, as shown in fig. 2.4 (d) and (e) [35].

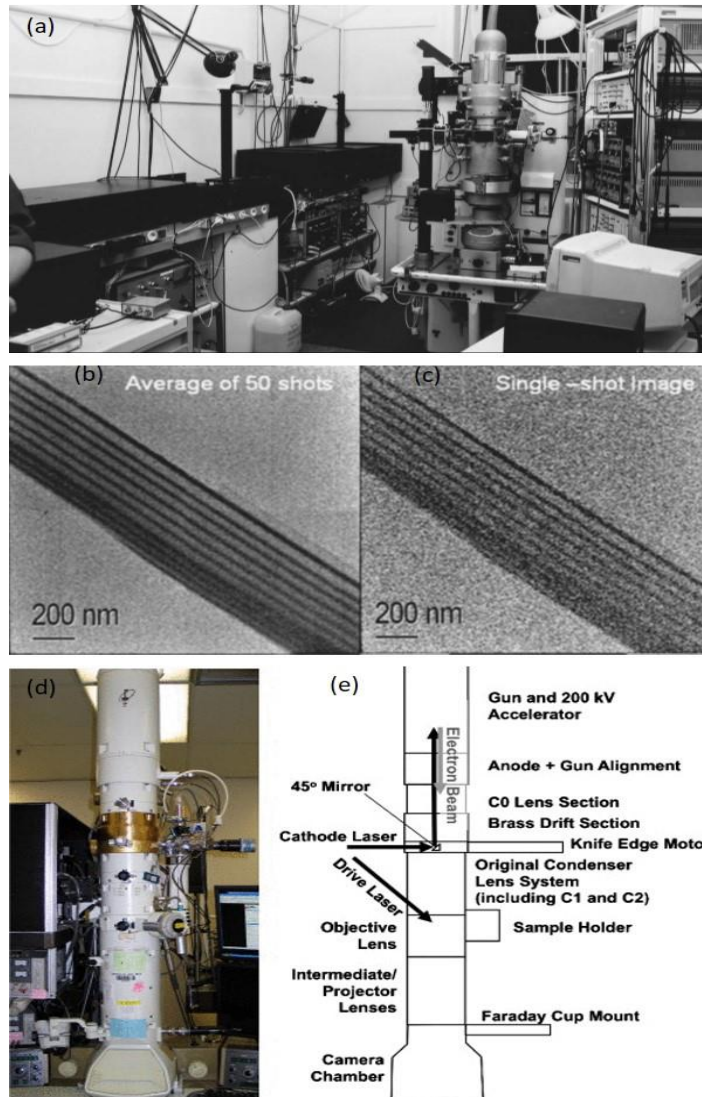


Fig. 2.4 (a) shows the first setup of a time-resolved TEM by Bostanjoglo in Berlin [10]; (b) shows images of an Au/C multilayer foil cross section with 50 DTEM pulses; (c) shows the corresponding image with one single pulse; (d) shows the photo of an improved time-resolved TEM setup in LLNL; (e) shows the schematic of this TEM with a  $C_0$  lens. (a) is adapted from Arbouet et al [10]; (b) and (c) are adapted from LaGrange et al [34]; (d) and (f) are adapted from Reed et al [35].

The  $C_0$  lens further increases the electron counts in each pulse ( $2 \times 10^9$  counts in 15 ns pulses) [10, 35]. In 2011, the movie-mode DTEM which can generate a sequence of images within 1  $\mu$ s was developed at LLNL [36, 37]. The movie-mode DTEM can record series of images of an irreversible process which happens within 10 ns  $\sim$  1 s [37].

The single-shot mode is necessary when irreversible transformations of objects such as chemical reactions or phase transformations are studied. The electron pulse of a DTEM contains  $> 10^7$  electron counts, which are causing a strong Coulomb repulsion between these electrons inside the propagating electron bunch. So the spatio-temporal and energy resolution is getting deteriorated by repulsion effects during the propagation.

Zewail and coworkers proposed a new method, ultrafast transmission electron microscopy (UTEM), where a femtosecond laser pulse generates an electron pulse which includes only one or a few electrons. In contrast to DTEM, where one intense pulse is used for studying irreversible transformations, UTEM is used in a stroboscopic approach which is limited to reversible transformations. Although, in UTEM, the images are recorded by summing up millions of pump-probe cycles, the time resolution of UTEM improved by 4 - 5 orders of magnitude compared with DTEM [38], as shown in fig. 2.5. The spatial resolution is also further improved as shown in fig. 2.6.

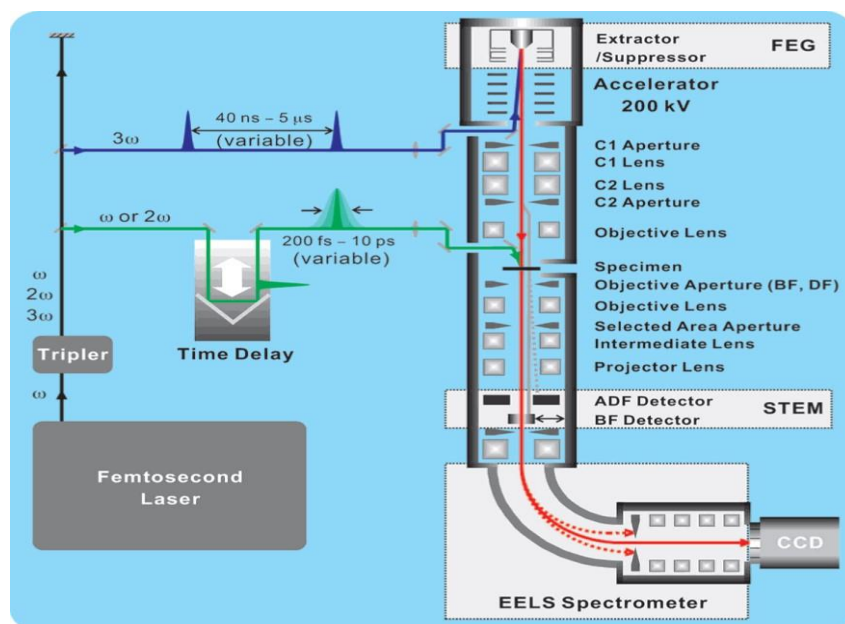


Fig. 2.5 The UTEM setup at Caltech: the instrument is based on a 200 kV TEM with a field emission gun assembly but using a LaB<sub>6</sub> filament; the femtosecond laser creates ultrashort pulses of up to 10  $\mu$ J at 1030 nm with variable repetition rate (200 kHz to 25 MHz) and pulse duration (200 fs to 10 ps) [38]. This picture is adapted from Park et al. [38].

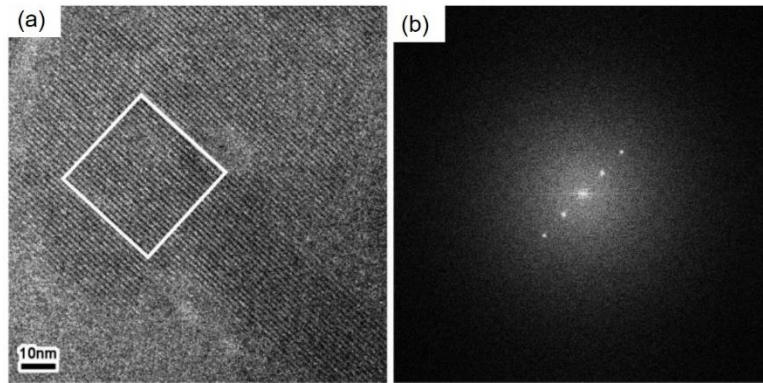


Fig. 2.6 UTEM images of an organometallic crystal of chlorinated copper phthalocyanine with atomic scale resolution in real space and reciprocal space, taken with photoelectron pulses: (a) high-resolution image; (b) the diffractogram was obtained by the Fourier transform of the image. This picture is adapted from Park et al. [38].

### UTEM in material science

Since the UTEM was built in 2005, high-resolution in real space and reciprocal space can be achieved at the picosecond timescale. This is an important improvement for studying reversible ultrafast processes, such as photo-induced phase transitions in nanomaterials [39] and lattice compression/expansion [40], ranging from sub-picoseconds to several nanoseconds. DTEM has been further improved recently, and especially after adding the lens C0, the ability of imaging in DTEM is sufficient to image and analyze irreversible processes [7].

In 2007, Baum et al. studied the reversible phase transition of single crystal vanadium dioxide through monitoring Bragg diffractions in UTEM, and revealed the vanadium-vanadium bond dilation at the fs timescale, atomic displacements within picoseconds, and the shear motion of sound waves within hundreds of picoseconds [39]. As shown in fig. 2.7 (a) and (b), the diffraction intensity of the (6 0 6) spot abruptly jumps after laser trigger, and the (0 9 1) spot displayed another dynamic process than the (6 0 6) spot.

Carbone et al. observed the coherent lattice motions and contractions which are followed by a large expansion [40]. After ultrafast laser excitation of graphite, the

excited carriers reach the equilibrium in less than 1 ps. As shown in fig. 2.7 (c) and (d), the velocity of the expansion depends on the laser energy.

UTEM is a promising method to study the rotation dynamics in nanoscale particle systems. The relevant mechanical parameters, such as impulsive torque, viscous fraction and damping constant causing by friction with the environment, are calculated from experimental results in the single-shot mode [41, 42].

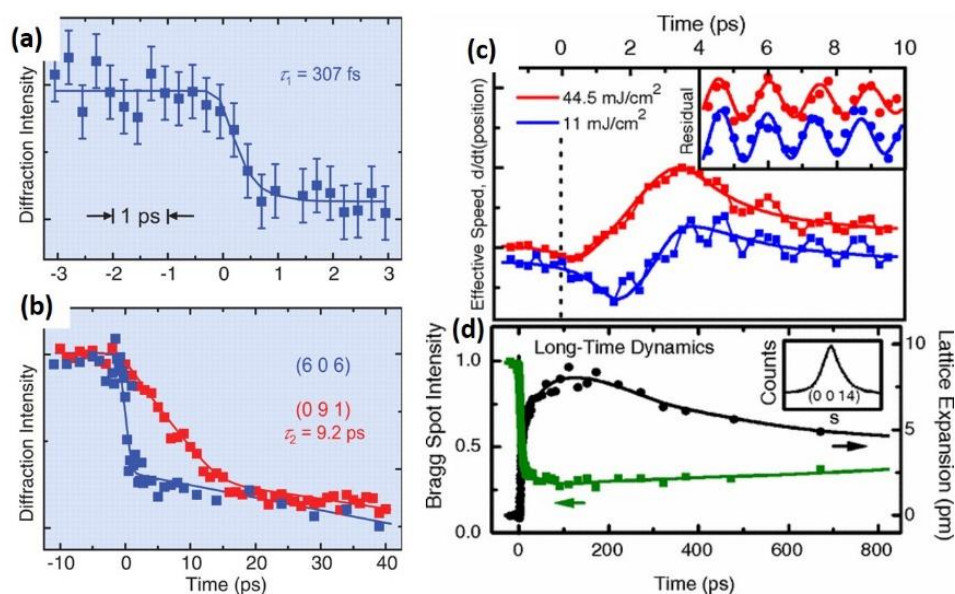


Fig. 2.7 Phase transition of  $\text{VO}_2$ : (a) intensity of the (6 0 6) reflection of  $\text{VO}_2$  as a function of time [47]; (b) intensity of the (6 0 6) reflection (blue curve) and (0 9 1) (red curve) [48]. The structural dynamics of graphite: (c) lattice oscillations of the (0 0 14) reflection; (d) the position and intensity of Bragg diffraction spot (0 0 14) excited by  $44.5 \text{ mJ/cm}^2$ . (a) and (b) adapted from Baum et al. [39]; (c) and (d) are adapted from Carbone et al. [9].

In the single shot mode, the UTEM group in Strasbourg studied fast irreversible processes [7]. They measured a sequence of dynamic processes including the thermal diffusion, the atom diffusion, and the metal solidification in a carbo-thermal reaction [7], as shown in fig. 2.8 and fig. 2.9. After the reduction of nanocrystalline NiO, the elemental Ni particles appeared at  $1.5 \mu\text{s}$ . According to the EELS and diffraction information in fig. 2.9, we know that the reaction finished at  $5 \mu\text{s}$ , but diffraction data show that a liquid transient state of Ni prevailed in the reaction, and the solidification

of Ni happened from 10  $\mu\text{s}$  to 100  $\mu\text{s}$ . The Göttingen team launched a project for ultrafast low-energy electron diffraction to study the ultrafast structural dynamics of surfaces and low-dimensional systems [43]. In 2021, they used an ultrafast dark-field domain imaging method to image transient dynamics of charge-density waves (CDW) in phases of a 1T-polytype of a tantalum disulfide thin film [44]. Lorenz et al. reported a new setup for atom-resolution UTEM and used this setup to get images of bacteriophage T4 where the spacing of the tail sheath proteins was measured to 39.0  $\text{\AA}$  [45].

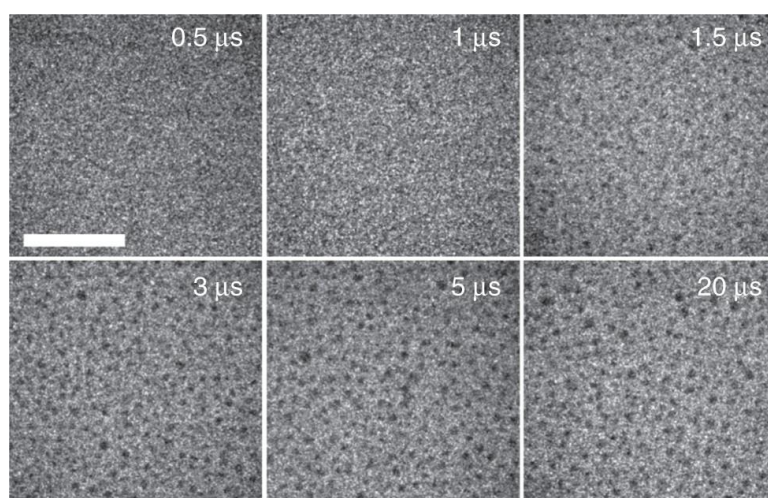


Fig. 2.8. Single-shot TEM images of the laser-induced reduction of a nanocrystalline NiO film to larger Ni crystals at different delays. Only the Ni particles after the reduction are visible. Scale bar: 1  $\mu\text{m}$ . Adapted from Sinha et al. [7].

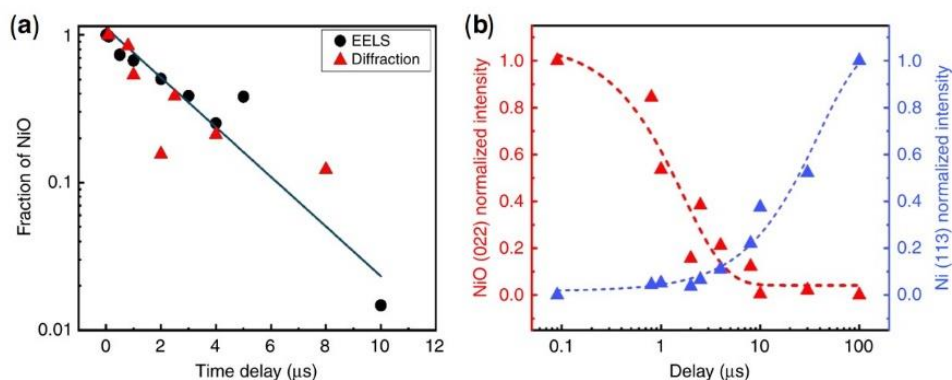


Fig. 2.9. Decomposition reaction of NiO. (a) Temporal evolution of the fraction of non-reduced NiO as taken from EELS (black dots) and from the intensity of the (0 2 2) reflection of NiO (red triangles). (b) Evolution of the diffraction intensities of the (0 2 2)-reflection of NiO and the (1 1 3)-reflection

of Ni. Adapted from Sinha et al. [7].

### UTEM in nano-optics

In 2009, Zewail's group discovered the phenomenon of photon-induced near-field electron microscopy (PINEM), where an optical near-field is created around a nanoparticle and probed by coherent electron pulses in the UTEM [46]. This phenomenon already became the basic method to find the time zero in UTEM experiments and to synchronize pump and probe pulses. After the improvement of the ultrafast low-emittance electron gun, the localized optical near-field in free space around an object could be studied by ultrashort electron pulses. As shown in fig. 2.10, the coherent light-electron coupling can be explained by an infinite n-level energy ladder [46 - 48]. In the near field of an object, the electrons can absorb or emit a photon of energy  $h\nu$  in the photon field, leading to energy gain or loss peaks around the zero-loss peak in the EEL spectrum.

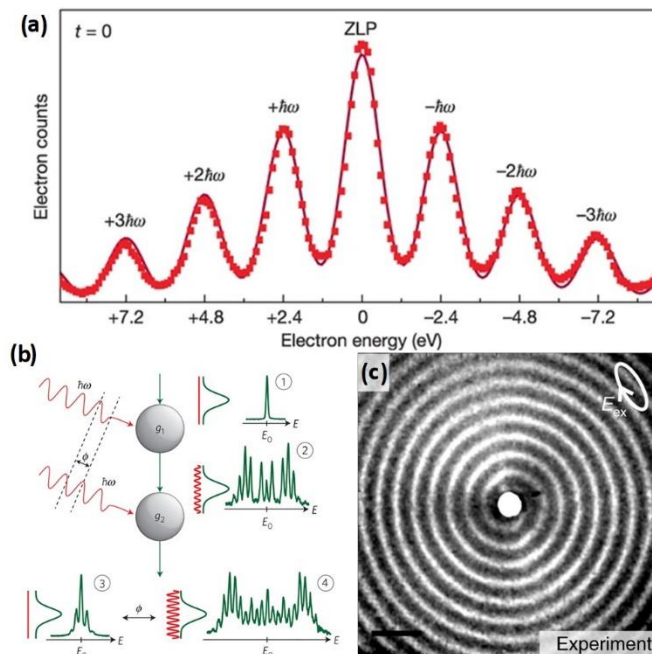


Fig. 2.10 Coherent control of free-electron beams: (a) presents an EEL spectrum around the zero-loss peak where the inelastic interaction between  $n\hbar\nu$  photons and the free-space electron beam appears [46]; (b) Ramsey-type free electron interferometer: 1 shows the incident beam; 2 a single interaction; 3 and 4 show double interactions of near-field

constructive and destructive quantum interference [47]; (c) the spiral phase pattern of surface plasmons generated by an elliptically polarized laser pulse (the scale bar in c is  $2\ \mu\text{m}$  [48]. (a) is adapted from Barwick et al [46]; (b) is adapted from Echtenkamp et al [40]; (c) is adapted from Vanacore et al [48].

Scientists at the Israel Institute of Technology built an optical cavity system and demonstrated the enhancement of electron-photon interaction through resolving the spatiotemporal energy-momentum of a free electron bunch in the UTEM [49]. They explored the interaction between electrons and photons in an optical cavity through mapping the Rabi oscillations in the electron spectrum. Fig. 2.11 shows the schematic setup of the optical cavity in their experiment. Their discovery, according to their description, can be further used for quantum information processing and quantum sensing with free electron beams. Recently, they proposed an ideal system for manipulating quantum information in the UTEM and proved that their method defines a valid qubit with a universal set of gates [49, 50].

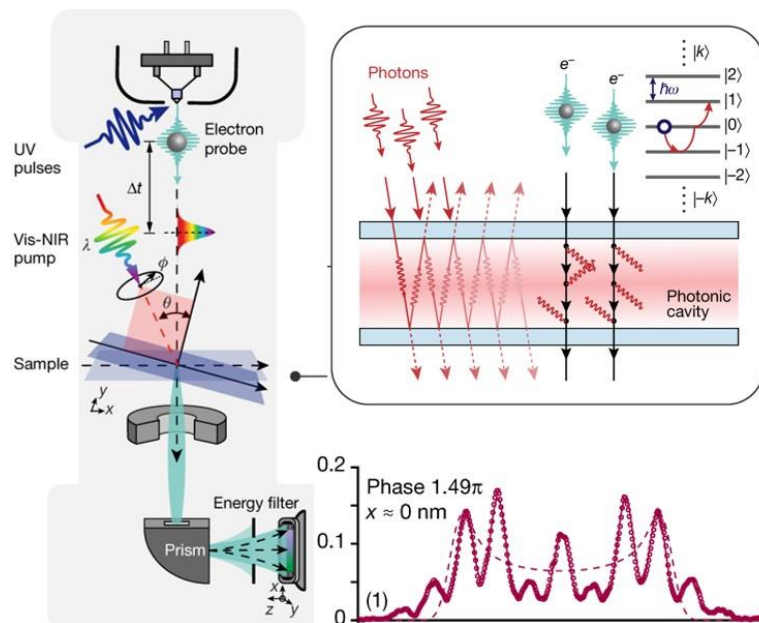


Fig. 2.11 left shows the UTEM system; right (top) shows the optical cavity in the sample and the interactions between electrons and photons in the cavity; right (bottom) shows Rabi oscillations with phase  $1.49\pi$  of the electron energy spectrum. Adapted from [49].

After further improving the equipment with photonic cavities and amplification of a 1064 nm continuum wave laser beam in the specimen holder of a UTEM, the photon quantum statistics effect in PINEM, which, following their description, passes from Poissonian to super-Poissonian [51]. In the free electron–light interaction range, the light can't be treated in the wave model alone [51]. The statistical property can be measured through extracting the electron energy spectrum since the entangled state of the joint free electron–light state isn't a separable state, and the statistical property of the photon is imprinted onto the electron energy spectrum [52]. They described the interactions between free electron pulses and photons as electron quantum/classical walk theory [44, 45]. Two–dimensional polaritons which were created by mid-infrared pulses in two-dimensional materials were also studied by UTEM [ 53].

### Electron pulse compression and attosecond electron pulses

Kealhofer et al used terahertz waves to compress electron pulses by a factor of 12 [54]. As shown in fig. 2.12 (a), a 1 ps laser pulse generated a photoelectron pulse, which was successivley compressed by the THz field through butterfly-shaped metal resonators. The shortest pulse had a FWHM duration of 75 fs, as shown in fig. 2.12 (b). The curve inserted in fig. 2.12 (b) is the shortest pulse curve. In fig. 2.13 (a), a continuous photoelectron beam is modulated by a continuous optical field, and generates attosecond electron pulses. The TEM, as shown in fig. 2.13 (b), is the setup at the Universität Konstanz.

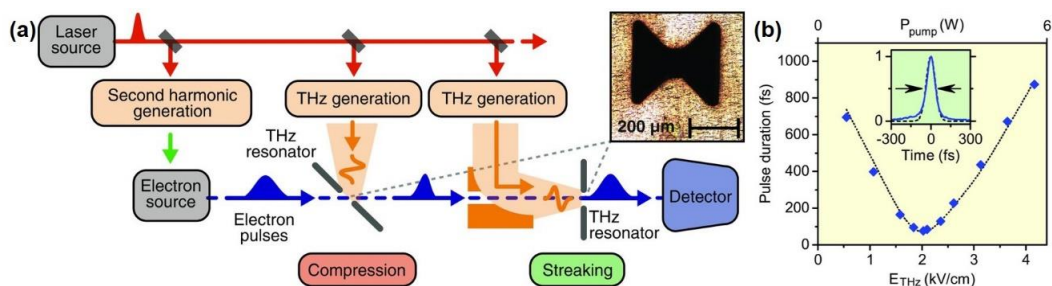


Fig. 2.12 Electron pulse compressed by a THz field: (a) Schematic experimental setup of photoelectron pulse generation and THz field compression; (b) electron pulse duration varied with THz field strength and optical pump power. This image is adapted from Kealhofer et al [54].

Electronic pulse compression techniques can compensate the stretching of the pulse, making the electron pulse shorter than the input laser pulse. This raises hopes in further improvements of the temporal resolution of UTEM.

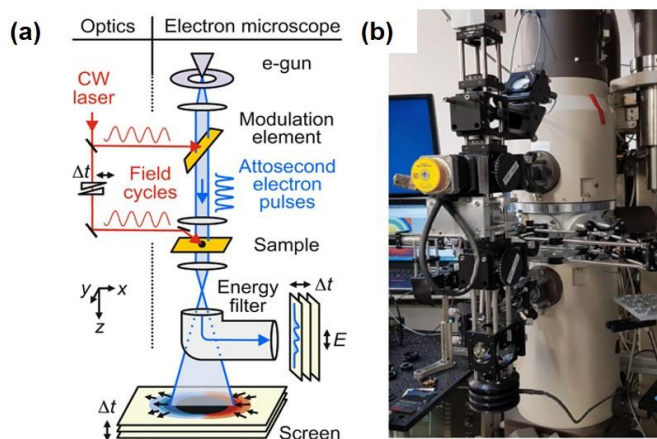


Fig. 2.13 (a) shows a schematic diagram of a light-field-modulated continuous electron beam with attosecond temporal resolution; (b) shows the setup of (a); This image is adapted from Ryabov et al [55].

### 2.3 Phase transitions in nanomaterials

Here, I would like to introduce some studies on phase transitions and transient properties in nanomaterials. Most the phase transition processes in nanomaterials can be measured through the changing optical and electrical properties, but the dynamic processes of morphology changes and domain wall motions in many nanomaterials are still unknown. UTEM has a potential to further boost this field.

Recently, due to the development of sub-picosecond laser pulse generation at mid-infrared (MIR) and Terahertz frequencies (THz), collective modes of solids in broken symmetry states can be studied [56]. In the visible and NIR wavelength range, the photon field has a resonance with electrons in materials. Under the mid-infrared excitation, the crystal lattice of non-superconducting  $\text{La}_{1.675}\text{Eu}_{0.2}\text{Sr}_{0.125}\text{CuO}_4$  was driven through an MIR-active Cu-O bond [56, 57]. The non-equilibrium transient state showed

a superconducting property in time-resolved THz spectroscopy. The light-induced excitation of specific vibrational modes and non-linear response of the lattice are the key to novel properties of solids. All the transient properties, according to these reported results, happened within 10 ps [18, 54]. These transient structural distortions help us further understanding the relation between crystal structure and relevant properties. It can guide us to design materials with unique distortion structure. Stoichevska et al. used sub-35 fs pulses with energy density  $1 \text{ mJ/cm}^2$  and wavelength 800 nm to induce a transition to a hidden state in 1T-TaS<sub>2</sub> (the trigonal phase of tantalum disulfide), which is inaccessible or does not exist under normal equilibrium conditions at 1.5 K in which the resistance of sample shows an abrupt jump and decreases by 3 orders of magnitude [58]. Danz et al. used ultrafast imaging to study the material of 1T-TaS<sub>2</sub> at room temperature and high temperature phases [44]. In their experiment, they employed ultrafast dark-field electron microscopy to demonstrate real-space imaging of charge density waves with high spatial and time resolution. As shown in fig. 2.14, the phase transition can be distinguished by the binary contrast difference. This phenomenon started from a few picoseconds after the pump laser excitation. The time-resolved imaging results are shown in fig. 2.10.

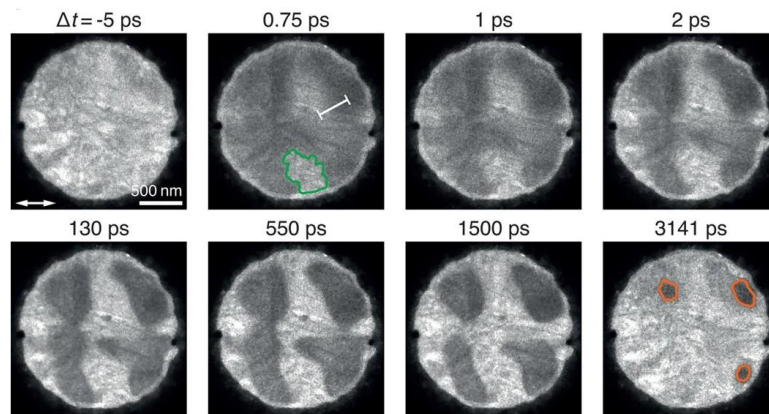


Fig. 2.14 ultrafast imaging of 1T- TaS<sub>2</sub> with different pump-probe delay. This image is adapted from Danz et al. [44].

Zhang et al. employed strain-engineered tuning of La<sub>1/3</sub>Ca<sub>2/3</sub>MnO<sub>3</sub> (LCMO) films [59 - 61] to demonstrate a light-induced transition to a metastable metallic state [60].

Unstrained LCMO films show the ferromagnetic metallic phase. But in an anisotropic strained LCMO film, which is grown on a  $\text{NdGaO}_3$  (0 0 1) substrate [60, 61], the ferromagnetic metallic phase is hidden, and an antiferromagnetic insulator phase is present. At low temperature around 80 K, it is insulating until it is photoexcited to a metallic phase [59]. The antiferromagnetic insulator phase originates from octahedral tilting and a Jahn-Teller distortion breaking the cubic symmetry, thus decreasing the Mn-O-Mn bond angle [59]. In Zhang's work, Terahertz time domain spectroscopy was employed to study the phase transition through analyzing photoinduced conductivity changes. McLeod et al. used multi-messenger nanoprobe, based on atom force microscopy and combined with cryogenic scanning near-field optical microscopy and magnetic force microscopy to study a hidden magnetic metal in LCMO film [62].

In summary, the pump-probe method is promising to study the transient dynamics of nanoscale systems. UTEM is a multifunctional pump-probe method which combines nano-imaging for nanomaterials and nano-systems, electron diffraction for crystallography, and electron energy-loss spectroscopy for elemental analysis and nano-optics.

The study of short-lived transient states shows novel functions of materials which appear in external strong magnetic fields or at low temperature, for example light-induced superconductivity. Through ultrafast studies of phase transitions, functional materials can be further improved, such as in oxides and spin-crossover materials. Static tuning of materials through epitaxial growth and elastic strain engineering are already used to create novel macroscopic states, but still lack detailed studies of ultrafast dynamics. UTEM could be a promising method to study these phase transition materials since in real space and reciprocal space nanoscale spatial and femto- to nanosecond resolution are combined. Through transient crystal distortions and modified properties, we can further explore the physics of new materials. The dynamics of phase transitions also can help us understanding cooperative response, e.g., in memory devices or molecular switches.

## Chapter 3

### Ultrafast Transmission Electron Microscope

#### Contents

<a href="#">Chapter 3. Ultrafast Transmission Electron Microscope</a> .....	19
<a href="#">3.1</a> .....	20
<a href="#">Properties of the electron pulses in the beam</a> .....	20
<a href="#">Electron gun and Acceleration tube</a> .....	22
<a href="#">Condenser lens system</a> .....	25
<a href="#">Imaging system</a> .....	27
<a href="#">Electron energy loss spectroscopy</a> .....	28
<a href="#">3.2 Ultrafast laser pulse technique</a> .....	30
<a href="#">The Ultrafast Transmission Electron Microscope used in this work</a> .....	31

In the third chapter, we introduce the UTEM setup and present our instrument with thermionic and photoelectron gun at the IPCMS as an example. This part provides an overview of the relevant concepts of the microscope, the electron gun, the electron-optics of the illumination system and applications of imaging, electron diffraction and EELS in UTEM.

### 3.1 Transmission Electron Microscopy with short electron pulses

Electron microscopes with static or pulsed electron beams can generate atom-scale images and diffraction patterns for crystallography. The TEM is composed of the electron gun, the illumination system, the specimen stage and the imaging system, and works under high-vacuum. Spectrometers for EDX or EELS are attached for analytical microscopy techniques.

#### Properties of the electron pulses in the beam

If the incident beam is parallel, all rays are focused onto the same spot through an ideal lens. When the electron trajectories between electron-optics components satisfy the Gauss equation, i.e., the paraxial condition where the angles to the optical axis are small, the image formation is straightforward. However, during the transport through the column, the electron pulses, consisting of many electrons within a small space, are elongated due to the repulsive forces between the electrons. The electrons in front and back of the propagating pulse have different energies which will increase the influence of lens aberrations.

To designate the figure of merit of the beam quality, we adopt the definition of emittance, in an ideal focusing system, according to the Liouville's theorem, which is a measure of the parallelism and the focusability of a beam. The emittance is the area of the electron beam in phase-space divided by  $\pi$ . We define the emittance in the  $x$  direction [63]:

$$\varepsilon_x = \iint dx dx' / \pi \quad (3.1)$$

Where  $x' = \frac{dx}{dz} = \frac{v_x}{v_z}$ ,  $v_x$  and  $v_z$  are the inclination angle, velocity of transverse and longitudinal motion respectively. In a reference system with acceleration, the phase-space volume decreases. However the transverse momenta,  $p_x = x' m v_e$ ,  $p_y = y' m v_e$ , don't change.  $m$  is electron mass, and  $v_e$  is electron speed.

Normalized rms (root mean square) emittance which is independent of the acceleration is the commonly used figure of merit for the beam. Normalized rms emittance can be given by [63]:

$$\varepsilon_{n,x} = \frac{1}{m_0 c} \sqrt{\langle x^2 \rangle \langle p_x^2 \rangle - \langle x p_x \rangle^2} \quad (3.2)$$

Where the brackets  $\langle \rangle$  indicate an average over the ensemble of electrons in the bunch. When the beam undergoes irreversible changes like thermal divergence, blocking by apertures, distortion and defocusing at the anode, the emittance deteriorates irreversibly.

Inserting a small condenser aperture, we obtain an electron beam with smaller rms emittance but less electrons. However, according to the Rose criterion, in order to generate an image with sufficient quality, the electron beam has to create enough counts (typically)  $10^8$  in the recording of an image. To consider this aspect, we need to define the brightness of the beam, which is the current density per unit solid angle. The current density is the number of electrons per unit area per unit time. With a current  $I$ , average radius  $r$ , and divergence angle  $\Theta$  of the beam, the brightness can be expressed as [63, 64]:

$$B = \frac{I}{dA d\Omega} = \frac{I}{(\pi r^2) \cdot (\pi \theta^2)} = \frac{I}{\pi^2 \varepsilon_x \varepsilon_y} \quad (3.3)$$

Following the approximation for isotropic beams with average emittance  $\varepsilon$ , the brightness can be written as [63, 64]:

$$B = \frac{I}{\pi^2 \varepsilon^2} \quad (3.4)$$

In analogy with normalized rms emittance, the normalized brightness under relativistic conditions can be defined as [63, 64]:

$$B_n = \frac{B}{\beta \gamma} \quad (3.5)$$

Where  $\beta = v_e/c$  and  $\gamma = 1/\sqrt{1 - \frac{v_e^2}{c^2}}$ .

Temporal coherence is an important parameter of the electron source. A definition of the coherence length  $l_c$  is [64]

$$l_c = \frac{h\nu_e}{\Delta E} = \beta \frac{hc}{\Delta E} \quad (3.6)$$

Where  $h$  is Planck's constant and  $\Delta E$  is the energy spread of electron beam. The temporal coherence is infinite for a monochromatic source. The transverse (spatial) coherence is [64]

$$d_c = \frac{\lambda_e}{2\alpha} \quad (3.7)$$

Where  $\alpha$  is the angle of the beam at the specimen. The transverse coherence is directly determined by the size of the electron source. So, a smaller source gives better coherence [64].

## Electron gun and Acceleration tube

### Continuous electron beam generation

There are two kinds of electron sources for continuous electron beams, thermionic gun and field emitting gun. Basically, the thermionic gun includes three main parts: the heated filament acting as the cathode on high negative potential, the Wehnelt cylinder acting as an electrostatic lens to focus the beam onto the optical axis, and an annular anode at ground potential, as shown in fig. 3.1.

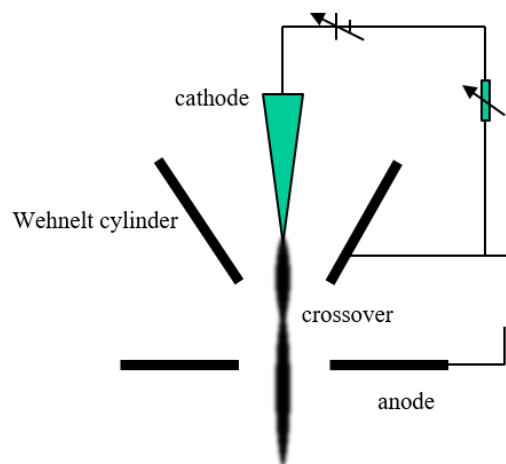


Fig. 3.1 Schematic of a thermal gun with Wehnelt cylinder.

The Wehnelt cylinder with small negative bias relative to the cathode confines the electrons to the gun crossover on the optical axis. The electric field at the surface of the cathode can increase the thermal emission current. However, the electric field is lower than the potential for extracting electrons from the cathode surface. When the added electrostatic field is larger than the exit barrier of the filament and the filament is not heated, the electrons can escape from the filament tip through quantum tunneling. This method is called cold field emission. The field emission may also be thermally assisted by the Schottky effect. The major properties of the electron gun are its brightness, temporal coherence and spatial coherence, which determine the quality of images, diffraction patterns and EELS. Normally, the brightness of a thermionic gun is  $10^9$  A/m<sup>2</sup>sr, in field assisted thermionic emission  $5 \cdot 10^{10}$  A/m<sup>2</sup>sr and in cold field emission  $10^{13}$  A/m<sup>2</sup>sr [64]. The temporal coherence refers to the energy spread of the source. The energy spread in different types of guns is shown in table 1. The transverse coherence is related to the relative source size. A good transverse coherence will improve the image resolution and lead to sharp diffraction patterns and better diffraction contrast. In order to improve the transverse coherence, we need to decrease the filament size, and select a small condenser aperture to decrease the angle  $\alpha$ . As shown in Table 1, the cold FEG and Schottky FEG with very small filament tip has a high-quality electron beam, but the thermionic gun can be improved by selecting small condenser aperture and suitable Wehnelt parameters.

Table 1: parameters in different electron guns with 200 keV~300 keV [64].

	<b>Brightness (A/m<sup>2</sup>sr)</b>	<b><math>\Delta E</math> (eV)</b>	<b>Crossover size</b>	<b>Vaccum (Pa)</b>	<b>Lifetime (hr)</b>
<b>Tungsten thermionic</b>	$10^9$	3	20 $\mu\text{m}$ ~ 50 $\mu\text{m}$	$10^{-3}$	100
<b>LaB<sub>6</sub> thermionic</b>	$5 \cdot 10^9$	1.5	10 $\mu\text{m}$ ~20 $\mu\text{m}$	$10^{-4}$	1000
<b>Schottky FEG</b>	$5 \cdot 10^{10}$	0.7	15 nm	$10^{-6}$	>5000
<b>Cold FEG</b>	$10^{13}$	0.3	2.5 nm	$10^{-8}$	>5000

The thermal emission current density can be expressed by Richardson's law:  $J = AT^2 e^{-\frac{\Phi}{kT}}$ , where  $k$  is Boltzmann's constant ( $8.6 \times 10^{-5}$  eV/K) and  $A$  is Richardson's constant. The Richardson's constant of  $\text{LaB}_6$  is  $4 \times 10^9$  ( $\text{A}/\text{m}^2\text{K}^2$ ). Therefore, we need to heat the filament to a high enough temperature, so that the electron gains enough thermal energy to escape from the filament tip. However, most materials melt or evaporate before reaching the escape temperature. So the only viable thermionic sources are either high melting point materials (Tungsten) or those with an exceptionally low energy barrier  $\Phi$ . The work function of  $\text{LaB}_6$  is 2.4 eV. Currently, the  $\text{LaB}_6$  electron source is the most used in thermionic guns.

#### *Generation of electron pulses*

Ultrashort electron pulses are normally generated by the photoelectric effect. With mode-locking or Q-switch techniques, ultrashort laser pulses can be created and then sent onto a photocathode to create ultrashort electron pulses. The laser pulses on the filament surface may be absorbed or reflected. After the absorption of incident photons, the electrons drift to the cathode surface, and then escape to the open space, as shown in fig. 3.2.

The electrons will be emitted from the filament surface once the incident photon energy  $E_{ph} = h\nu$  is sufficient to overcome the material's work function  $\Phi$ . The emitted electrons have a kinetic energy of  $E_{kinetic} = h\nu + \varepsilon_n - \Phi$ , where  $\varepsilon_n$  is the original energy normal to the surface. The normal energy satisfies the Fermi-Dirac distribution, and the distribution is affected by temperature [65, 66].

At the initial state of the electron pulse, the energy spread and temporal coherence are determined by the energy width of the laser and the electron energy distribution in the filament material. After photoemission, the energy spread increases due to space charge (mutual repulsion of the electrons) at low electron energy. After acceleration and during the propagation in the column, due to the Coulomb repulsion forces, the electron pulse is further elongated, in particular in the lens cross-overs, and temporal

as well as spatial coherence decrease. In a thermal gun used in photoemission mode, the bias voltage of the Wehnelt cylinder has a strong influence on the spatial and temporal spread [67].

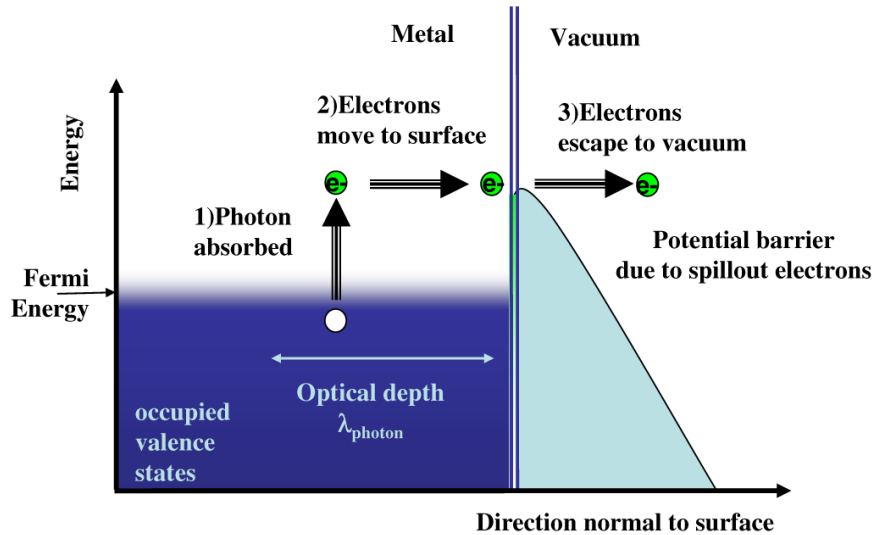


Fig. 3.2 Three-step model of photoemission. This figure reproduced from Treacy et al [66].

The electrons from the filament converge in the crossover in the acceleration tube. These electrons are accelerated by the electrical potential field  $V_0$  parallel to the optical axis between cathode and anode. If the thermal energy  $2k_B T$  ( $\ll 1$  eV) is neglected, the final energy is  $eV_0$ . Normally  $V_0$  is 100 KeV~300 KeV. Effects of special relativity should be taken into account in calculations of the pulse propagation.

### Condenser lens system

The condenser lens system basically includes two condenser lenses C1, C2 and a condenser aperture. The condenser lens C1 is a strong magnetic lens with a focal length of the order 2 mm. The virtual source is de-magnified. The second condenser lens is a weak magnetic lens, which provides little or no magnification, but controls the illumination diameter on the specimen. The focal length is several centimeters. The condenser aperture can be used to control the semi-convergence angle. As shown in fig. 3.3 (a), C1 strongly converges the beam, leading to a smaller spot on the specimen,

but many electrons are filtered out from the optical system. In fig. 3.3 (b), C1 has longer focal length and a larger beam spot reaches the specimen. Here, more electrons are included in in the beam. Through the condenser aperture, the semi-angle  $\alpha$  can be controlled.

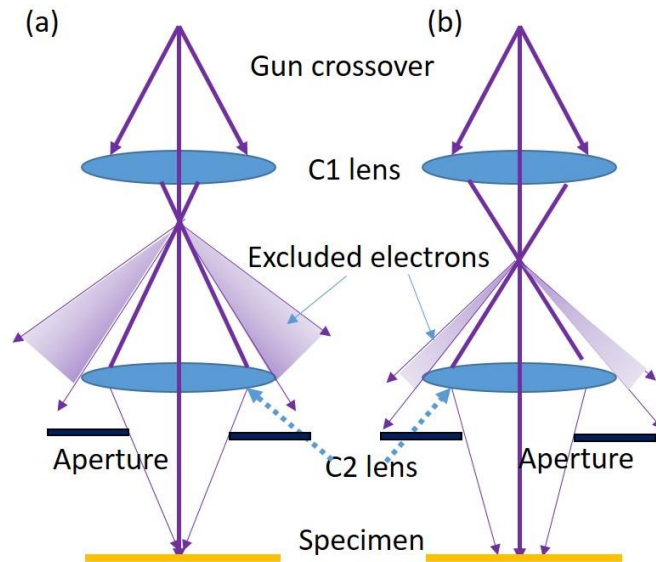


Fig. 3.3 condenser lens system: (a) C1 has a short focal length causing a larger spot at the specimen plane; (b) C1 with weak convergence has longer focal length leading to a larger spot. This figure is reproduced from Williams et al. [64].

The conventional illumination of a TEM including filament, Wehnelt cup, acceleration tube, two magnetic condenser lenses and a condenser aperture reduce the intensity of the electron beam considerably. In conventional TEM, in order to minimize the aberration, it is important to select the paraxial electron beam. This is acceptable because there are enough electron counts to generate an image. But in time-resolved TEM, in particular in single-shot operation, this loss of beam current is crucial and compromises the image quality. An additional C0 lens is inserted which has 15 mm focal length, and increases the intensity of the electron beam [10, 36]. As shown in fig.3.4, it is the schematic of TEM with C0 lens in IPCMS.

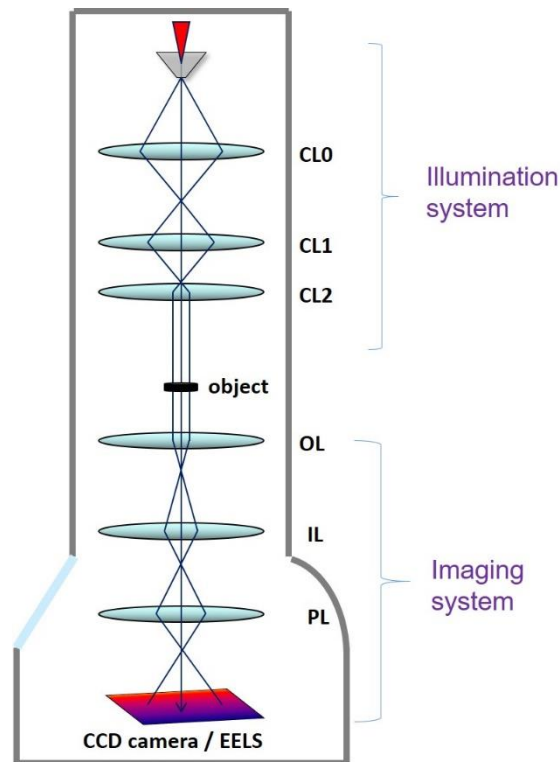


Fig. 3.4. Schematic setup with main components of TEM in UTEM group of IPCMS.

### Imaging system

The objective lens with strong field and small focal length needs a high excitation current. In order to keep a stable working environment, the objective lens as all other lenses need a cooling system to keep a constant temperature to prevent the thermal drift of imaging conditions. Furthermore, in order to maintain the same focal length under different acceleration voltages, the current dc power supply with negative feedback must be stabilized and adjustable. The specimen is in the objective lens and subjected to a strong magnetic field. The real-space image of specimen is produced around 10 cm below the objective lens.

The objective aperture can be inserted into the back focal plane to cut off peripheral electrons. This aperture also blocks the outer electrons scattered at very high angles. Without the objective aperture, the contribution of TDS (Thermal diffuse scattering), generated by the interaction of the probe electrons with phonons in the specimen, to the image is significant. Therefore, with the objective aperture, electrons scattered at high angle can be excluded from imaging.

The selector aperture in the image plane of the objective lens can be used to limit the detected area of diffraction patterns. The selected area is  $D_a/M$ , which  $D_a$  is the diameter of the selector aperture, and  $M$  is the magnification of the objective lens.

After the selector aperture, there are intermediate lenses and a projector lens. The intermediate lenses can change the magnification of the image or the camera length in diffraction through adjusting their focal length in small steps. The image magnification can be changed from  $10^3$  to  $10^6$ . In TEM, we can easily switch between the imaging mode and the diffraction mode through focusing the first intermediate lens onto the image or focal plane of the objective lens. The projector with a few millimeter focal length is used to produce an image on the screen [64].

### Electron energy loss spectroscopy

The incident electron beam interacts with the specimen, and these electrons undergo inelastic collisions with electrons of the specimen. Fig. 3.5 shows the principle of electron energy-loss spectroscopy, which can measure small differences in kinetic energy of the electrons after interaction with the specimen. This is realized with a magnetic prism with a highly uniform magnetic field that bends the electron beam according to the energy loss. This field exerts a Lorentz force onto these electrons. The Lorentz force provides a centripetal force so that the electrons move on circular trajectories with a radius  $R$ :

$$R = \frac{mv}{eB}, \quad (3.8)$$

where  $m$  is the relativistic mass of electron. Those electrons which have lost energy in the inelastic interaction with the specimen have smaller  $R$  than elastically scattered and unscattered electrons. Therefore, the magnetic prism can disperse the electrons with different kinetic energy.

The electron beam passing through the specimen contains elastically scattered and unscattered electrons which are in the Zero-loss peak, those interacted with plasmons or outer-shell electrons below 50 eV (low loss), and inelastic excitation of inner electrons (core loss). The interaction with inner electrons can cause an abrupt increase

in shell ionization, resulting in an edge in the spectrum. The ionization energy is characteristic of a particular chemical element. So the energy of the ionization edge can indicate every individual element in the specimen. EELS can also be combined with imaging in an imaging filter. An example is shown in fig. 3.6, it is the elemental map that represents the elemental distribution in a SCO compound.

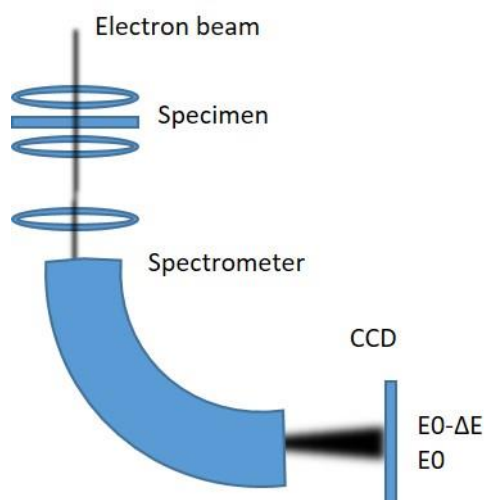


Fig. 3.5 Principle of the EEL spectrometer. A uniform magnetic field is perpendicular to the plane in the 90° prism, and bends the electron trajectories, leading to dispersion. After creating light pulses on a scintillator, the light pulses are guided through a fiber-optic window onto a photodiode or CCD array cooled to -20°C.

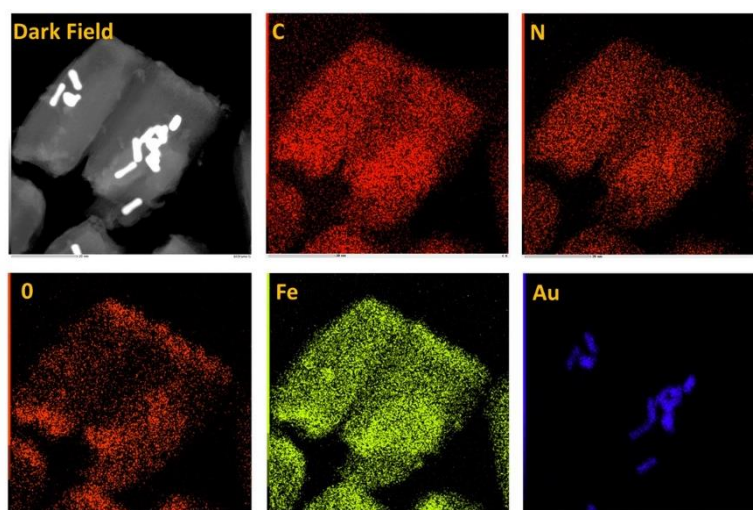


Fig. 3.6 An element distribution map taken with an imaging filter of an SCO compound  $[\text{Fe}(\text{Htrz})_2(\text{trz})](\text{BF}_4)$  with embedded Au particles (see Chapter 4); C-carbon element distribution, N-nitrogen element

distribution, O-oxygen element distribution, Fe-iron element distribution, and Au-gold element distribution. (Images taken by W. Baaziz and M. Picher).

### 3.2 Ultrafast laser pulse technique

In our equipment, we employed laser pulses to create electron pulses on a disc-shaped photocathode. The physical processes are discussed in section 3.1.2. Nanosecond laser pulses are generated by a Q-switching NdYAG laser system. Through controlling the quality factor  $Q$  of the cavity, lasing action is disabled at low  $Q$  and enabled at high  $Q$ . Fig. 3.7 shows schematically the timing of the pump source that synchronizes the flash lamp and Q-switch.

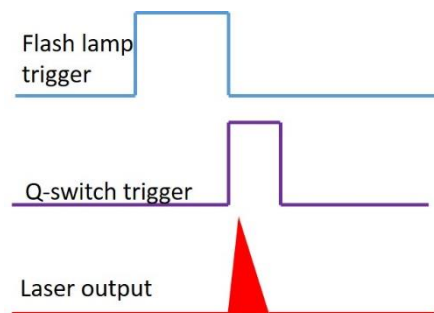


Fig. 3.7 Timing schematic of a Q-switching laser system: when the pump source is lighting the lamp and pumping the gain medium at low  $Q$  cavity, the lasing is disabled. After the pumping is finished, the Q-switch opens immediately and the lasing is enabled.

Short laser pulses from a few tens of picoseconds to femtoseconds are generated by the mode-locking method which is achieved with a modulator (for example, electro-optic type) in saturation absorption. If the active mode-locking, which modulates the resonator losses, is in exact synchronization with the resonator round-trips, pulses up to tens of picoseconds can be generated. The passive mode-locking can generate shorter laser pulses compared with the active mode-locking. In 1985, Strickland et al. reported a technique that was used in radar, and employed in the optical regime [67]. The laser system with millijoule level output and 2 ps duration firstly amplified a linearly

chirped pulse, which was stretched in a fiber through group velocity dispersion and self-phase modulation, and then compressed by two gratings [67,68]. D. Strickland and G. Mourou received the Nobel Prize 2018, for the chirped pulse amplification.

### The Ultrafast Transmission Electron Microscope used in this work

A modified JEOL 2100 transmission electron microscope with thermal gun was used for this work that is capable of performing conventional TEM with continuous beam and time-resolved experiments with electron pulses. It is equipped with multiple laser systems that allow us to observe nanoscale processes from hundreds of femtoseconds to more than a second. Table 2 shows the laser systems installed on the UTEM at the IPCMS.

Table 2. Laser specifications of UTEM at the IPCMS

	Wavelength (IR/green)	Wavelength (UV)	Duration	Repetition (Hz)
Laser pulse (fs)	1030 / 515 nm	213 nm	370 fs	0~40 MHz
Laser pulse (ns)	1064 / 532 nm	355 / 266 / 213 nm	8 ns	0~20 Hz
Laser pulse (ns)	1064 / 532 nm		7n s	0~20 Hz

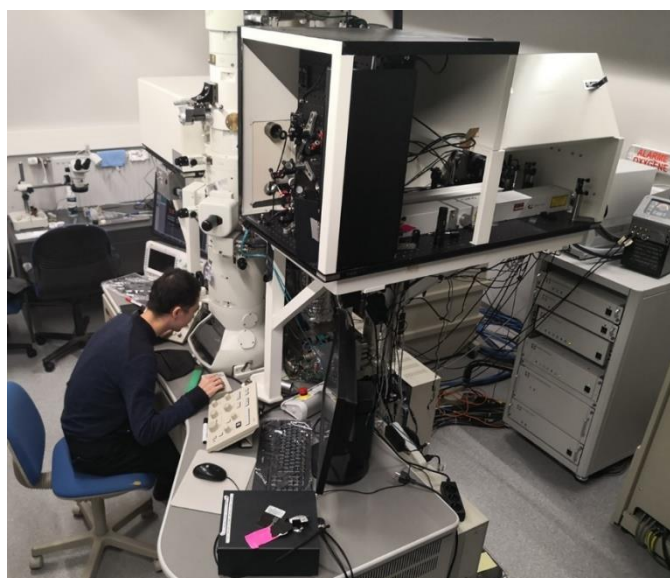


Photo I. The setup of the JEOL transmission electron microscope combined with laser tables.

### Picosecond electron pulses

As shown in fig. 3.8, the femtosecond laser is separated into two branches. As pumping pulse, one laser path through an optical delay line reaches the specimen in the microscope. Another laser a through two non-linear crystals reaches the photocathode and generates the electron pulses. The photoelectron pulse with initial kinetic energy spread  $\Delta E_i$  is generated by the laser pulse at the filament surface. Through a Wehnelt electrode, the electron bunch is focused to the crossover, and then accelerated by the acceleration tube. After free-space propagation and focusing by magnetic lenses, the electron pulse reaches the specimen. The electrons scattered by the sample are collected by objective and intermediate magnetic lenses, and imaged by a CCD camera or an EEL spectrometer.

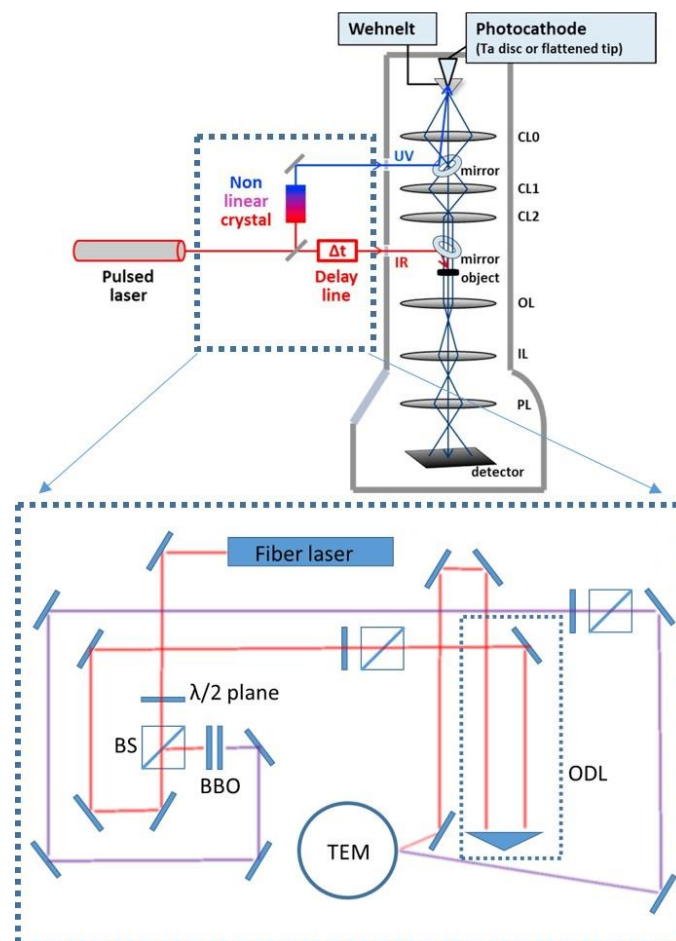


Fig. 3.8 Schematic drawing of the UTEM in the stroboscopic mode: a femtosecond laser system was employed, and the laser pulse was split into two routes: pump and probe; the bottom sketch shows the optical raypaths where ODL is an optical delay line; BBO is an

double nonlinear crystal to create UV pulses from the IR output of the laser.

If we assume a step of the optical delay line of 1 ps, this corresponds to an optical path difference of  $\pm 300 \mu\text{m}$ . In the stroboscopic setup with the fs laser, the UV pulse has a length of 370 fs, but the duration of the electron pulse is widened to 1-5 ps due to repulsion and trajectory effects. As shown in fig.3.9 (a) and (b), the Wehnelt gap length and negative bias voltage strongly influence the energy spread and duration of electron pulse. In order to keep a reasonable time resolution and monochromaticity of the electron pulse, the Wehnelt bias voltage is typically 300 - 400 V. The figs.3.9 (c) and (d) show the tuning of the gun parameters for imaging and EELS in the stroboscopic mode.

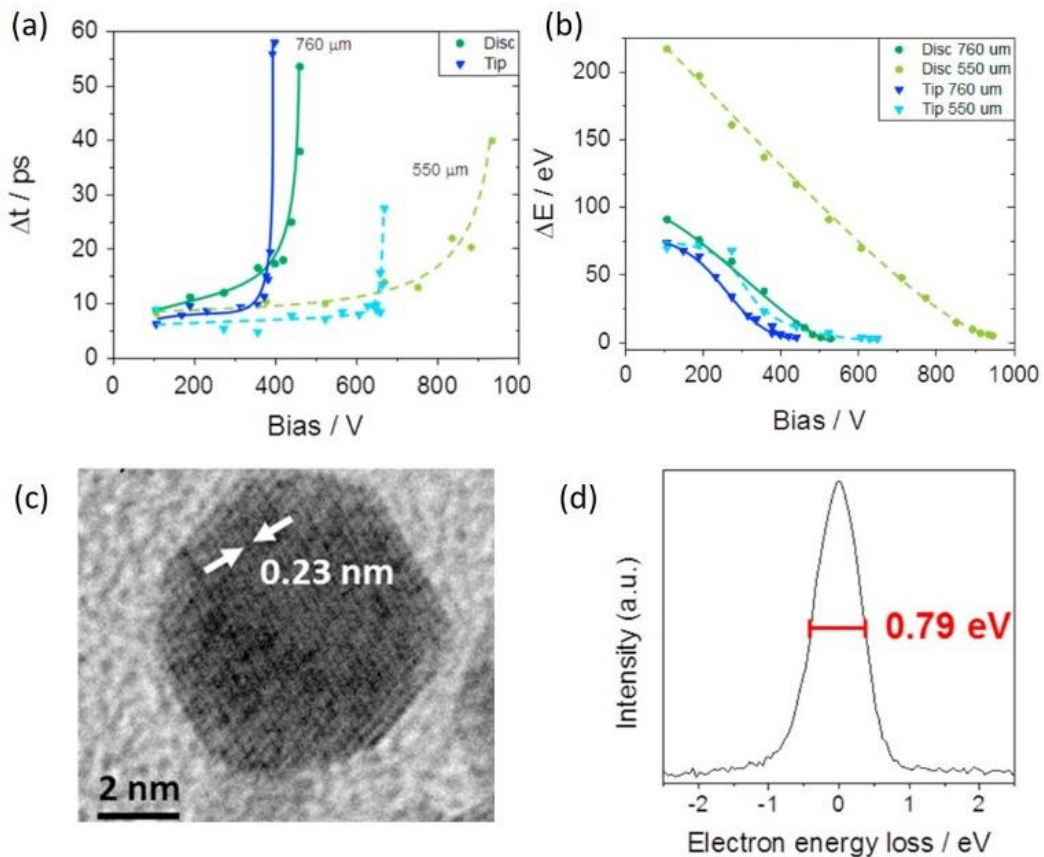


Fig. 3.9 Stroboscopic electron pulses generated by femtosecond laser pulses: (a) electron pulse elongation as a function of the Wehnelt bias voltage, measured for two kinds of filament and gaps of Wehnelt cylinder; (b) energy spread as a function of the Wehnelt bias. (c) lattice resolution image of a Au particle imaged with photoelectrons in  $2 \times 10^7$  exposures; (d) EELS acquired by photoelectron pulses at low intensity. Adapted from Bückner et al [69].

### Nanosecond electron pulses

If the delay time  $t$  between pump and probe exceeds 3 ns, the length of the optical delay of approximately 1 m exceeds the length of the delay line. However, in many studies, we observe transformations at longer timescales, lasting up to hundreds of nanoseconds or even milliseconds [70]. With an optical delay line, these delays cannot be realized anymore. Therefore, we employed an electronic delay to synchronize two nanosecond laser pulses, as shown in fig. 3.10. This setup can be used in stroboscopic or single-shot operation.

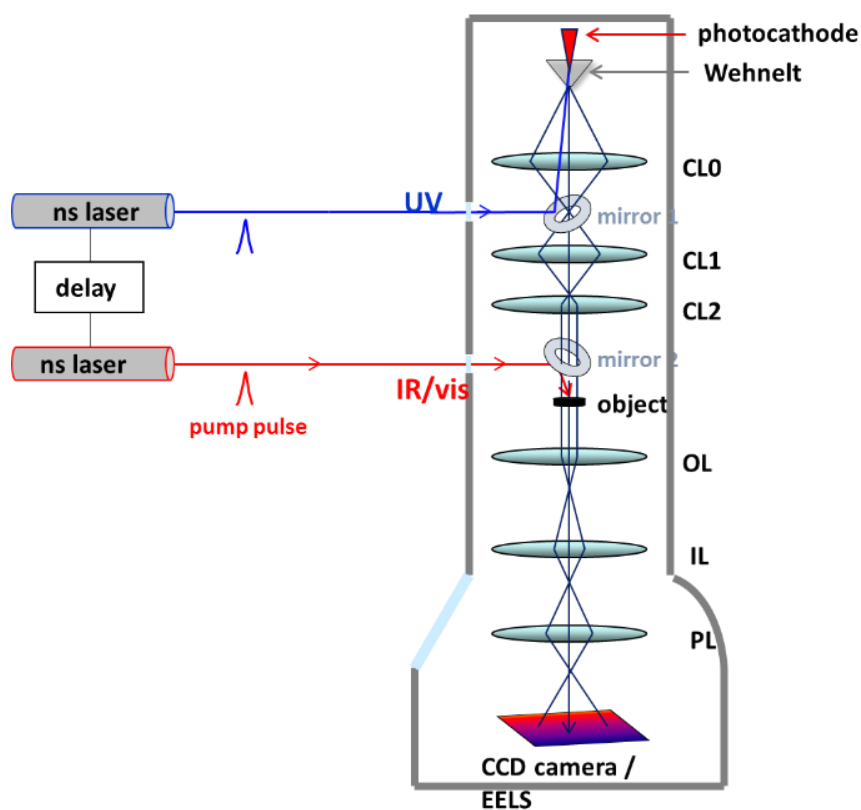


Fig. 3.10 Setup of the UTEM in the single-shot mode or stroboscopic mode with two nanosecond laser systems. The two laser systems are synchronized by an external timing system.

The electronic control is shown in fig. 3.11. The UV laser as master is triggered by its internal timing system. The processes are shown in fig. 3.7. The UV source sends one



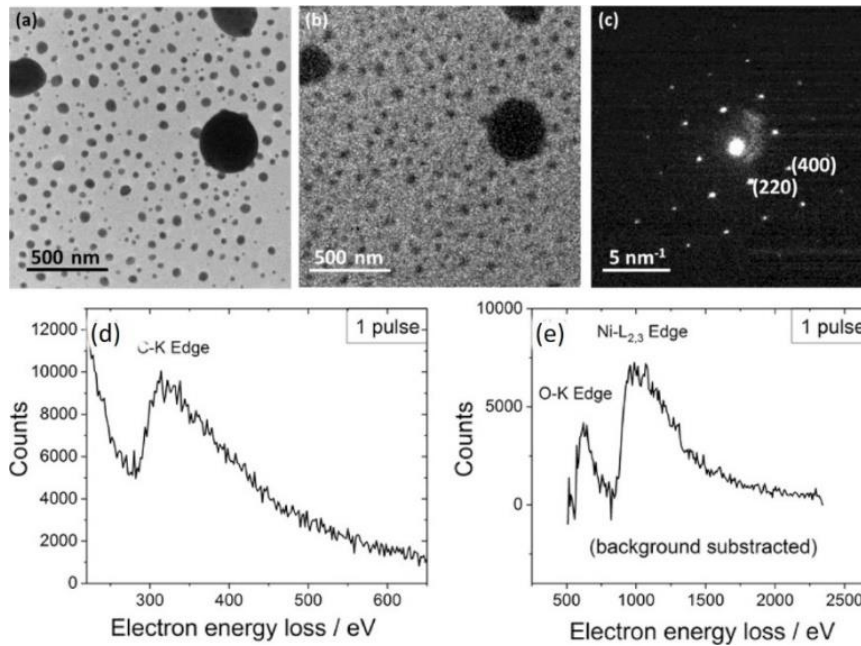


Fig. 3.12 Resolution of the microscope with nanosecond electron pulses. (a) gold particles imaged by 1000 shots of 7ns electron pulses; (b) the same imaged with a single-shot; (c) single-shot diffraction pattern of Si (100); (d) single-shot EELS of a carbon film; (e) single-shot EELS of a NiO film; adapted from Picher et al [71].

The UTEM at the IPCMS can work in the stroboscopic mode from 2.5 ps to 3 ns with picosecond electron pulses and from 7 ns to more than tens of milliseconds with nanosecond electron pulses [69, 71]. For irreversible processes, the setup is used in the single-shot mode, and works from a few nanoseconds to milliseconds. Through energy filtering by the Wehnelt bias, the coherence and energy spread of the electron pulses can be improved. However, since the Wehnelt bias strongly influences the elongation of the electron pulse, a balance between time-resolution and electron pulse quality has to be found for each particular experiment.

## Chapter 4

### Time-resolved experiments on single particles behavior of spin-crossover compounds

#### Contents

<a href="#">Chapter 4</a> .....	37
Time-resolved experiments on <a href="#">single particles of spin-crossover compounds</a> .....	37
<a href="#">4.1 Crystal structure and molecular description of SCO materials</a> .....	38
<a href="#">4.2 Microscopic models for spin-crossover compounds</a> .....	40
<a href="#">The elastic model</a> .....	41
<a href="#">4.3 Experiment</a> .....	42
<a href="#">Single SCO nanoparticle measurement in TEM</a> .....	43
<a href="#">Single SCO nanoparticle behavior under continuous external heating</a> .....	44
<a href="#">Radiation damage effects in SCO particles under the electron beam</a> .....	48
<a href="#">4.4 Time-resolved measurements of single spin-crossover nanoparticles</a> .....	49
<a href="#">Time-resolved measurements of SCO</a> .....	50
<a href="#">Time-resolved measurements of SCO@AuNPs</a> .....	53
<a href="#">Discussion of the results on SCO</a> .....	56
<a href="#">Time-resolved Optical spectroscopy</a> .....	57
<a href="#">Simulation of the light field inside the composite particles Au@SCO</a> .....	58
<a href="#">Oscillation in phase transition in UTEM</a> .....	62
<a href="#">4.5 Conclusion</a> .....	64

In the fourth chapter, firstly we introduce spin-crossover (SCO) materials and the SCO crystal structure and temporal evolution in the phase transition between two spin states from tens of fs to several ms. We investigate the volume change during the phase transition of spin crossover (SCO) nanoparticles ( $[\text{Fe}(\text{Htrz})_2(\text{trz})](\text{BF}_4)$ ) through nano-imaging from nanoseconds to milliseconds.

#### 4.1 Crystal structure and molecular description of SCO materials

Spin transition molecules and complexes are composed of a transition-metal with four to seven d electrons in their valence shell. For example, in the  $[\text{Fe}(\text{R-trz})_3]\text{X}_2$  family, the Fe atom is situated in an octahedral ligand field, and the 3d orbital splits into two levels: a lower energy level  $t_{2g}$ , containing the three degenerated orbitals, and a higher energy level  $e_g$ , formed by the two orbitals [72], as shown in fig 4.1.

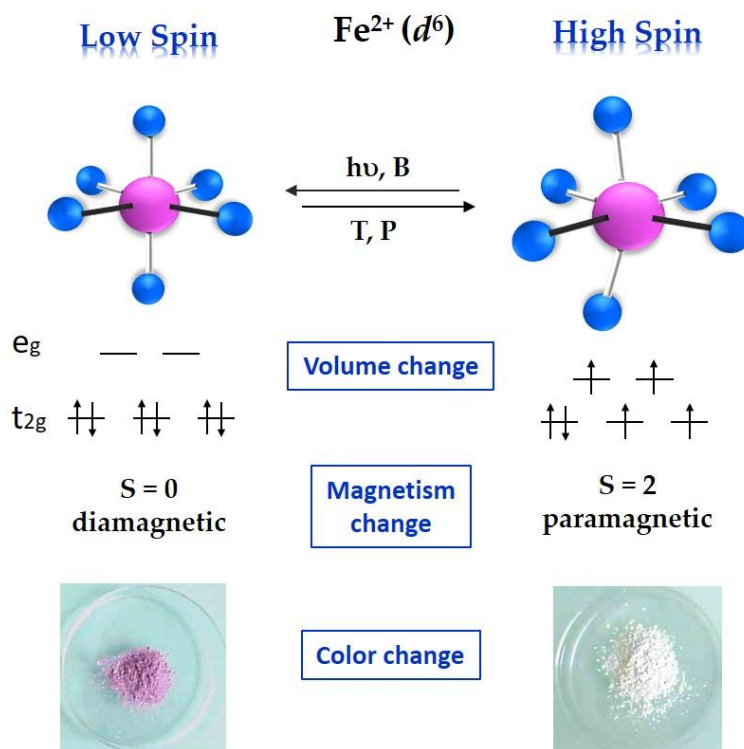


Fig. 4.1 Schematic representation of the molecule  $\text{Fe}(\text{Htrz})_2(\text{trz})(\text{BF}_4)$ . The pink sphere is the Fe atom, and blue spheres are ligands; the electron configuration is shown in the middle part; the bottom images show the color change between LS and HS state. This figure was provided

by our collaborator G. Chastanet (ICMCB Bordeaux).

In the Fe( II ) system, as shown in fig. 4.1, the electron distribution in the d-shell corresponds to the configuration  $t_{2g}^6 e_g^0 L_0$  in the low-spin (LS) state, L refers to ligand orbitals; whereas in the high-spin (HS) state, the electron configuration is  $t_{2g}^4 e_g^2 L_0$  [73, 74, 75]. There is a considerable difference in the length of the bonds between the central metal atom and the ligands in the two spin states. This leads to different volumes of the molecules and finally to different sizes of the molecular crystals. The bond length difference of metal-ligand between LS and HS state in the Fe( II ) system is larger compared with the Fe( III ) and Co( II ) system [76]. The change of the total spin in the Fe( III ) system is equal to  $\Delta S = 2$ , but the bond length difference (0.13 ~ 0.16 Å) is shorter than in the Fe( II ) system (around 0.2 Å). In the Co( II ) system, the total spin changes by  $\Delta S = 1$  and the bond length difference is only 0.07 to 0.11 Å [76].

The transition between the two spin states can be induced thermally (different stability of LS and HS in different temperature regimes) or under photon irradiation. The excitation triggered by light of the singlet metal ligand Fe( II ) complexes leads to the population of lowest-lying high-spin quintet state with unity quantum yield [77, 78]. During this process, the molecule doesn't expand, and this process happens in tens of femtoseconds [77, 78].

The triazole-based polymeric SCO materials  $[\text{Fe}(\text{Htrz})_2(\text{trz})](\text{BF}_4)$  (Htrz=1H-1,2,4-triazole, trz<sup>-</sup>=deprotonated triazolato ligand) attracted attention recently. The LS to HS transition shows a large thermal hysteresis which is slightly above room temperature and a reversible pink to white color change.

The molecules crystallize in a lattice. Recently, the structural data were obtained by X-ray diffraction [79]. The crystal structure of  $[\text{Fe}(\text{Htrz})_2(\text{trz})](\text{BF}_4)$  has an asymmetric unit, because iron connects with Htrz ligands and anion trz<sup>-</sup> ligands, as shown in fig. 4.2. The ligand Htrz, trz<sup>-</sup> and anion  $\text{BF}_4^-$  lie on mirror planes, and the iron lies on an inversion center [79]. The anion  $\text{BF}_4^-$  is situated in the cavity formed by the triazole ligand. The intrachain Fe-(N=N)-Fe distance directly determines the properties of SCO, because

the bond length Fe-N varies by 0.2 Å between HS (high spin) and LS (Low spin). The intra-chain Fe-Fe distance changes to 0.23 Å because of the different molecular chains in b orientation between LS 3.6624 Å and HS 3.8937 Å. The relative variation in the b direction is the strongest within the unit cell. And the variation in a and c direction are 1% and 4% respectively. The corresponding volume variation is 11.5% which is much larger than in other SCO materials (around 5%). The crystal structure is pseudo-hexagonal, due to the relative position of the Htrz ligand and the trz- ligand [79]. The large volume changes under thermal or light pulses are the basis for the applications of SCO materials as photoswitches. This phenomenon has to be studied by UTEM. Only one study has been carried out on SCO materials by UTEM before [80] but didn't reveal the time-resolved expansion behaviour in enough detail and, in particular, did not study plasmonic effects of embedded particles.

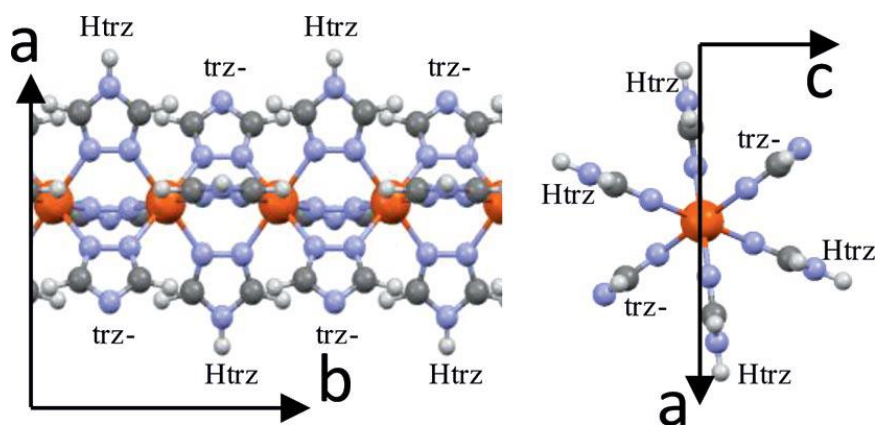


Fig. 4.2 View of the segment of the  $[\text{Fe}(\text{Htrz})_2(\text{trz})]_n$  chain along b, Blue: nitrogen; orange: iron; dark-grey: carbon; light-grey: hydrogen. This picture was reproduced from Grosjean et al. [79].

## 4.2 Microscopic models for spin-crossover compounds

In the SCO system, cooperativity between neighbouring molecules is due to the large difference in metal-ligand bond lengths and corresponding differences in unit cell volumes between the two spin states. When a molecule in an SCO crystal changes its

spin state, the local crystal distortions not only affect the nearest neighbor molecules, but are also causing an effective long-range interaction between other molecules in the system, leading to collective switching of many molecules and thus collective size changes of the molecular crystal.

### The elastic model

In a two-dimensional or three-dimensional SCO system, once the molecules switch from low spin to high spin, the crystal develops a distortion which causes changes of the whole molecular system in the crystal.

In the elastic models, the Hamiltonian can be written as [81 - 83]:

$$H = \frac{1}{2} \sum_i (D - k_B T \ln g) S_i + \sum_{\langle i, j \rangle} V_{ij}^{inner} \quad (4.1)$$

where the first term is corresponding to the classical Hamiltonian used to treat the spin-crossover Ising-type system [81, 82].  $D$  denotes the energy difference between the states,  $g$  is the degeneracy ratio between HS and LS states, and  $S_i$  takes the value +1 for HS and -1 for LS. The second term is the elastic potential which is varied with the individual bond elongations between all neighbouring molecules in the system.

The switching probabilities can be defined based on Arrhenius-type dynamics [83, 84]:

$$\begin{cases} P_{HS \rightarrow LS}^i = \frac{1}{\tau} \exp\left(\frac{D - k_B T \ln g}{2k_B T}\right) \exp\left(-\frac{E - \kappa p_i}{k_B T}\right) \\ P_{LS \rightarrow HS}^i = \frac{1}{\tau} \exp\left(-\frac{D - k_B T \ln g}{2k_B T}\right) \exp\left(-\frac{E + \kappa p_i}{k_B T}\right) \end{cases} \quad (4.2)$$

Where  $p_i$  is local pressure of  $i_{th}$  molecule;  $\tau$  is the scaling constant that keeps the probability below unity;  $\kappa$  is a scaling factor between the local pressure and the activation energy of individual molecule;  $E$  is the activation energy. The molecular motion can be described as a damped oscillatory-type motion [84]:

$$\begin{cases} m \frac{d^2 x_i}{dt^2} = F_{x_i} - \mu \frac{dx_i}{dt} \\ m \frac{d^2 y_i}{dt^2} = F_{y_i} - \mu \frac{dy_i}{dt} \end{cases} \quad (4.3)$$

Where  $x_i$  and  $y_i$  are Cartesian coordinates of molecule  $i$ ;  $u$  is a damping constant;  $F_{xi}$  and  $F_{yi}$  are the components of the instantaneous force.

Fig. 4.3 presents the relationship between the physical processes and timescales of the LS – HS transformations in SCO materials.

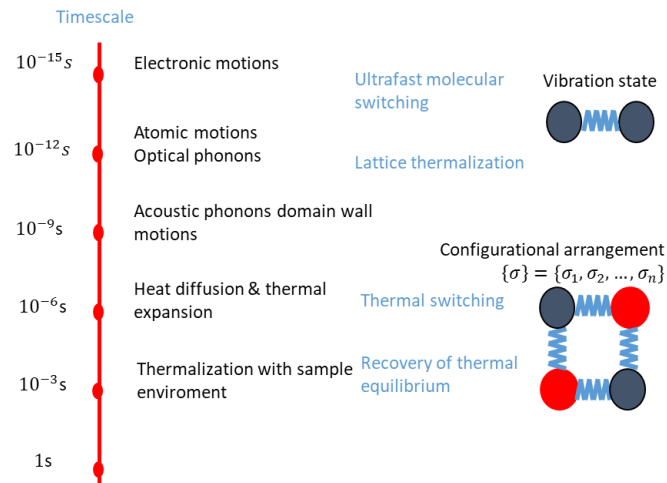


Fig. 4.3 Timescales of dynamic processes in spin-crossover materials after laser induced switching of molecules in the solid state [85].

### 4.3 Experimental results

Fig. 4.4 (a) shows the SCO particles we used in our experiments on graphene, and the length along the b axis is around 550 ~ 600 nm. There is a random orientation distribution of the ac plane by rotation around the b axis. The width of the SCO particles is 150 ~ 200 nm. In fig. 4.4 (b), the magnetic behavior of an SCO film was measured as a function of temperature under an external magnetic field 10 kOe. The magnetic measurements were done at the ICMCB in Bordeaux.

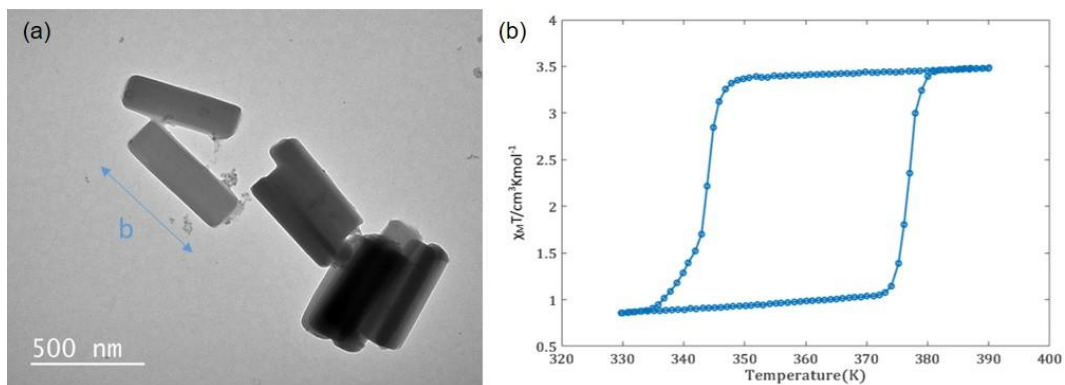


Fig.4.4 (a) TEM image of SCO nanoparticles on a graphene grid, the b-axis of SCO is marked in the image; (b) the molar magnetic susceptibility of  $[\text{Fe}(\text{Htrz})_2(\text{trz})](\text{BF}_4)$  at an applied 10 kOe external magnetic field, and a temperature sweep of 0.7 K/min. The data of (b) were measured by the group of our collaborator G. Chastanet (ICMCB).

At room temperature, the SCO particles  $[\text{Fe}(\text{Htrz})_2(\text{trz})](\text{BF}_4)$  show diamagnetic behavior. Following a temperature increase, at 375 K, the sample shows an abrupt jump to paramagnetic behavior. If the temperature is increased further, the magnetic susceptibility is constant. And when we decrease the temperature, the magnetic susceptibility remains constant until it jumps to the initial value at 335 K.

### Single SCO nanoparticle measurement in TEM

The SCO compounds were dispersed in ethanol, and sonicated 30 s. A droplet of the SCO/ethanol solution was deposited onto a graphene grid. Fig. 4.5 (a) presents the pure SCO particle and SCO encapsulating gold nanoparticles (SCO@AuNps), which were used to enhance the photo-thermal effect due to plasmonic heating under laser pulses (see below). The size distribution of pure SCO particles in the long b-axis direction is 450 ~ 600 nm, and the width distribution is 80 ~ 160 nm. The SCO@AuNps length in b-axis direction is 300 ~ 450 nm, and the width distribution is 100 ~ 280 nm.

The gold particle's shape is rod-like. Their length varies from 50 nm to 80 nm. And their diameter is from 15 nm to 21 nm. The particles are randomly distributed in the SCO nanoparticles.

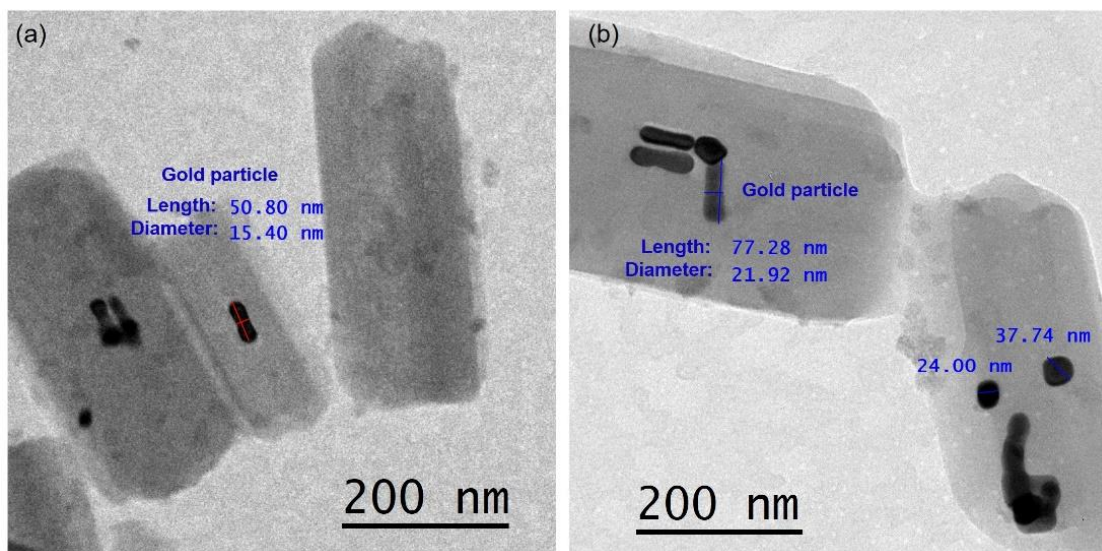


Fig. 4.5 (a) TEM image of pure SCO particles and SCO@AuNps; (b) SCO@AuNps with different sizes and shapes of gold nanoparticles.

### Single SCO nanoparticle behavior under continuous external heating

To measure the sizes of SCO particles as a function of temperature, experiments were done by using a TEM heating specimen holder. Images of SCO particles were taken with a continuous electron beam at different temperatures.

All images were taken by a low brightness electron beam. The beam current was 0.5 ~ 0.6 pA and the exposure time was 0.5 s. The average length of SCO nanoparticles along the crystal b-axis is 450 nm. The average width of SCO nanoparticles is 80 nm. Fig. 4.6 shows the measurements in the TEM. The specimen was heated starting from room temperature. At around 370 K, its length shows an abrupt jump. The maximum expansion is 5.1%. Under further increase of temperature, the length remains in saturation. When we decrease the temperature, the length is reduced by a few nanometers, and has an obvious jump back to the initial length at 330 K. The expansion ratio shows an obvious hysteresis. The width is close to 40 K.

When the temperature increases from 330 K to 360 K (red curve in Fig. 4.6), the particle length increases by only 1 nm compared with the initial state. This can be

described as a cluster formation at the surface where the spin transition starts (transition LS  $\rightarrow$  HS) [84]. When the temperature decreases from 370 K to 330 K (blue curve), the reverse cluster formation at the surface happens again in the relaxation process (HS  $\rightarrow$  LS) [84]. Fig. 4.7 presents the hysteresis curve of a SCO particle with size 527 nm  $\times$  150 nm.

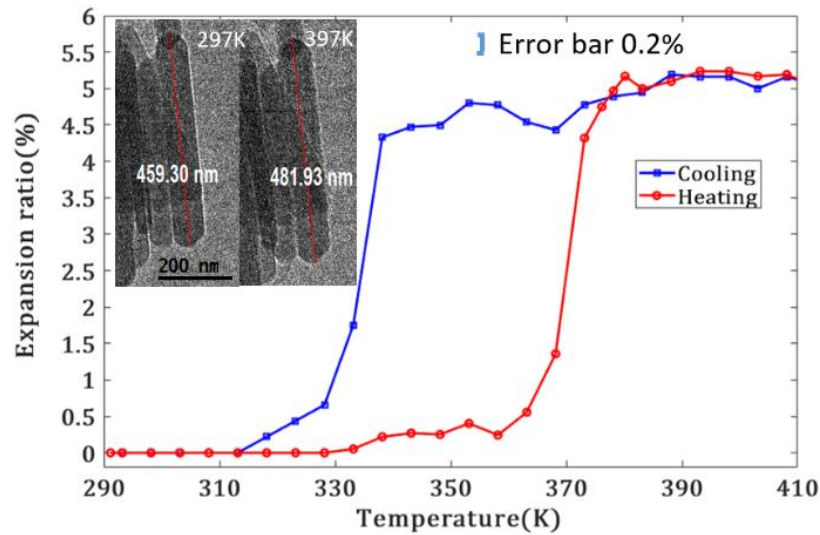


Fig. 4.6 Length measurements of a SCO particle at different temperatures. The hysteresis curve of a single SCO particle (459 nm  $\times$  80 nm) was measured along the b-axis.

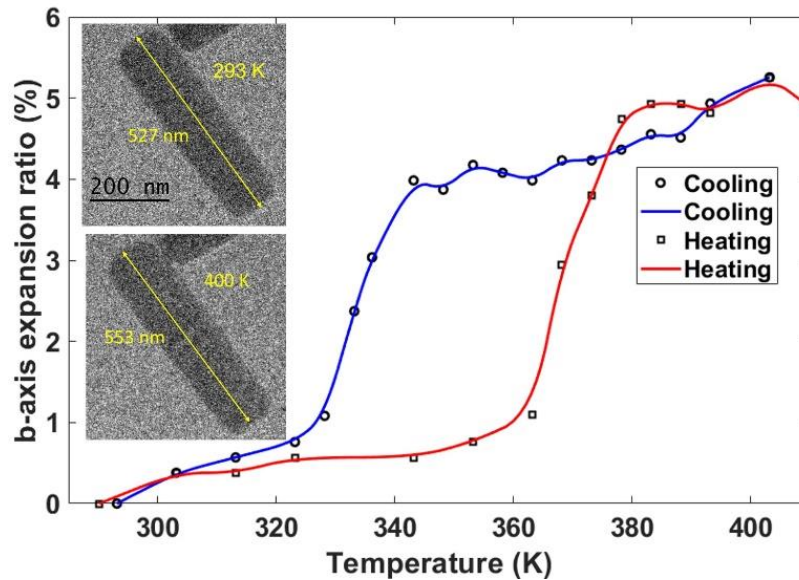


Fig.4.7 Hysteresis curve of a SCO particle (527 nm  $\times$  150 nm) with elongation along the b-axis.

The particle has a hysteresis width of around 40 K, and the length increases rapidly at 370 K. At 330 K, the particle is back in the low spin state saturation. These two SCO

particles with different size show therefore similar results, indicating that size effects are less important in 400 ~ 600 nm.

The SCO compounds  $[\text{Fe}(\text{Htrz})_2(\text{trz})](\text{BF}_4)$  have a very low absorption in the near-infrared band. In order to reduce the laser fluence and the photo-switching time, heating of the SCO particles is promoted by encapsulating plasmonically active gold nanorods. The surface plasmon resonance effect is hence employed in the light-induced phase transition process [86, 87].

As shown in fig. 4.8, the gold nanoparticles (AuNps) were inserted into SCO particles by our project partners at ICMCB, and the same procedure as described above is repeated. The elongation is measured as a function of temperature, still in thermal equilibrium without laser irradiation. The red curve is the heating process and the blue one is the cooling process. Due to gold particles inserted in SCO, the SCO crystal has a slight distortion. So the elongation under temperature increase is slightly lower than pure SCO materials.

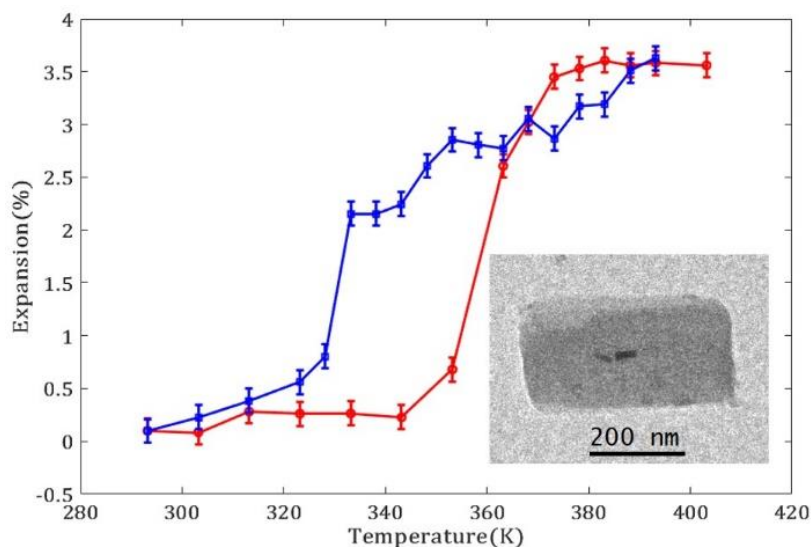


Fig.4.8 Hysteresis curve of single SCO@AuNps elongation along the b-axis.

External magnetic and electric fields affect the thermal excitation [88]. As discussed in the chapter 3, the specimen stage is the objective lens, and affected by the strong magnetic field. According to the relation [88]

$$\Delta T = -\frac{(\chi_{HS} - \chi_{LS})B^2}{2\mu_0 k_B \ln g},$$

we see that the transition temperature will decrease under an external magnetic field, where  $\chi_{HS}$  and  $\chi_{LS}$  are the magnetic susceptibilities;  $B$  is the magnetic field and  $\mu_0$  is the magnetic permeability. The susceptibility of SCO satisfies the relation  $\chi_{HS} > \chi_{LS}$  under an external magnetic field, as shown in fig. 4.4 (b). Comparing the susceptibility measurements in fig. 4.4 b with our length measurements in fig. 4.5, the transition temperature of SCO in TEM differs by around 5 K. This shift of the thermal hysteresis could be due to the magnetic field (1 – 2 T in the TEM), but the shift is small and difficult to separate from uncertainties due to the calibration of the TEM heating stage.

The expansion ratio of SCO@AuNps is slightly lower than of pure SCO particles. This is most likely due to the replacement of SCO material by the non-expanding Au particles. We measured more particles and randomly selected the particles, as shown in fig. 4.9. The particles 1, 2, 3, and 4 were used to demonstrate the maximum elongation and the hysteresis behavior. The maximum elongation is 4% ~ 4.5%. It is lower than the pure SCO elongation 4.5% ~ 5.2%. However, the maximum hysteresis width is around 35 K ~40 K.

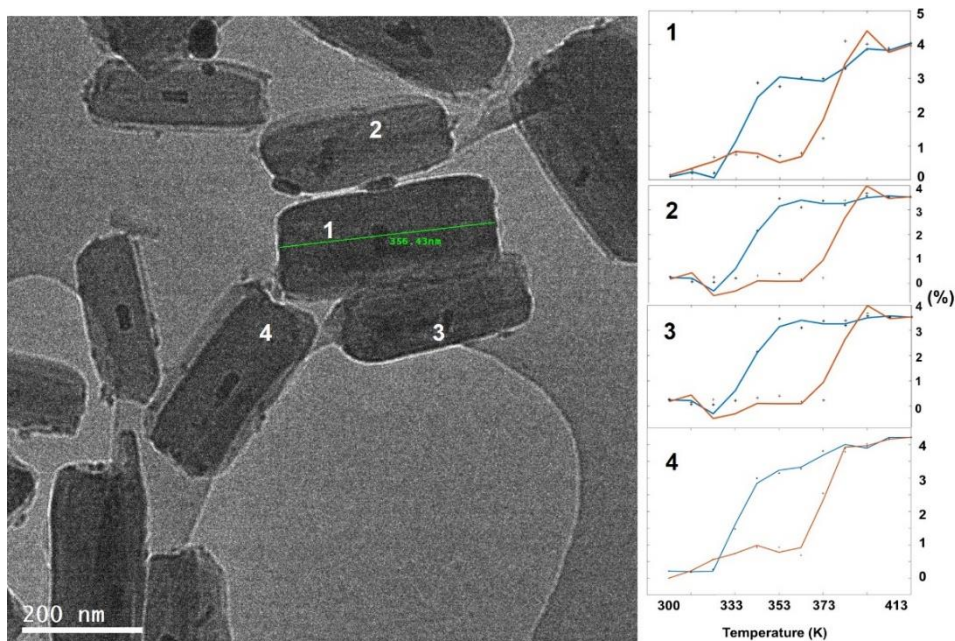


Fig. 4.9 SCO@AuNps measurement in the heating stage: left side TEM image shows many SCO@AuNps

on the amorphous carbon film; right side shows the hysteresis curves of the particles 1, 2, 3, and 4.

### Radiation damage effects in SCO particles under the electron beam

Before concluding about the expansion effects in SCO particles, their sensitivity to the electron beam had to be studied. The maximum tolerable electron dose on SCO particles before the expansion effects vanish was determined. This section presents the results where a high brightness electron beam illuminates the SCO compounds. As shown in fig. 4.10, under 4.8 pA electron beam illumination and after 1 min, the nanoparticle has a shrunk from 660 nm to 610 nm. This demonstrates that an intense electron beam damages and finally evaporates the SCO compounds.

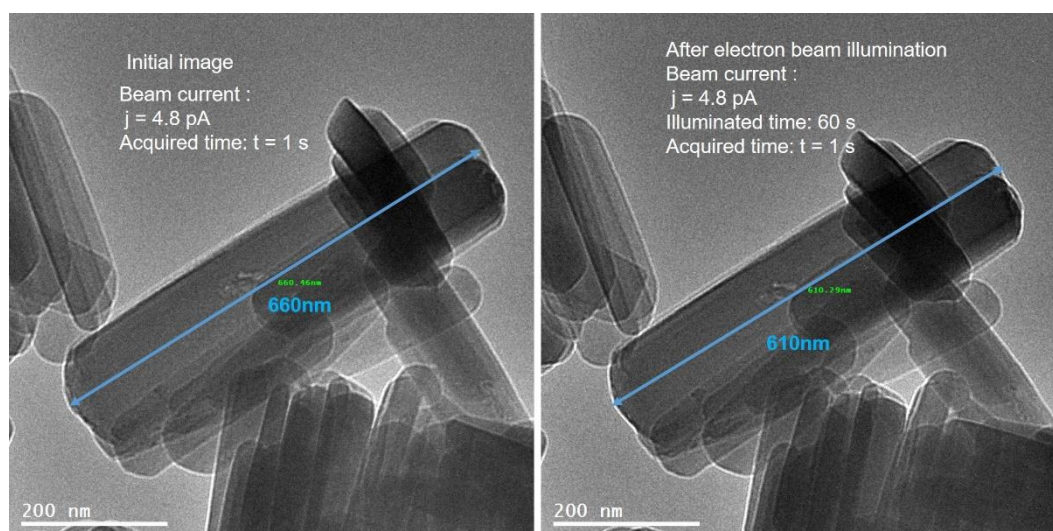


Fig. 4.10 SCO particle transformation under the electron beam: left side image shows the particle before electron irradiation; (b) right side image was acquired after long exposure to irradiation.

When we decreased the current to 1 pA, the particle after the first-cycle measurement was already damaged, as shown in fig. 4.11. In the first cycle, the particle elongation along the b-axis still reached 5%. In the second cycle, the particle expansion and relaxation happened at lower temperature. Compared with the first-cycle measurement, the hysteresis width and elongation are reduced. Therefore, care was taken in all length measurements that the electron beam dose was kept far below the damage threshold where radiation effects have a measurable influence on the measurements.

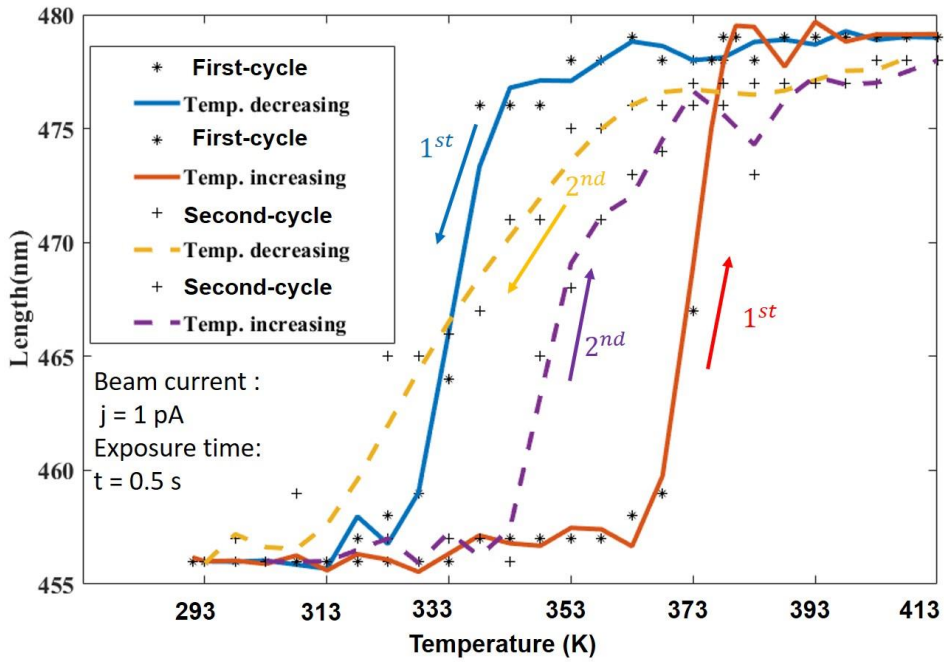


Fig. 4.11 SCO particle hysteresis curve under heating after different electron doses. The difference between first-cycle heating-cooling (low irradiation dose) and second-cycle (high irradiation dose) heating-cooling under 1pA electron beam illumination and 0.5 s exposure is visible.

#### 4.4 Time-resolved measurements of single spin-crossover nanoparticles

The SCO phase transition, which is a reversible process as described in section 4.3, was studied by TEM. Considering the high speed of the transformation, stroboscopic experiments with picosecond electron pulses would be appropriate. In order to get a good quality image with acceptable noise level, approximately  $10^9$  counts have to be acquired in one image. However, since each picosecond electron pulse in our UTEM only includes  $5 \times 10^2 \sim 10^3$  counts, an exposure would need  $10^6$  pump-probe cycles. The relaxation period from excitation to the ground state of SCO particles takes 0.5 ms to 2 ms. So, with picosecond electron pulses, it would take at least 30 minutes to accumulate counts in an image. In order to explore the dynamic process and reproduce the results, we would have needed to acquire thousands of images which would be too time-consuming with such long exposure times. Therefore, we decided to carry out

the experiment with nanosecond electron pulses. Each nanosecond electron pulse includes  $10^5 \sim 10^6$  counts, and the repetition is 20 Hz in our experiment. Each image takes 60 s  $\sim$  100 s which is acceptable in our experiment.

Ultrafast transmission electron microscopy (UTEM) allowed us to observe the behavior of individual particles which isn't possible by any other time-resolved technique. In a pump-probe approach, a nanosecond laser pulse (1064 nm, 7 ns pulse duration) is focused onto a spot (150  $\mu\text{m}$ ) on the specimen grid in the column of the UTEM. Although the absorption of SCO at 1064 nm is very low, length changes of pure SCO particles up to saturation could be achieved through heat conduction from the graphene substrate at pulse energies in the range 4 – 40  $\mu\text{J}/\text{pulse}$ , corresponding to 20 – 200  $\text{mJ}/\text{cm}^2$  per pulse. Each IR pulse is followed after an adjustable delay by a 7 ns electron pulse that served for imaging the particles, so that their morphology could be measured as a function of time. The temporal resolution in this configuration is approximately 8 ns; however, relative length changes can be recorded in slightly smaller steps. Due to repulsive electron-electron interactions within the intense pulses which cause a loss of coherence and electron energy spread, the electron counts in every pulse had to be limited. It is also important to avoid radiation damage by the electron beam that occurs under longer exposure to a high brightness electron beam.

The pump-probe delay is adjusted by synchronizing the two lasers with an electronic delay unit, which is described in chapter 3. Since the volume changes of the SCO particles are reversible, the experiments were carried out repeatedly for each measurement in a stroboscopic approach with a repetition frequency of 20 Hz. For recording a measurable image, 1200 pulses are summed up within the typical acquisition time of 60 s.

### Time-resolved measurements of SCO

To ensure that no undesired radiation damage of SCO by the electron beam occurred, some particles were exposed deliberately to electron irradiation. After a dose

exceeding approximately  $1000 \text{ electrons/nm}^2$ , the thermally induced expansion isn't observable anymore. Therefore, all pump-probe experiments were carried out at much lower electron dose (typically  $0.02 \text{ electrons/nm}^2$  per pulse or  $24 \text{ electrons/nm}^2$  during the recording of an image), where electron beam effects are negligible. Fig. 4.12 (a) shows an SCO particle in an image generated by 1200 electron pulses. In the fig. 4.12 (b), the principle of the stroboscopic mode with nanosecond electron pulses is shown.

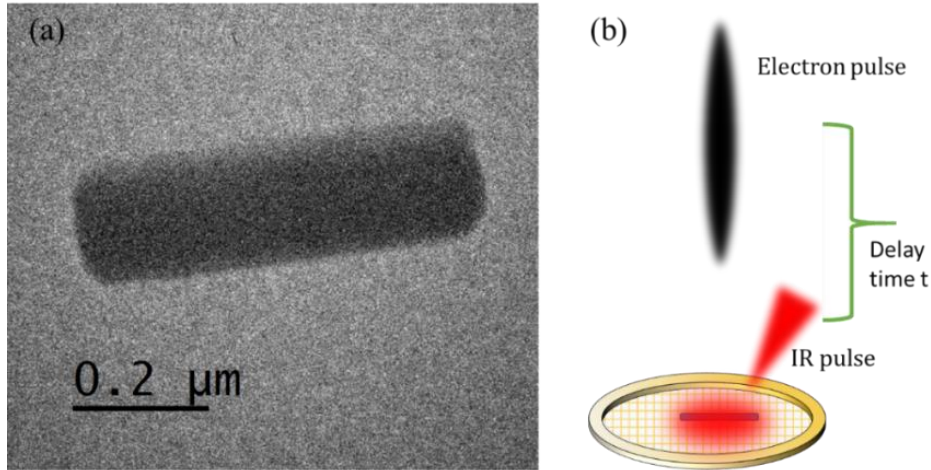


Fig. 4.12 (a) shows a SCO nanoparticle imaged in the photoelectron mode without laser pulse excitation; (b) is the pump-probe principle: after a delay time  $t$ , the electron pulse detects the excited nanoparticle.

Fig. 4.13 shows the measurement results on SCO nanoparticles in a comparison between  $t = -5 \text{ ns}$  and  $t = 500 \text{ ns}$ . At the delay time  $t = 500 \text{ ns}$ , the particle elongation ratio reaches 5.3% which is the saturation. And the width expansion is around 3%.

In fig. 4.14, the pure SCO particle was excited by IR laser pulses with different energies. The green curve in fig. 4.14 shows the full saturation after a  $20 \mu\text{J}$  IR laser pulse, whereas the red line shows the low saturation of SCO nanoparticle that is triggered by  $8 \mu\text{J}$  IR laser pulses. After full saturation of an SCO particle, almost  $1 \text{ ms}$  is needed for recovery to the LS state. The relaxation time after low excitation is around  $150 \text{ ns}$ . The blue curve in fig. 4.14 shows excitation by  $15 \mu\text{J}$  laser pulses, and the relaxation time is  $200 \mu\text{s}$ . The rise time for full saturation is  $120 \text{ ns}$  for pure SCO materials. The left slopes of the curves are almost identical, showing that the expansion speed does not depend considerably on the power of the laser pulses.

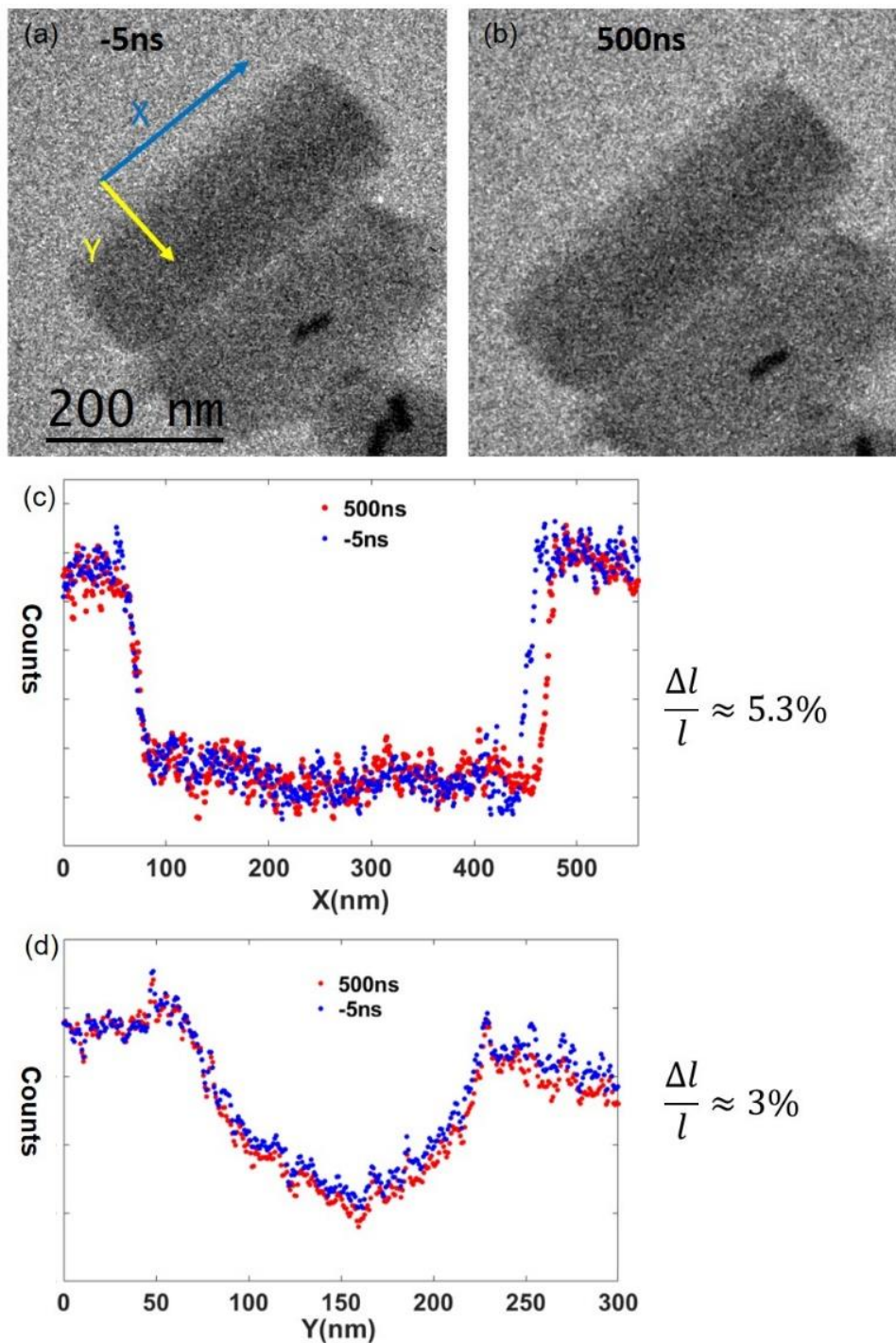


Fig. 4.13 (a) Image of a pure SCO particle at -5 ns; (b) at 500 ns; (c) shows the length profile in b-axis orientation of the SCO particle, measured along X; (d) is the width change, measured along Y. The blue profile is before, the red 500 ns after the laser pulse.

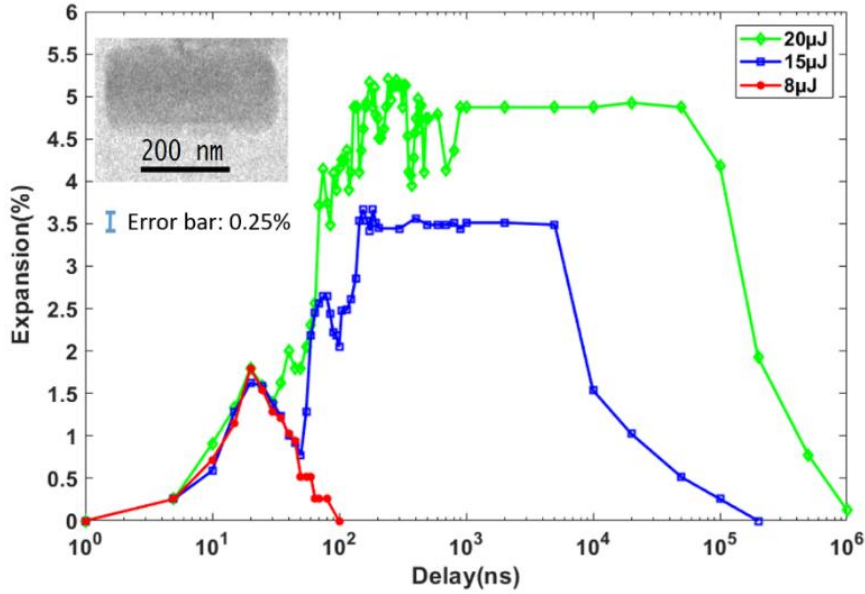


Fig. 4.14 The expansion of a pure SCO particle triggered by different laser energies.

#### Time-resolved measurements of SCO@AuNPs

After measuring the expansion of pure SCO particles, the heating efficiency of embedded plasmonic Au particles was studied. Since the gold particles replace some SCO molecules, in the measurements, we excluded the central region with the gold particles for the length measurements. Fig. 4.15 shows measurement results of SCO@AuNPs as a comparison between  $t = -5$  ns and  $t = 500$  ns.

At a delay time  $t = 500$  ns, the particle elongation reached the saturation expansion of its length of 5.1%. The width difference is 2.1%. The measurement areas are marked by dashed lines in different colors. As shown in fig. 4.16 and fig. 4.17, the SCO@AuNPs were excited by different laser powers. In the fig. 4.16, 3 gold particles were encapsulated in the SCO materials, the saturation time is around 25 ns. The elongation is much faster than the pure SCO particle (Fig. 4.14). And the relaxation to the original length takes from 500  $\mu$ s to 1 ms.

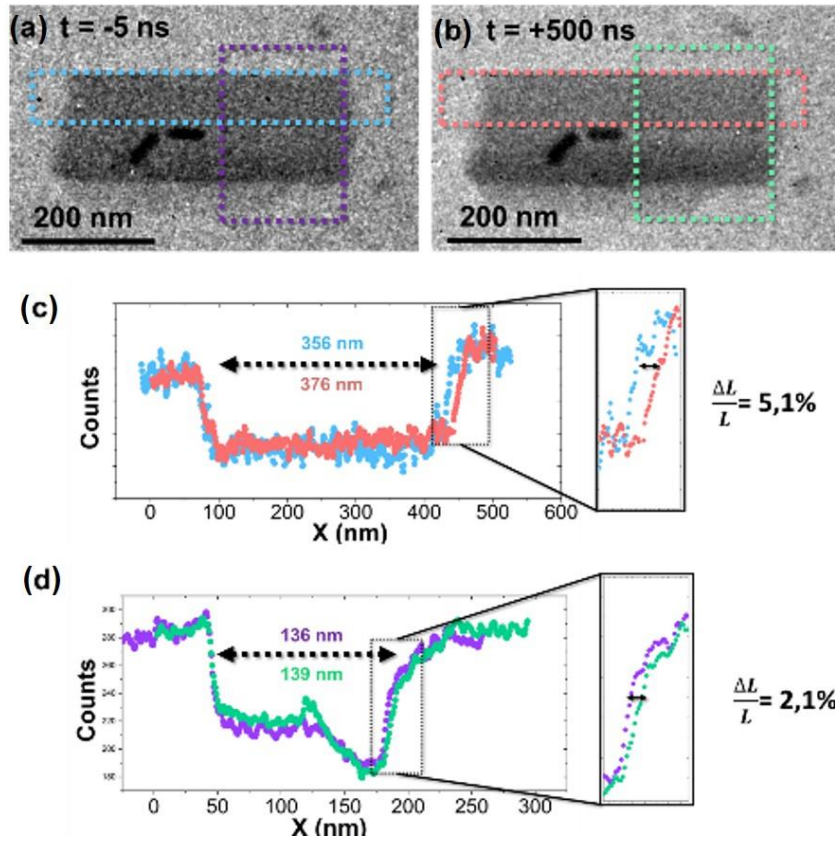


Fig. 4.15 (a) SCO particle at -5 ns; (b) at 500 ns; (c) shows the length change in b-axis direction; (d) shows the width change.

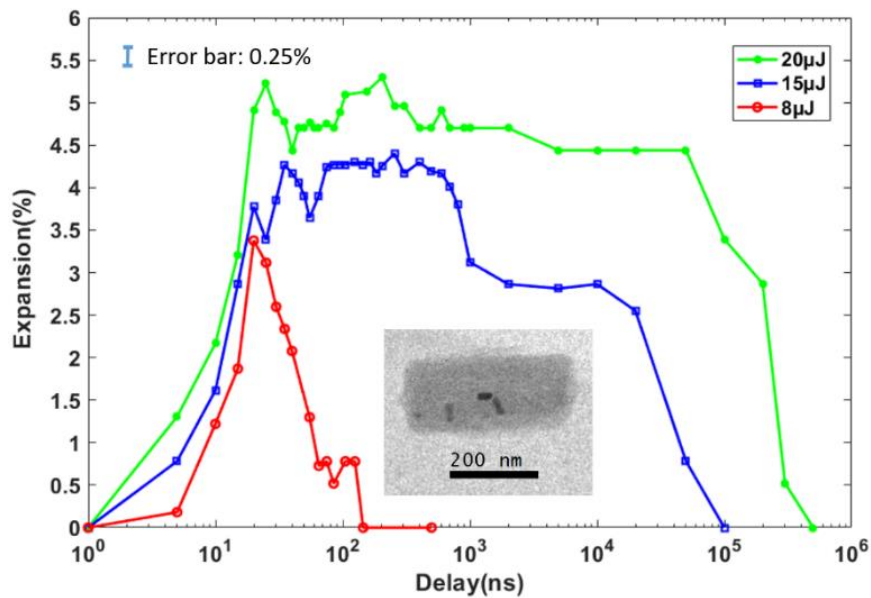


Fig. 4.16 Time-resolved length measurements of SCO@3AuNP, triggered by different laser energies.

The SCO@Au with 4 gold rods needs 500  $\mu\text{s}$  for relaxation after 8  $\mu\text{J}$  laser energy excitation, as shown in fig. 4.17. So it is obvious that more gold particles lead to longer relaxation times. Fig. 4.18 shows a comparison of the temporal behavior when different numbers of Au particles are encapsulated. With 8  $\mu\text{J}$  laser pulses, the SCO with 3 gold particles shows the fastest expansion speed whereas the expansion with one or no Au particle is slower.

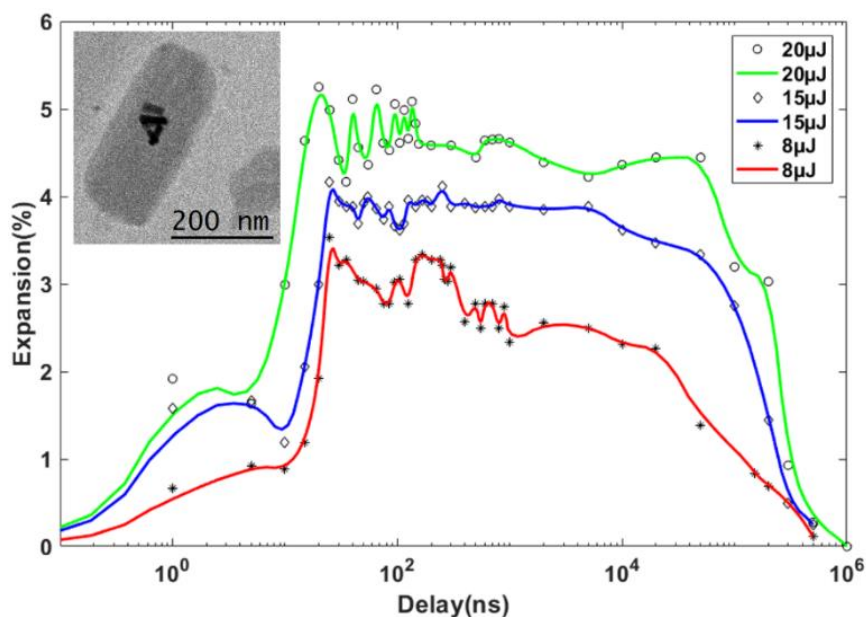


Fig. 4.17 A SCO@4AuNP triggered by different laser energies.

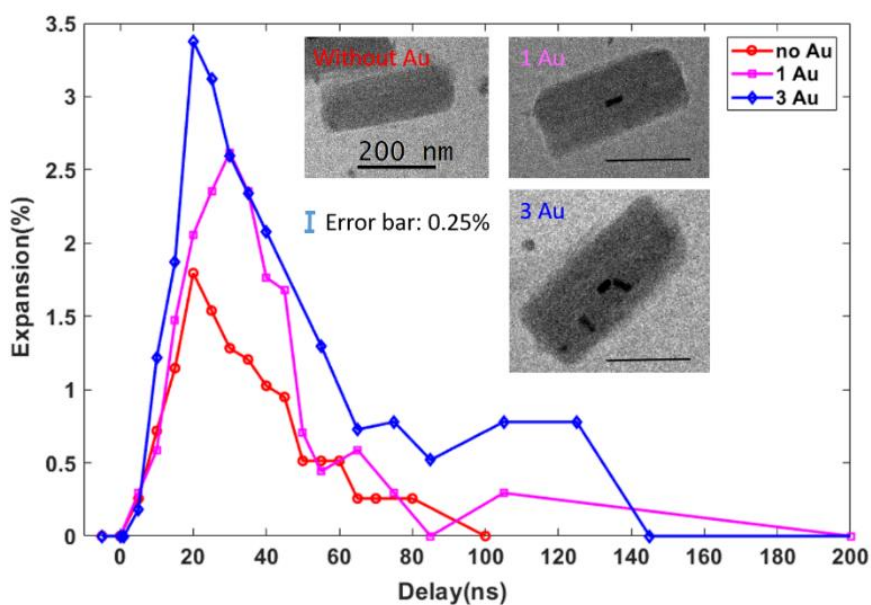


Fig. 4.18 Expansion of pure SCO and SCO@Au with one and three Au particles with the same excitation laser energy 8  $\mu\text{J}$ .

### Discussion of the results on SCO

The initial step in the excitation process is photon-electron interaction and metal-ligand charge transfer which happen from tens to hundreds of femtoseconds [76 - 78]. In this regime, there is no thermal exchange between environment and SCO particle. Therefore, no expansion of the whole crystal is expected. Since the duration of the pulses is 7 ns in our experiment and no length change occurs below a few nanoseconds, the initial step isn't visible in our measurement.

At the second step, the photo-switched molecules interact elastically, causing the cell volume expansion. Time-resolved X-ray measurements of the cell volume expansion of SCO revealed the strain wave propagation occurs at the speed of sound [74, 89]. Thus, after the initial photo-switching of individual molecules, the SCO volume expands in a self-amplified collective process by interaction between neighboring molecules. During the evolution, the volume varies in a competition between LS and HS states, called cooperative elastic interaction, which results from the lattice heating due to energy dissipation into the phonon bath. Therefore, this expansion process is not linear. Local volume compression by strain waves might happen before the expansion as seen in fig. 4.14. This phenomenon is very obvious in pure SCO. The alternating phenomenon of compression and expansion is found to range between 10 ns to 120 ns. Thus, the particle length vibrates around the maximum elongation from 120 ns to 500 ns until most molecules reached the metastable saturation state, as shown in fig. 4.14.

The third step, relaxation to thermal equilibrium, depends on the energy barrier between the LS state and the HS state until the whole SCO crystal remains temporarily in a thermal balance in the HS state. After 100  $\mu$ s, the saturation starts to decay and relaxes to the low-spin state when the particle cools, as seen in fig. 4.14, fig. 4.16, and fig. 4.17.

This is the last step which also depends on the laser intensity. When the trigger energy is 20  $\mu$ J, it needs 500  $\mu$ s, and lasts even longer if we increase the trigger energy. The

transformation of the sample back to the initial state depends on the spreading of heat to the environment which is determined by the contact of the SCO particle to the substrate which itself has to cool down after laser heating.

### Time-resolved Optical spectroscopy

The results by UTEM are now compared with optical measurements on the same samples that have been carried out by E. Freysz and his group (LOMA, Bordeaux). Fig. 4.19 (a) presents the optical transmission of a large ensemble of SCO@Au particles as a function of time at the temperature 333 K. The transmission starts increasing within few tens of nanoseconds and reaches a maximum after hundreds of nanoseconds. After 1 ms, it recovers to its initial state. Fig. 4.19 (b) presents the comparison between SCO (light blue line) and SCO@Au (red line) excited by 10 mJ/cm<sup>2</sup> laser pulses.

The SCO@Au particles have higher efficiency, due to the plasmonic heating. The optical transmission  $T(t)$  is fitted using the function  $T(t) = \Delta T (1 - \exp(-t/t_s))$  where  $\Delta T$  is the difference of transmission between initial and excited state;  $t_s$  is the switching time. Similarly, the relaxation of the transmission towards its initial value is fitted using the decay law  $T(t) = \Delta T \exp(-t/t_r)$  where  $t_r$  is the relaxation time. As displayed in Figures 4.19 (a), the data are fitted with  $t_s = 18 \pm 2$  ns and  $t_r = 410 \pm 50$   $\mu$ s. Besides, the difference in the transmission indicates that about 45% of all molecules (i.e. the HS fraction  $\gamma_{HS} \approx 45\%$ ) of the sample have switched from the LS to HS.

The same experiment was performed at 9.5 mJ cm<sup>-2</sup> and 19 mJ cm<sup>-2</sup> laser fluences, as displayed in fig. 4.19 (a) (blue and red dots). For the lowest laser fluence the switching time increases to  $\sim 250 \pm 50$  ns, the plateau remains almost the same while the relaxation rate decreases:  $t_r = 120 \pm 20$   $\mu$ s and  $70 \pm 10$   $\mu$ s for 19 mJ cm<sup>-2</sup> and 9.5 mJ cm<sup>-2</sup> laser fluences, respectively.

As shown in fig. 4.19 (b), the same experiment was repeated with a different wavelength of 470 nm, with and without embedded gold nanoparticles. The change in

$\gamma_{HS} \sim 5\%$  for the SCO sample is less compared to the change recorded for Au@SCO ( $\gamma_{HS} \sim 10\%$ ). Hence, the relaxation time recorded for the SCO ( $t_r = 12.5 \pm 1 \mu s$ ) is faster than the one for the Au@SCO ( $t_r = 65 \pm 5 \mu s$ ).

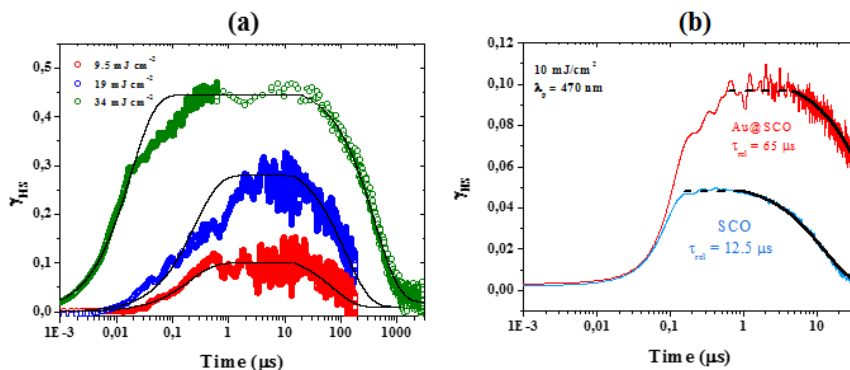


Fig. 4.19 Optical transmission measurements revealing the fraction of SCO molecules  $\gamma_{HS}$  in the HS state. (a) photoswitching of SCO@Au upon excitation by nanosecond laser with various energy; (b) comparison between SCO and SCO@Au. Adapted from Hu et al. [87]. These optical measurements were done by the group of our collaborator Eric Freysz (LOMA, Bordeaux).

### Simulation of the plasmonic light field inside the composite particles Au@SCO

Fig. 4.20 shows schematically the different types of heat transfer to the SCO particles in our experiment. The sample was excited by near-infrared (NIR) at 1064 nm. The main contribution of heating of a pure SCO particle (no Au rods) comes from heat conduction from the graphene substrate which, in turn, is also heated by the copper grid. This thermal switching processes also happened in SCO@Au, but the gold absorbs the incident laser efficiently as shown in fig. 4.21. We did finite difference time domain (FDTD) simulation with a commercial Lumerical FDTD program (a free 30 - day trial version) (<https://support.lumerical.com/hc/en-us/articles/360034914633-Finite-Difference-Time-Domain-FDTD-solver-introduction>). In this optical simulation, the gold particle size is 80 nm  $\times$  20 nm  $\times$  20 nm, and it is placed in a Cartesian coordinate origin (0, 0, 0). The gold particle is inserted in a SCO particle. The incident laser wavelength is 1064 nm. In the fig. 4.21 (a) - (c), the light (photonic near field) emerging from the Au rod is focused onto the edge of gold particle. Therefore, the

corners of gold particle concentrate the energy. So, the gold particle excites surrounding molecules with higher intensity than the incident laser. From this simulation results, we know that the gold particle in SCO not only generates the localized surface plasmon resonance, but also increases the surrounding light field, as shown in fig. 4.21 (a) - (d).

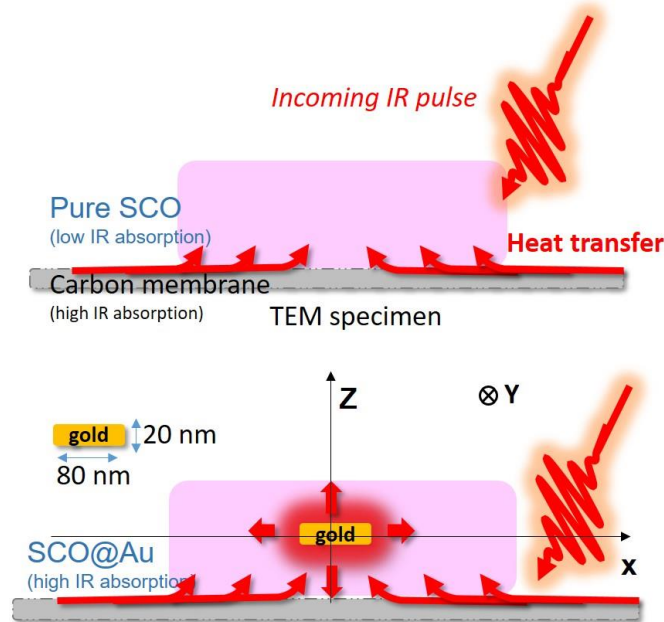


Fig. 4.20. Heat absorption of a SCO particle without and with a gold particle. The pure SCO is excited mainly by heat conduction from the underlying graphene film; the SCO@gold is excited by plasmonic heating but also from the substrate.

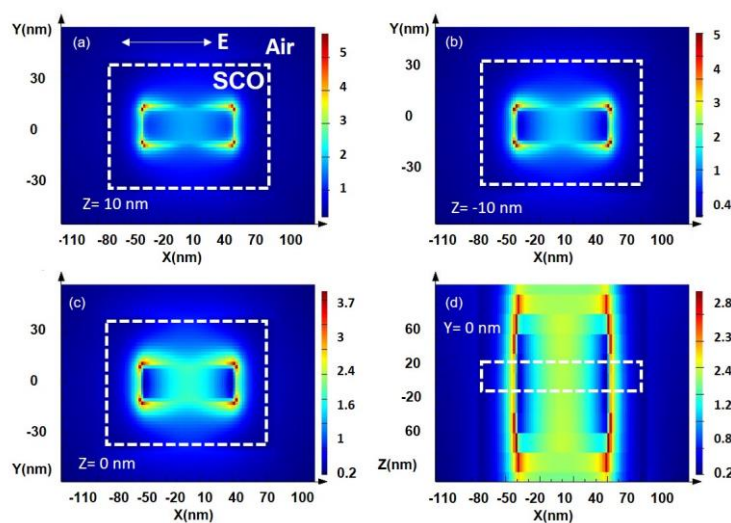


Fig. 4.21. FDTD simulation of a gold particle inserted in a SCO particle (white dashed line square): (a) light intensity distribution on the upper surface (in the plane  $Z = 10$  nm) of the gold particle; (b)

distribution on the bottom surface of gold particle (in the plane  $Z = -10$  nm); (c) distribution in the center (in the plane  $Z = 0$  nm) of the gold particle; (d) light intensity distribution in the  $Y = 0$  plane, the same viewing direction as in fig. 4.20.

Fig. 4.22 shows the simulation results with polarization direction perpendicular to the X-axis. If we define the polarization angle of  $90^\circ$  perpendiculars to X-axis, the polarization of the incident laser in fig. 4.21 is  $0^\circ$ , which is parallel to the X-axis. Obviously, even if the incident angle of the laser pulses is constant, the light intensity distribution varies with polarization angle which changes from  $0^\circ$  to  $90^\circ$ .

When the particle is anisotropic, the incident light polarization and incident angle affect the light intensity distribution. Typically, in optical experiments many randomly oriented particles are present. The directions of the axes of the SCO cannot be arranged. Fig. 4.23 shows a spherical gold particle inserted into a SCO particle. And the light distribution here is not sensitive to the polarization.

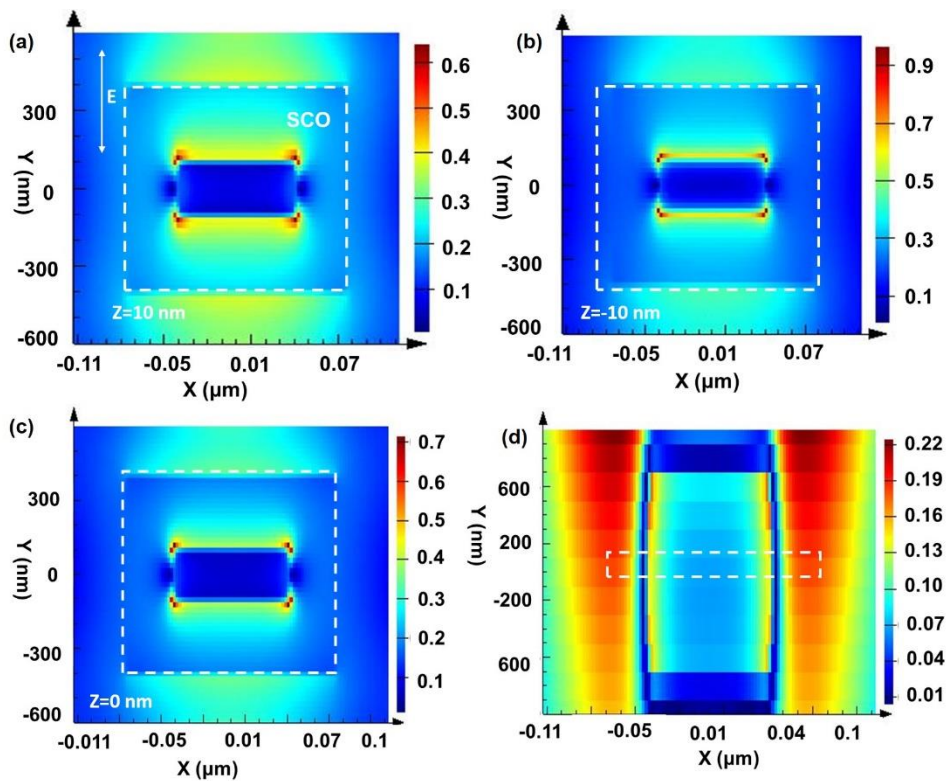


Fig. 4.22. FDTD simulation of a gold particle inserted in a SCO particle (white dashed line square):

(a) intensity distribution on the upper surface (in the plane  $Z = 10$  nm) of the gold particle; (b)

intensity distribution on the bottom surface of the gold particle (in the plane  $Z = -10$  nm); (c) intensity distribution in the center (in the plane  $Z = 0$  nm) of the gold particle; (d) light intensity distribution in of the  $Y=0$  plane, as shown in fig. 4.18.

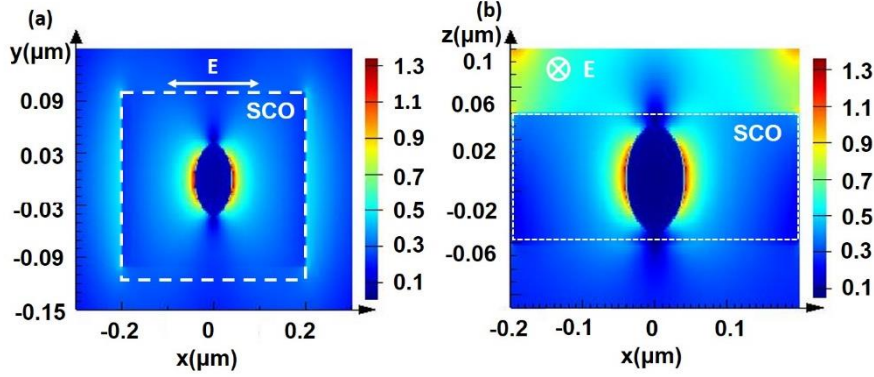


Fig. 4.23 FDTD simulation of a spherical gold particle inserted into a SCO particle: (a) light intensity distribution in the  $Z=0$  plane; (b) light intensity in the  $Y=0$  plane.

### Simulation of collective effects due to elastic interactions in the SCO particles

Simulation of elastic interactions were carried out by our collaborators Cristian Enachescu and Laurentiu Stoleriu (Iasi University, Romania) and are shown in fig. 4.24. The equations (4.1) - (4.3) describe the elastic model which was used to simulate the dynamic process after an ultrafast laser trigger [74, 75, 83, 84, 87]. The initial evolution of the system was simulated (a) by randomly creating an additional given number of HS molecules (50% in our case), whose temperature increase  $\Delta T = 300$  K is assumed to simulate a direct absorption of light by the SCO compound; (b) by the heat diffusion from a hot substrate towards the sample, or (c) by heat diffusion from 5 hot gold particles inside the SCO particle. (d) and (e) show thermal diffusion from the substrate; (f) - (g) show heat diffusion from six different gold particles.

The dynamics of the heat conduction in the system is described for every molecule  $i$  by the following differential equation

$$\frac{dT_L^i}{dt} = -\alpha \cdot (T^i - \langle T_{ij} \rangle) - \beta \cdot (T_{edge}^i - T_B) \quad (4.4)$$

Where  $\langle \rangle$  denotes the average value.

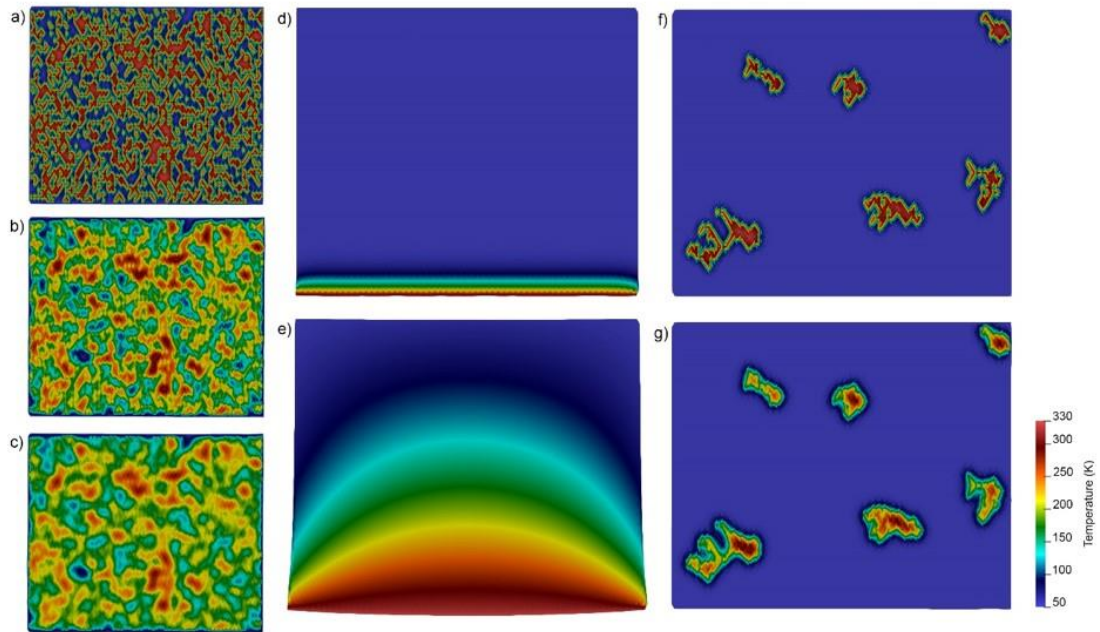


Fig. 4.24. Evolution of temperature inside the system (a)-(c): top view of a particle, heating occurs uniformly; (d) and (e): side-view: heat diffusion from a hot substrate at the bottom; (f) and (g) heat diffusion from six gold particles. Adapted from Hu et al. [87]. This simulation was done by our collaborators Cristian Enachescu and Laurentiu Stoleriu (Iasi University, Romania).

### Oscillations in the phase transition of SCO

As we see in figs. 4.14, 4.16 and 4.17, once the particle elongation along the b-axis is over 5%, where saturation is reached, the particle shows an obvious vibration. This hasn't been seen in any other experiment on spin-crossover materials before, most likely because all techniques hitherto have averaged over a large number of SCO particles. The behavior is shown in detail in fig. 4.25, where at the timescale 1 ns ~ 50 ns, the length oscillates by repeated expansion and compression periods. E.g., at 25 ns and 40 ns, the particle shrinks temporarily. At 55 ns, the particle elongation is saturated around 5.5%. However, it still fluctuates around 5%, and the amplitude gradually increases. At 185 ns, it reaches to 6%. At last, the SCO molecular system and the environment reach thermal equilibrium at 1  $\mu$ s where the oscillation is dampened and disappears. The elongation remains around 5%. From 20  $\mu$ s to 200  $\mu$ s, the particle relaxes gradually back to its initial state.

When we further increased the incident laser energy to the limit where the SCO particle is damaged, the particle reached the maximum around 6.3% at 25 ns. And after 2 cycles, the particle evaporated. So in the 1064 nm and 7 ns photo-thermal excitation, 30  $\mu$ J pulses are already over the thermal damage threshold of SCO.

Preliminary (unpublished) Monte Carlo simulation results from our collaborator C. Enachescu and L. Stoleriu (Iasi University, Romania) reproduce well our observations. They show that the elastic step of the expansion leads to energy dissipation into phonons. The excited molecules (HS) have more energy and transfer it to their neighbor molecules. In their simulation, the HS molecules are at 335 K. The vibration process is due to the energy transition process. After 1  $\mu$ s, the system relaxes back to the ground state. It is therefore an interplay between the elastic forces in the particle that lead to the oscillations. Size effects should also be important but haven't been studied yet. We expect that the oscillation frequency increases with decreasing size of the particle. This hasn't been studied yet, but more detailed work on this new phenomenon is in progress and a publication is in preparation.

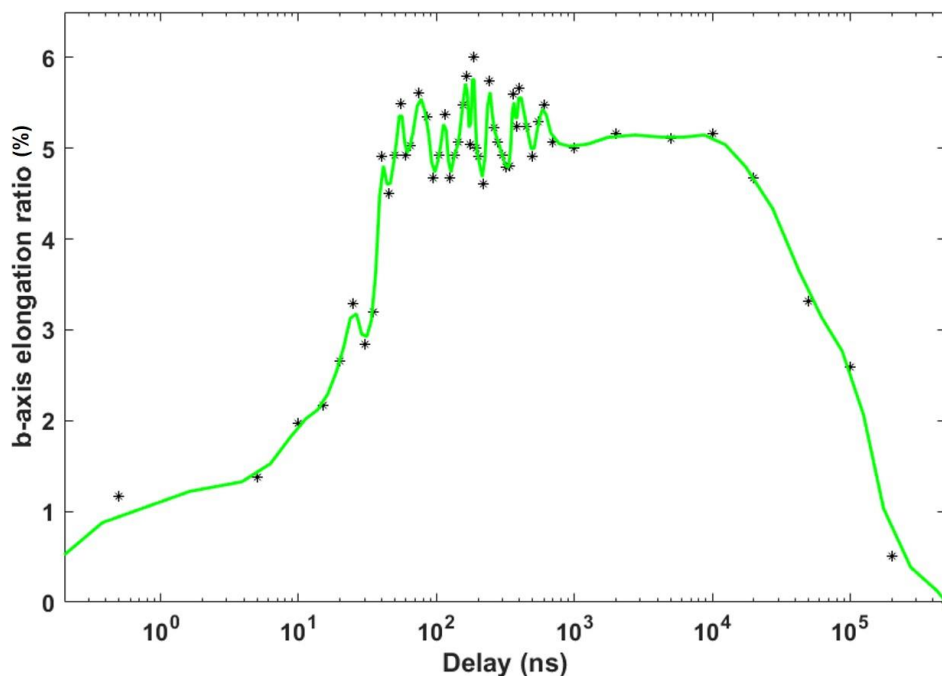


Fig. 4.25 Length oscillation of a pure SCO particle (initial length 599 nm) under 26  $\mu$ J laser pulse excitation.

## 4.5 Conclusion

In this part of the thesis, single SCO particle excitation was studied under static heating and in time-resolved experiments to measure the photo-thermal behavior quantitatively in the UTEM. The volume expansion of SCO particles is due to a gradual transition of the molecules from the low-spin to the high-spin state. In the UTEM studies, the expansion along the b-axis is our major parameter, and up to 5.1% elongation has been observed. The width of the thermal hysteresis is around 40 K. The influence of the magnetic field in the objective lens causes only a minor shift of the hysteresis loop towards lower temperature compared with susceptibility measurements. The SCO@Au particles show similar overall expansion in thermal equilibrium. In time-resolved experiments, pure SCO particles expand after 10 ns and reach their maximum expansion at 120 ns. The SCO@Au particles show a faster expansion rate, reaching the maximum expansion already within 20 ns. This is due to the efficient heating of SCO by the embedded plasmonic gold particles. After some hundred nanoseconds, the particle remains at maximum expansion up to 80  $\mu$ s. The particle needs hundreds of microsecond to cool down and to relax into the low-spin state in the particular setup of our experiments. A stronger thermal coupling to the environment would lead to a faster relaxation of the SCO particles. One complete cycle from excitation to relaxation happens within 1 ms.

Furthermore, when the incident laser energy is over 20  $\mu$ J and the particles expand to saturation, an oscillation of their elongation around 5% is getting obvious. This is a new collective phenomenon in SCO particles that needs a more detailed study. At average intense IR laser pulses around 30  $\mu$ J (1064 nm), the particle reaches its maximum elongation within 25 ns. But this is close to the damage threshold where the particle is damaged and evaporates.

## Chapter 5

### Photo-reversible phase transition in $\text{Ti}_3\text{O}_5$

#### Contents

<a href="#">Chapter 5</a> .....	65
<a href="#">Photo-reversible phase transition in <math>\text{Ti}_3\text{O}_5</math></a> .....	65
<a href="#">5.1 Crystal structure and electronic states in <math>\text{Ti}_3\text{O}_5</math></a> .....	66
<a href="#">5.2 Thermal phase transformations in <math>\text{Ti}_3\text{O}_5</math> observed by TEM</a> .....	69
<a href="#">5.3 Photo-excited phase transition in TEM</a> .....	75
<a href="#">5.4 Previous time-resolved experiments by optical techniques</a> .....	80

This study is being carried out in collaboration with Maciej Lorenc's group (University of Rennes). The specimens delivered by the Rennes group were synthesized by ball milling by the group of S. Ohkoshi at the University of Tokyo. This chapter describes preliminary work in the context of a more extended study of light-induced phase transitions by imaging, diffraction and EELS in the UTEM.

## 5.1 Crystal structure and electronic states in $\text{Ti}_3\text{O}_5$

$\text{Ti}_3\text{O}_5$  is the first metal oxide showing bistability in two phases at room temperature where laser pulses can be used for switching between the two phases. In other words, it is a photorewritable material allowing permanent photoinduced phase transitions at room temperature. This suggests that  $\text{Ti}_3\text{O}_5$  nanoparticles have potential applications in optical memories and novel heat storage devices [90, 91]. Before the first report of photorewritable properties at room temperature, the phase transitions in  $\text{Ti}_3\text{O}_5$  had been studied [90 - 93]. At room temperature, crystalline  $\text{Ti}_3\text{O}_5$  may exist in either the  $\beta$ -phase or the  $\lambda$ -phase, both having the same monoclinic structure and space group  $C2/m$  but different lattice parameters [90]. Thus, a transition between these two phases is accompanied with a change of crystal size. The  $\alpha$ -phase is a third stable phase which exists at higher temperature.

The crystal structure and electronic states of  $\text{Ti}_3\text{O}_5$  have been studied through X-ray diffraction, magnetic measurements, and transport measurements [90, 93, 94]. The transition between the  $\beta$ -phase and the  $\alpha$ -phase undergoes first-order structural and magnetic-nonmagnetic transitions at 460 K. The  $\beta$ -phase is a semiconductor with conductivity  $\sigma = 3 \times 10^{-2}$  S/cm and band gap of 0.14 eV [90]. The transition between the  $\lambda$ -phase and the  $\alpha$ -phase is classified as a second-order phase transition [93]. The  $\lambda$ -phase has a magnetic susceptibility of  $\chi = 2 \times 10^{-4}$  emu per Ti atom and a conductivity  $\sigma = 30$  S/cm [90, 93]. From an electronic standpoint, the semiconductor-to-metal

transition can be treated as a vanishing of the band gap due to a  $\text{Ti}_3 - \text{Ti}_3$  dimer dislocation [94] as shown in the fig. 5.1 (a) and (b). In the  $\beta$ -phase, the  $\text{Ti}_3 - \text{Ti}_3$  dimers are sharing the electrons on a band below and near the Fermi level. The band gap is 0.13 ~ 0.14 eV in the  $\beta$ -phase [90].

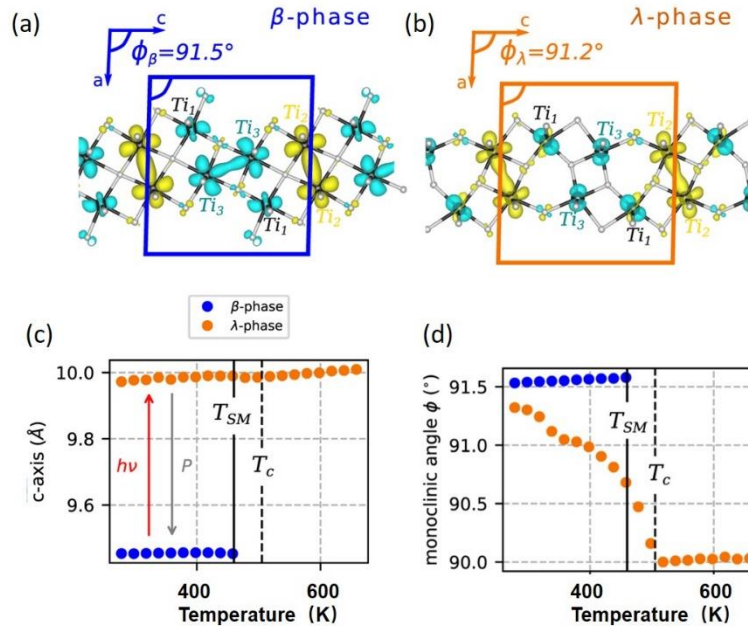


Fig. 5.1 (a)  $\text{Ti}_3\text{O}_5$ : crystal structure of  $\beta$ -phase; (b)  $\lambda$ -phase;  $\Phi_\beta$  and  $\Phi_\lambda$  are the monoclinic angles of the  $\beta$  and  $\lambda$  unit cells; (c) crystal parameter change between  $\beta$  and  $\lambda$  unit cells along the c-axis; (d) monoclinic angle change between  $\beta$  and  $\lambda$  unit cell. The critical temperature is  $T_c=500\text{K}$ . Adapted from Mariette et al [94].

The phase transition from the semiconductor to the metal phase in  $\text{Ti}_3\text{O}_5$  is accompanied by a volume change between the  $\beta$ -phase and the  $\lambda$ -phase [94]. The increase of volume from  $\beta\text{-Ti}_3\text{O}_5$  to  $\lambda\text{-Ti}_3\text{O}_5$  results from an increasing c-axis, as shown in the fig. 5.1(c) and (d) which shows that the c-axis expansion and the difference in monoclinic angle depend on temperature. At a critical temperature  $T_c = 500\text{K}$ , the second order phase transition occurs from  $\lambda\text{-Ti}_3\text{O}_5$  towards to the  $\alpha$ -phase which is metallic and has an orthorhombic space group  $\text{Cmcm}$ . This transition is ferroelastic

when the crystal structure changes from monoclinic to orthorhombic. The c-axis parameter and monoclinic angle don't change.

Under thermal excitation,  $\text{Ti}_3\text{O}_5$  undergoes a phase transition from  $\beta\text{-Ti}_3\text{O}_5$ , which is energetically favorable, to the metastable  $\lambda\text{-Ti}_3\text{O}_5$  phase in a local configurational energy minimum [90], as shown in fig. 5.2. The  $\lambda\text{-Ti}_3\text{O}_5$  can be switched back to the initial  $\beta\text{-Ti}_3\text{O}_5$  through an intense nanosecond laser pulse. This photoinduced phase transition can be manipulated by controlling the incident laser energy and wavelength [90, 95] or by external pressure 0.5 GPa [96].

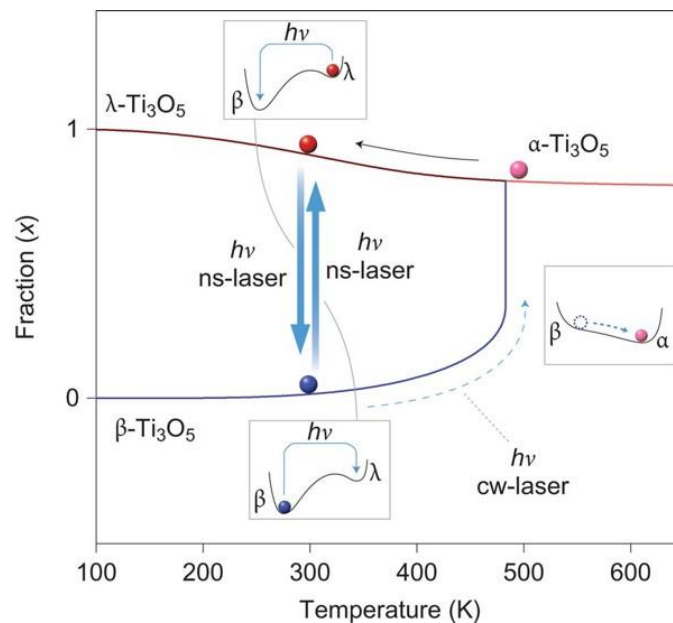


Fig. 5.2 Laser-induced phase transitions between  $\beta\text{-Ti}_3\text{O}_5$  and  $\lambda\text{-Ti}_3\text{O}_5$ ; phase versus temperature curves are based on Gibbs free energy calculations. Adapted from Ohkoshi et al [90].

When crystalline flakes of  $\lambda\text{-Ti}_3\text{O}_5$  are irradiated by nanosecond laser pulses with 532 nm, 6 ns,  $1.5 \times 10^{-5} \text{ mJ } \mu\text{m}^{-2}$ , and 5 shots, according to Ohkoshi's report, the sample color changed from black to brown. The brown area is the  $\beta\text{-Ti}_3\text{O}_5$  phase which was demonstrated by XRD. After 410 nm laser irradiation, the color changed from brown to black. This transformation can be repeated by using the wavelengths 355 nm and 1064 nm [90]. Using the same wavelength 532 nm but with different intensity can also induce

the phase switching between  $\beta$ -Ti<sub>3</sub>O<sub>5</sub> and  $\lambda$ -Ti<sub>3</sub>O<sub>5</sub>. The transformation  $\beta$ -Ti<sub>3</sub>O<sub>5</sub>  $\rightarrow$   $\lambda$ -Ti<sub>3</sub>O<sub>5</sub> needed  $2.7 \times 10^{-6} \text{ mJ } \mu\text{m}^{-2}$ , but the reverse process needed at least  $7 \times 10^{-6} \text{ mJ } \mu\text{m}^{-2}$ . The difference in laser power density for switching in the two directions suggests a cooperative interaction between photo-excited domains and neighboring unexcited domains [90]. As shown in fig. 5.2, below 460 K, the  $\beta$ -Ti<sub>3</sub>O<sub>5</sub> phase is the stable ground state through the thermodynamic analysis of the phase transitions in Ti<sub>3</sub>O<sub>5</sub>.

## 5.2 Thermal phase transformations in Ti<sub>3</sub>O<sub>5</sub> observed by TEM

In the TEM, we can observe and measure the crystal rearrangement and lattice parameter changes. This is the most straightforward way to demonstrate how a phase transition occurs. Fig. 5.3 presents the image under high magnification.

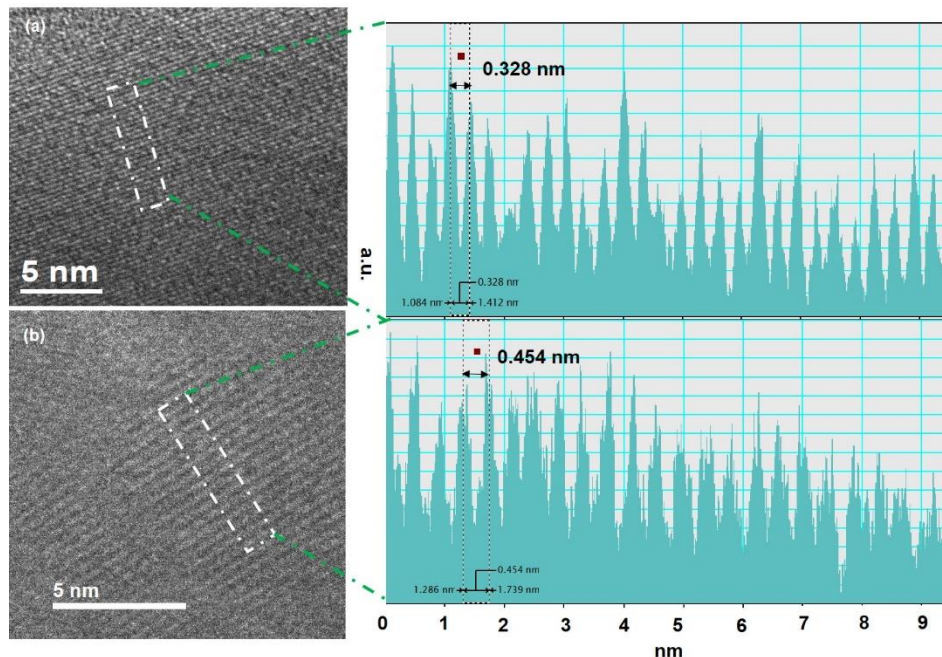


Figure 5.3 (a) lattice image of Ti<sub>3</sub>O<sub>5</sub> at room temperature and before heating; (b) lattice image of Ti<sub>3</sub>O<sub>5</sub> at room temperature and after heating; the right side shows the contrast profile of the images.

An intense electron beam can damage the structures, as shown in fig. 5.3 (b). The crystal image gradually blurs and finally disappears. In our experiment in the heating stage, the measured area was always shifted when the temperature was changed to avoid radiation damage, and it is sometimes hard to find back to the initial area.

Our initial goal is measuring the structural dynamics of the switching between the  $\beta$  and the  $\lambda$  phase. This process normally happens at the nanosecond or microsecond timescale. Time-resolved measurements need the accumulation of a large number of electron counts. And the  $\lambda$ -phase of  $\text{Ti}_3\text{O}_5$  particles needs an external excitation to switch back to the initial  $\beta$ -phase (the conditions for switching in the two directions are different). Considering the equipment available in our lab, a much more complex synchronization between pump laser and probe laser would have to be installed, in particular since two pump lasers might be needed. Even with this synchronization, the laser-triggered phase transition for electron accumulation in the stroboscopic mode should occur very stably in many cycles.

Therefore, in our experiment, we couldn't carry out a time-resolved measurement of the crystal structure rearrangement and the phase transitions yet. Here, we propose that once the crystal constant and orientation change, this will cause a change of the whole particle size and shape. And in a reversible phase transition, these processes should be reversible.

As described in section 5.1, the unit cell of the  $\text{Ti}_3\text{O}_5$  crystal has a larger expansion in the c-axis direction. In the TEM, we can analyze the nanoparticle morphology and corresponding diffraction patterns to study the  $\text{Ti}_3\text{O}_5$  phase transition. The oxide particles were dispersed in ethanol, followed by supersonic stirring, and deposited on amorphous carbon film. The nanoparticle orientation and distribution is random.

Since the lattice parameters of these two phases are different, the particle changes its size during the transition. We used imaging to measure the particle size change between different phases. Fig. 5.4 shows the particle that we picked to measure the size change. The temperature cycle went through the steps RT (a)  $\rightarrow$  623 K (b)  $\rightarrow$  RT

(c). In this particular projection, no measurable size changes are visible between the  $\beta$ - and  $\lambda$ -phase whereas a slight expansion appears in the  $\alpha$ -phase in the vertical direction. However, according to the reported results [5], the volume should have 6% difference between  $\beta$ -phase and  $\lambda$ -phase. So, a randomly picked particle direction doesn't necessarily show the expansion.

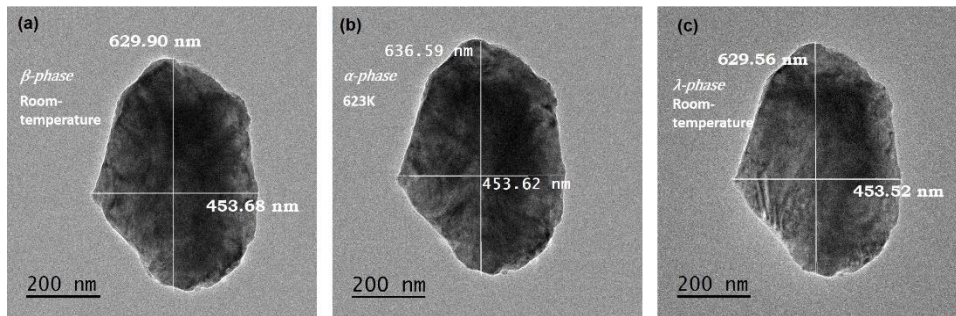


Fig. 5.4 A randomly selected  $\text{Ti}_3\text{O}_5$  particle: (a) initial state at room temperature; (b) the particle in the heating stage at 623 K; (c) particle after cooling back to room temperature. The respective phases are indicated.

As reported in X-ray diffraction data of  $\text{Ti}_3\text{O}_5$  powder [5], the  $\beta$ -phase reflection (2 0 1) disappears in the phase transition to  $\lambda$ . This shows that the crystal structure changes. In powder diffraction, all orientations appear, and the diffraction pattern is an important reference.

The particles are of irregular shape, as shown in fig. 5.5. The profile in fig. 5.5 presents the elongation in different directions. This changes in size was measured as a function of temperature. Fig. 5.5 shows the size of a nanoparticle before heating and after cooling. The experiments were carried out with a heated stage in thermal equilibrium. In the experiment, we always picked out those particles' diffraction patterns where the (2 0 1) diffraction spots appeared because this diffraction peak disappears in the phase transition from  $\beta$ -phase to  $\lambda$ -phase. For a convenient observation, the particle should be a single crystal.

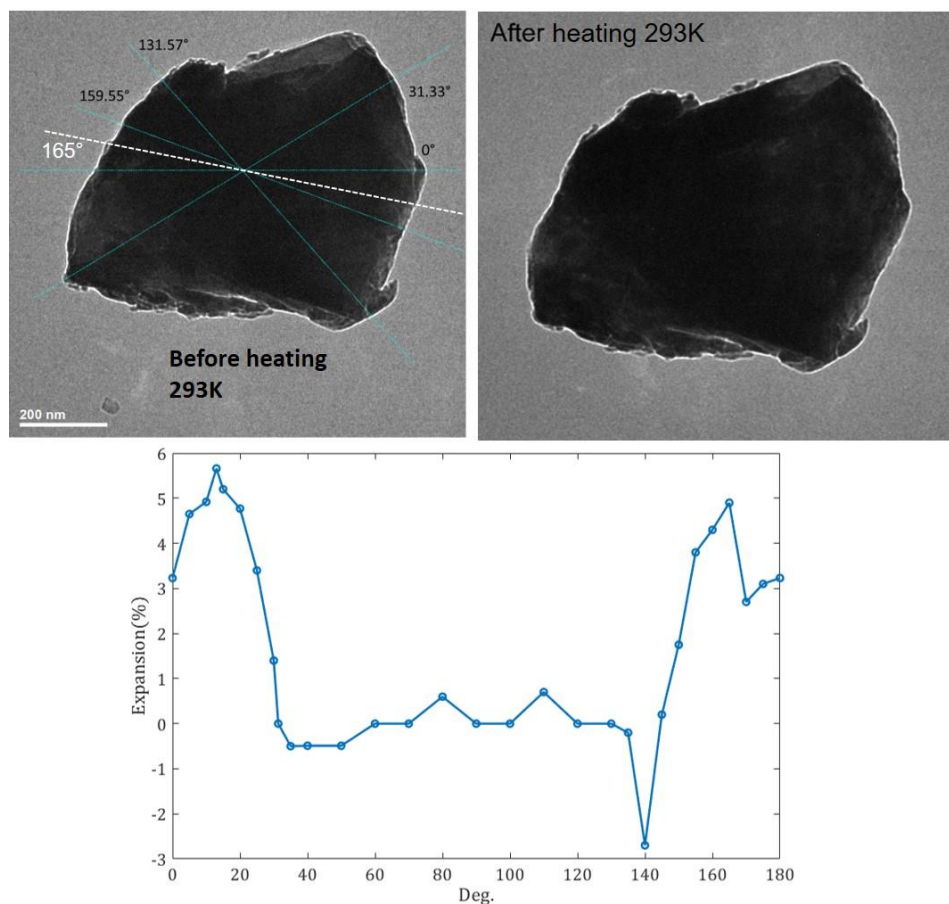


Fig. 5.5. The morphology of a  $\text{Ti}_3\text{O}_5$  crystal in the top images (left: pristine crystal before heating, right: same crystal after heating to 623 K and cooling back to room temperature); the bottom shows the elongation ratio between the particle's initial state and after heating and cooling back to room temperature. The reference direction  $0^\circ$  is the horizontal.

The particle in Fig. 5.5 shows the maximum expansion along the direction at  $15^\circ$  and  $165^\circ$  relative to the horizontal line ( $0^\circ$ ). The length measurement as a function of temperature is shown in fig. 5.6 for a heating-cooling cycle. In the curve of heating and cooling, the different points are marked where the phases can be identified by diffraction. The state 1 is the initial state where the crystal is in the  $\beta$ -phase. When we heated it to 623 K, as shown in the fig. 5.6, the diffraction pattern changed (point 2) and can be identified as the  $\alpha$ -phase. During the successive cooling processes, at point 4 the  $\lambda$ -phase appears according to the corresponding diffraction pattern. When the temperature was decreased to 293 K, the particle in this direction remained at the expansion of 4.6%. According to the diffraction patterns, between

the state 1 and state 4 the (2 0 1) and (2 0 -1) reflections are rotated. The contour of the particle in the  $\beta$ -phase and  $\lambda$ -phase are presented in the fig. 5.6.

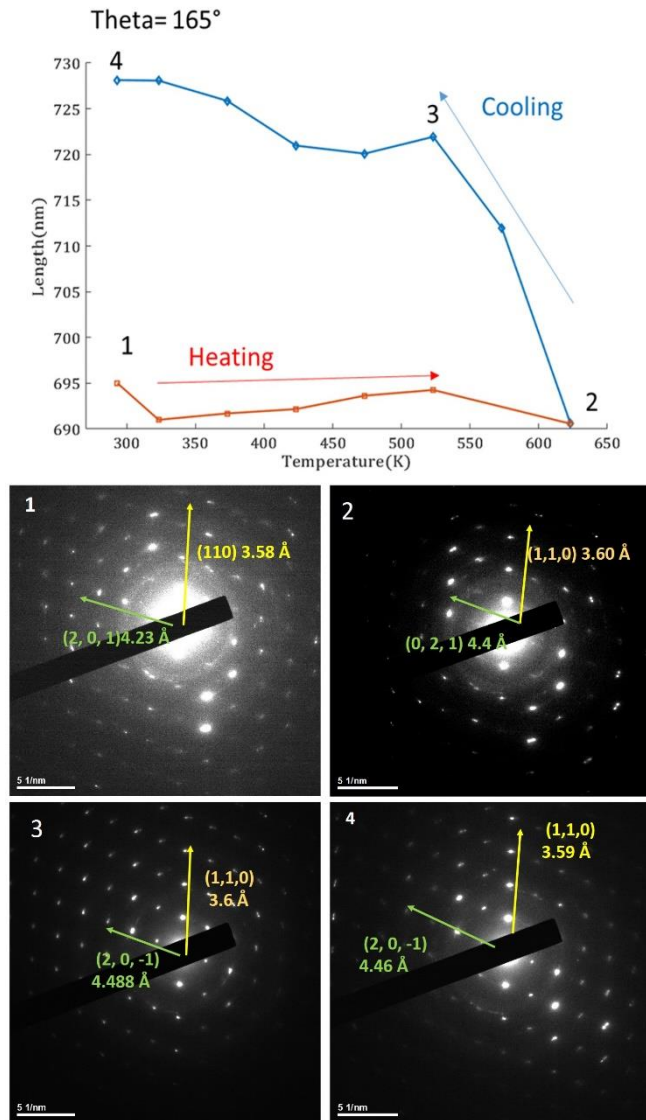


Fig. 5.6. top shows the particle elongation in the 165° direction (see Fig. 5.5); the 1, 2, 3, and 4 are the diffraction patterns at the corresponding points.

We reproduced the experiment with other particles, as shown in fig. 5.7. The particle morphology has an obvious change from the  $\beta$ -phase to the  $\alpha$ -phase in the heating experiment at 623 K. The diffraction patterns show an obvious difference. According to the known d-spacing, the diffraction pattern at high temperature is in accordance with the  $\alpha$ -phase. Fig. 5.7 (c) shows the  $\lambda$ -Ti<sub>3</sub>O<sub>5</sub> particle. In order to describe the

whole expansion, the projected area in the image of the particles has to be calculated.

The elongation and the area of the particle in the projection are shown in fig. 5.8. The elongation along the blue line in fig. 5.7 is plotted as a function of temperature. While the first cycle led to a permanent transformation, in the second cycle, the transition is reversible between the  $\lambda$ -phase and  $\alpha$ -phase, as shown in fig. 5.8 (b) and (d). There is a hysteresis with a width of 15 K between the  $\lambda$ -phase and  $\alpha$ -phase in the heating and cooling processes, as shown in the fig. 5.8 (b). The projected area in the transition from the  $\beta$ -phase to the  $\lambda$ -phase has around 6% difference. Fig. 5.8 (c) is the first cycle heating experiment, and fig. 5.8 (d) is the second-cycle heating.

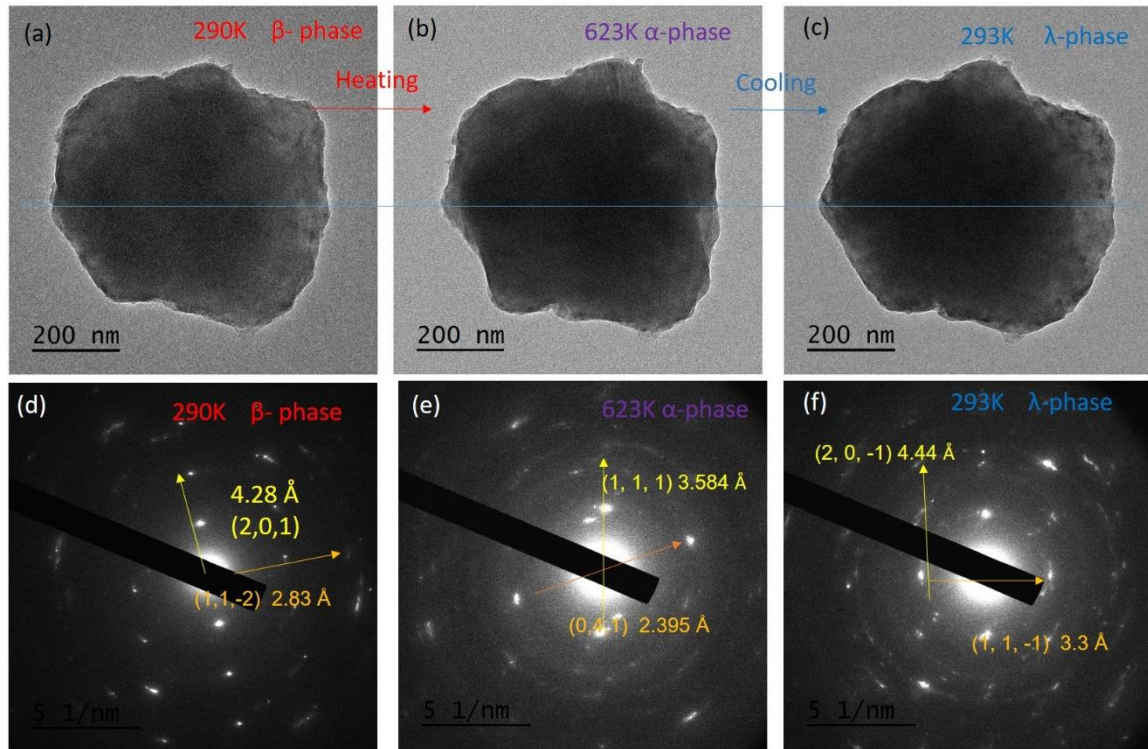


Fig. 5.7. Phase transformations of  $\text{Ti}_3\text{O}_5$ : (a) the  $\beta$ - $\text{Ti}_3\text{O}_5$  phase is the initial state at room temperature; (b) transformation to the  $\alpha$ -phase at 623 K; (c) cooling to room temperature; the particle is in the  $\lambda$ -phase; (d), (e) and (f) shows the diffraction pattern of (a), (b) and (c) respectively.

Because the metastable  $\lambda$ - $\text{Ti}_3\text{O}_5$  phase is trapped in a local configurational energy minimum, the transition to the  $\beta$ -phase can be induced through heating. So the second cycle heating could be considered as a second-order phase transition [93]. As shown in the fig. 5.8 (d), the area doesn't change anymore in the second cycle. This demonstrates that our samples in the initial state are in the  $\beta$ -phase, and the projected area can be used as a parameter to describe the phase transition in our experiments.

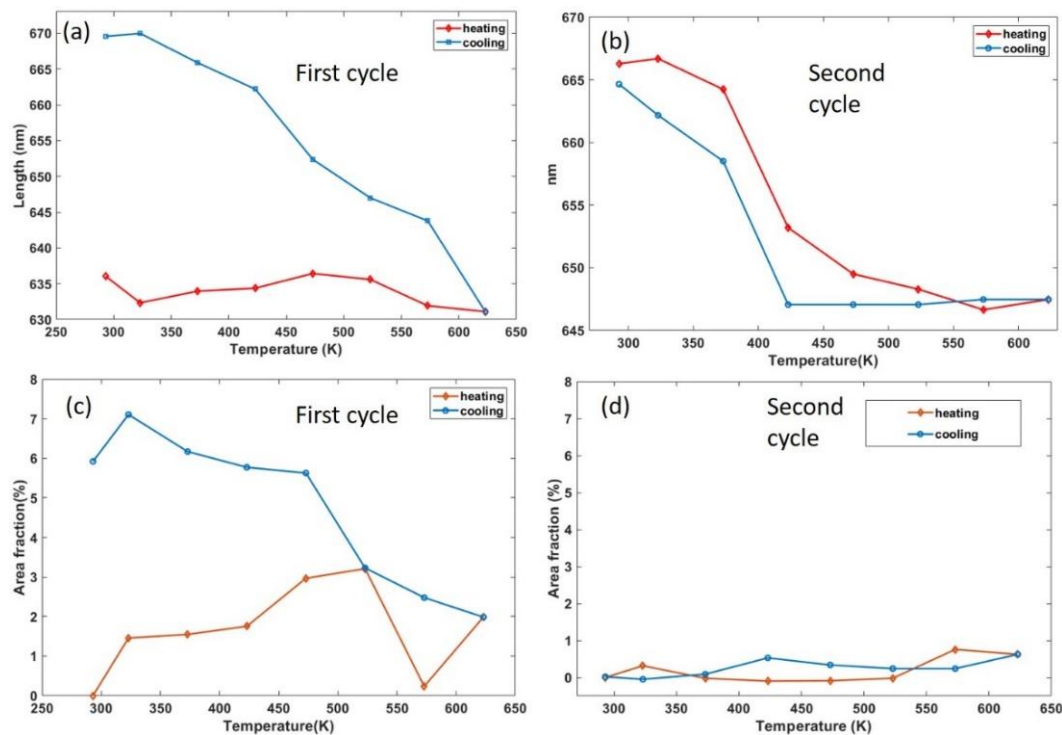


Fig. 5.8. (a) the elongation of the particle along the horizontal line of Fig. 5.7 as a function of temperature in the first cycle; (b) elongation in the second cycle heating; (c) projected area as the function of temperature in the first cycle; (d) projected area in the second heating cycle;

### 5.3 Photo-excited phase transition in TEM

Here we study the phase transitions under laser pulses. In the laser experiment, we employed pulses at 1064 nm (1.2 eV and 7 ns). To check the mechanical stability under laser pulses, a particle was exposed to pulses repeatedly. As shown in fig. 5.9, after 3 laser shots, the particle shows a different projected profile. But after several

shots, the particle doesn't seem to move anymore. So this difference in profile results from the rotation which is caused by the laser shots.

Considering this problem, the measured particle shapes in the  $\beta$ -phase and  $\lambda$ -phase should be acquired and known before laser excitation and the shapes and the particle phases have to be identified.

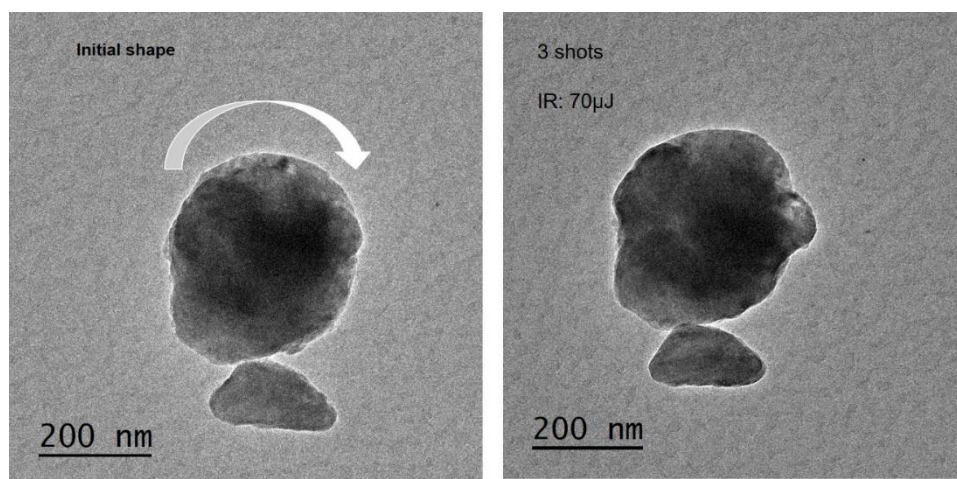


Fig. 5.9 Rotation of a  $\text{Ti}_3\text{O}_5$  particle after laser pulse excitation.

In the experiment, two heating cycles are employed in order to make sure that the measurements are not affected by rotation effects and to image the phase transition with obvious volume change.

Due to the band gap of 0.14 eV in the  $\beta$ -phase, the absorption in the near-infrared is high enough for laser excitation. In fig. 5.10 the phase transition between the  $\beta$ - $\text{Ti}_3\text{O}_5$  phase and  $\lambda$ - $\text{Ti}_3\text{O}_5$  phase is shown. After two heating cycles in a heating stage, the particle is in the  $\lambda$ -phase, as shown in fig. 5.10 (a) and (d).

The particle in the  $\lambda$ -phase, as shown in fig. 5.10 (a) and (d), is triggered by a laser pulse with  $2.8 \text{ mJ/cm}^2$  and transformed to the  $\beta$ -phase, as shown in fig. 5.10 (b) and (e). The particle in the  $\beta$ -phase is triggered by another laser pulse with  $2.4 \text{ mJ/cm}^2$  and transforms back to the  $\lambda$ -phase again, as shown in the fig. 5.10 (c) and (f). When we further increased the laser energy, the particle evaporated.

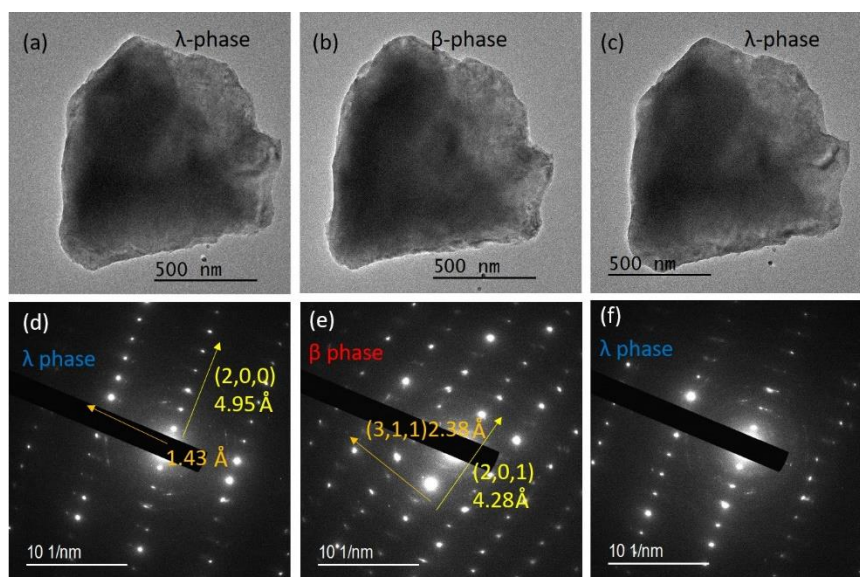


Fig. 5.10 (a) the particle after a heating cycle is in the  $\lambda$ -phase; (b) the particle after one laser shot is in the  $\beta$ -phase; (c) the particle after another laser shot is transformed back to the  $\lambda$ -phase; (d), (e) and (f) are diffraction pattern of (a), (b) and (c) respectively.

In order to reproduce the photo-induced reversible process, another particle in the  $\beta$ -phase with a clearly visible (2 0 1) reflection was picked, as shown in fig. 5.11 (a) and (d). After two heating cycles, the morphology changes slightly in fig. 5.11 (b), and the diffraction pattern in fig. 5.11 (e) shows that it has transformed to the  $\beta$ -phase. With a laser shot, the particle was transformed back to the  $\lambda$ -phase, as shown in fig. 5.11 (c), according to the diffraction pattern of fig. 5.11 (f). After heating and laser triggering, shown in Fig. 5.11 (c) and (f), the crystalline perfection of the particle has increased and it seems to be a single crystal. In the experiments, all particles have almost single crystal perfection, making the results more reliable and reproducible. As shown in fig. 5.12, the same particle under laser trigger underwent a reversible transition. The particle was triggered by laser shots in several cycles. Here, the aim is to search a relationship between laser energy and phase transition. The threshold for the transition from the  $\beta$ -phase to the  $\lambda$ -phase was found to be in the range from 2.4 mJ/cm<sup>2</sup> to 4 mJ/cm<sup>2</sup>. The threshold for the reverse transition from the  $\lambda$ -phase to the  $\beta$ -phase was in the range from 3.4 mJ/cm<sup>2</sup> to 5.2 mJ/cm<sup>2</sup>. This indicates that the switching direction between the two phases can be controlled by the power of the laser pulse.

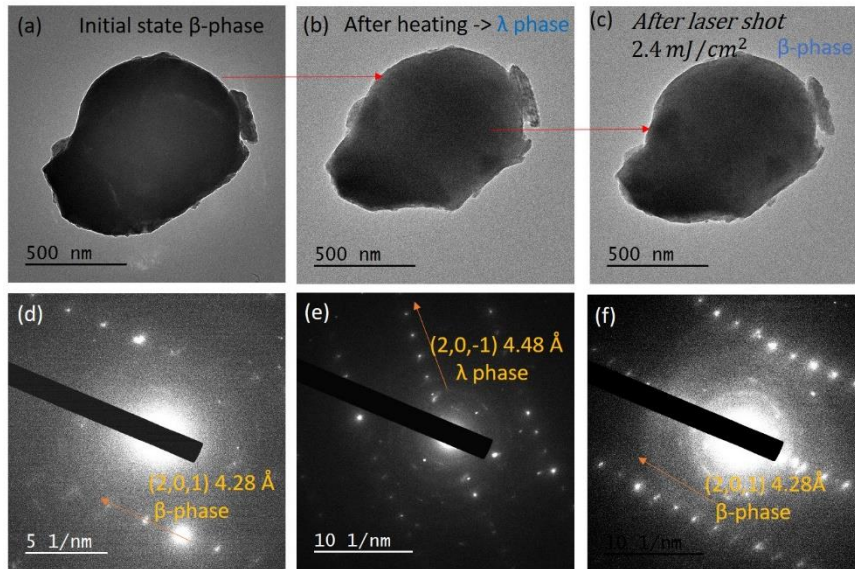


Fig. 5.11. (a) the initial state in the  $\beta$ -phase; (b)  $\lambda$ -phase after two-cycle heating in a heating stage; (c) the particle after a laser trigger is back in the  $\beta$ -phase; (d), (e) and (f) are the diffraction patterns of (a), (b) and (c) respectively.

After showing that reversible switching of  $\text{Ti}_3\text{O}_5$  is possible by IR pulses, further experiments were done with green laser pulses (532 nm, 7 ns). Fig. 5.13 (a) shows the initial state of  $\beta\text{-Ti}_3\text{O}_5$ , and (e) is the corresponding diffraction pattern. The fig. 5.13 (b) - (d) show the result of green laser pulses (2.33 eV and 7 ns). The fig. 5.13 (b) was taken after a laser pulse energy below the threshold for the phase transition between  $\beta$ -phase and  $\lambda$ -phase. According to the 5.13 (f), the particle should have undergone a phase transition; however, the identification wasn't unambiguous. After another pulse with higher energy density  $0.91 \text{ mJ/cm}^2$ , according to the diffraction pattern fig. 5.13 (g), the  $\lambda$ -phase was identified, as shown in fig. 5.13 (c) and (g). After a pulse with  $1.13 \text{ mJ/cm}^2$ , the particle is shown fig. 5.13 (d) but, as shown in fig. 5.13 (h), the particle has already started melting or transforming to an amorphous phase. A transformation back to the initial state wasn't possible anymore. According to the results with green pulses, the  $\text{Ti}_3\text{O}_5$  particle seems more sensitive at 532 nm wavelength. The damage threshold for 532 nm wavelength is around  $0.9 \sim 1 \text{ mJ/cm}^2$ . If thinner particles are used, this value can decrease to around  $0.7 \text{ mJ/cm}^2$ .

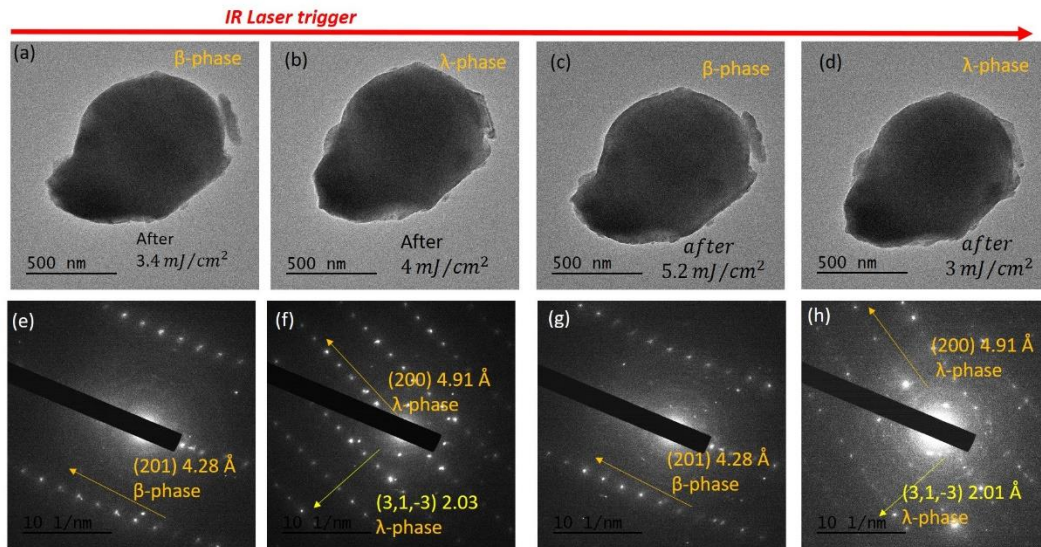


Fig. 5.12, multi-cycle phase transitions between  $\beta$ -phase and  $\lambda$ -phase induced by IR pulses: (a) particle in the  $\beta$ -phase after a  $3.4 \text{ mJ/cm}^2$  laser shot; (b)  $\lambda$ -phase with  $4 \text{ mJ/cm}^2$ ; (c)  $\beta$ -phase after  $5.2 \text{ mJ/cm}^2$ ; (d)  $\lambda$ -phase after  $3 \text{ mJ/cm}^2$ ; (e), (f), (g), and (h) are diffraction patterns of (a), (b), (c), and (d) respectively.

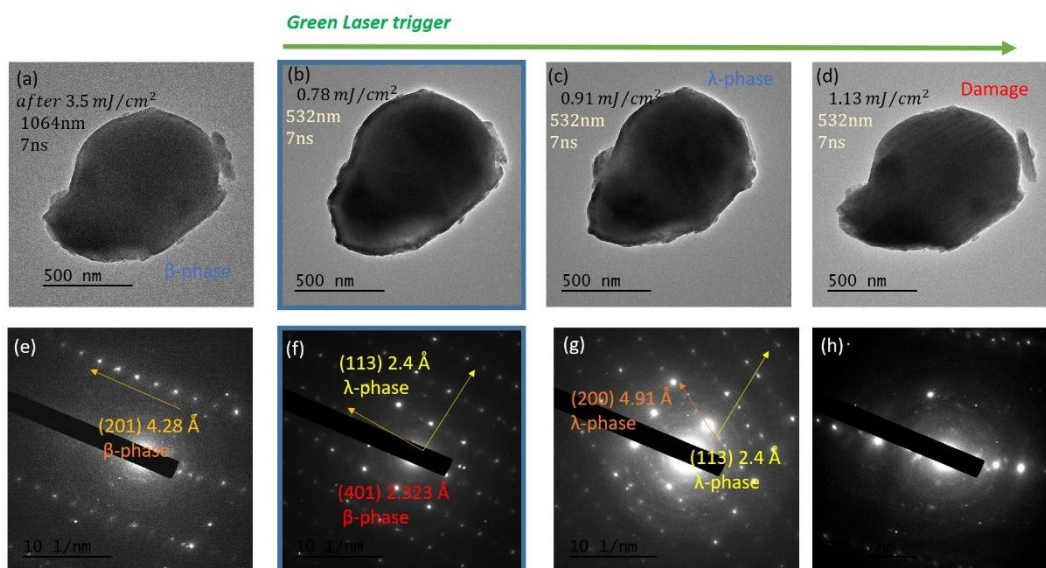


Fig. 5.13. (a)  $\beta$ -phase after an IR  $3.5 \text{ mJ/cm}^2$  laser shot; (b) the particle after a green laser shot with  $0.78 \text{ mJ/cm}^2$ ; (c) the particle after another shot with  $0.91 \text{ mJ/cm}^2$ ; (c) particle in the  $\lambda$ -phase; (d) the damaged particle after  $1.13 \text{ mJ/cm}^2$ .

## 5.4 Previous time-resolved experiments by optical techniques

The dynamics of the phase transition between  $\beta$ -Ti<sub>3</sub>O<sub>5</sub> and  $\lambda$ -Ti<sub>3</sub>O<sub>5</sub> has already been measured by other authors through single-shot time-resolved reflectivity at room temperature [95]. According to the time-resolved optical measurements, the transition from  $\lambda$ -Ti<sub>3</sub>O<sub>5</sub> to  $\beta$ -Ti<sub>3</sub>O<sub>5</sub> needs  $900 \pm 20$  ns to reach the steady state, whereas the transition from  $\beta$ -Ti<sub>3</sub>O<sub>5</sub> to  $\lambda$ -Ti<sub>3</sub>O<sub>5</sub> takes  $20 \pm 5$  ns [95]. Considering the quite large absorption coefficient, the laser penetrates only into very thin layers, resulting in the transformation of surface molecules to the  $\alpha$ -phase. The actual temperature increase is the most important parameter which was in the range from 1000 K to 2000 K. According to the explanation [94], the very high thermal gradient causes a shock wave propagating in the particle with the speed of sound. Therefore, after the thermal effect, the surface layers are in the  $\alpha$ -phase, and then the shock wave turns the  $\alpha$ -phase to the  $\beta$ -phase. Following the thermal diffusion from surface layers to the center of the particle, the seeds of the  $\beta$ -phase grow and propagate towards the center, and at last encounter boundaries [95]. At the picosecond timescale, the intra-cell distortion and propagation happen at the speed of acoustic waves [94]. This process of photo-induced phase transition in surface layers and strained dynamics leading to the transformation of the whole particle can be described by the theory of Thomsen [94, 98].

We define the complex reflection index of Ti<sub>3</sub>O<sub>5</sub>  $\tilde{n}$ , the plane wave as

$$\left. \begin{aligned} E_x &= A e^{i(kx - \omega t)} \\ \tilde{n} &= n(1 + i\kappa) \end{aligned} \right\}$$

Where  $n$  is the refractive index;  $\kappa$  is the extinction coefficient;  $k$  is the wave number; and  $\omega$  is the angular frequency.

$$E_x = A e^{-\omega n \kappa x} e^{i\left(\frac{n}{c}x - \omega t\right)}$$

The absorption coefficient is  $\alpha = \omega n \kappa$ ; and the penetration depth is equal to  $\delta = \frac{1}{\alpha}$ .

In the  $\lambda$ -phase, the metal phase is trapped in the local energy minimum. It needs higher energy to transfer to the  $\beta$ -phase, compared with the transition from  $\beta$ -phase to  $\lambda$ -phase. Furthermore, the material in the  $\lambda$ -phase is metallic with higher reflection.

According to the reported work [99], the refractive index is  $n = 2.3$  at a wavelength of 1064 nm and  $n = 2$  at a wavelength 533 nm. At 1064 nm, the reflection is over 15.5%, and the penetration depth is around 100 nm. At 532 nm, the reflection is 11.1%, and the penetration depth is around 170 nm.

Therefore, as the next step, we will use green laser pulses to do the time-resolved experiment. Due to the lack of time, this couldn't be started yet within this thesis.

## Chapter 6

### Other projects in UTEM

#### Contents

<a href="#">Chapter 6</a> .....	82
<a href="#">Other projects in UTEM</a> .....	82
<a href="#">6.1 Melting processes in core-shell nanoparticles</a> .....	83
<a href="#">6.2 Photothermal reduction of iron oxide nanocrystals</a> .....	84
<a href="#">6.3 Reversible redox reaction in ceria nanoparticles</a> .....	88
<a href="#">6.4 Ultrafast TEM using coherent electron pulses</a> .....	91
<a href="#">PINEM experiment</a> .....	91

At the beginning of this thesis, preliminary experiments on several materials systems have been carried out to find out whether they are suitable for UTEM studies. Some of these systems, where difficulties impeded detailed UTEM studies, are presented in this chapter.

## 6.1 Melting processes in core-shell nanoparticles

The melting process in nanoparticles goes through important non-equilibrium states with complex solid-liquid transition dynamics [100]. The propagation speed of melting is different at low and high energy laser excitation of nanoparticles [100]. In-situ TEM is a versatile technique to study the melting processes. However, an intense laser pulse melts but also evaporates metal nanoparticles. In stroboscopic picosecond imaging in UTEM, millions of laser-excitations are necessary to accumulate enough electron counts in the image. Normally, nanoparticles under laser pulses are totally evaporated after some hundred femtosecond laser pulses. We considered a core-shell nanoparticles method to prevent the evaporation and to measure the melting dynamics [101, 102]. Fig. 6.1 presents Tin nanoparticles covered by layers of carbon, which were fabricated by an arc-discharge method at UTEM group of IPCMS. The mass ratio of Tin/carbon was 1: 1. The current of the arc-discharge was set to 80 A in a helium filled reaction cell at pressure of 200 Torr.

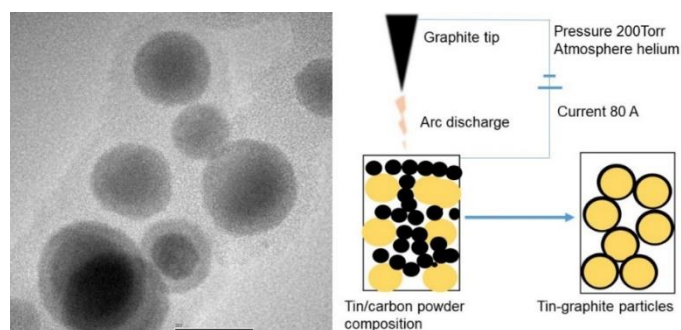


Fig. 6.1 core-shell nanoparticles C@Sn made by arc discharge, the scale bar is 500 nm; right is a schematic description of the arc-discharge method.

In the transformation from solid to liquid, the diffraction peak of Tin nanoparticles should disappear. The repetition frequency of the stroboscopic mode was 100 Hz. But in our experiment, we didn't observe the liquid phase, as shown in fig. 6.2. It seems that melting didn't happen. The experiment was performed in the stroboscopic mode. The carbon shells couldn't totally prevent evaporation of tin. Therefore, the signal was getting weaker and weaker.

Since melting couldn't be observed clearly in these studies, more work on the preparation of suitable core-shell particles is necessary.

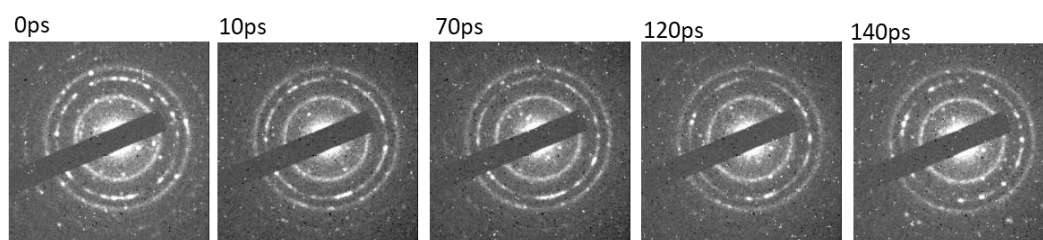


Fig. 6.2 time-resolved diffraction patterns of C@Sn core-shell particles

## 6.2 Photothermal reduction of iron oxide nanocrystals

The carbothermal reaction of  $\text{Fe}_2\text{O}_3$  and Carbon is following previous work on the reduction of NiO nanoparticles [7]. In comparison to NiO, the  $\text{Fe}_2\text{O}_3$  reduction reaction is expected to show more complex dynamics. It is of interest how the different shapes and different sizes of  $\text{Fe}_2\text{O}_3$  nanoparticles at the nanoscale will affect the fast reaction dynamics and atomic diffusion rate. Since the reduction reaction is irreversible, time-resolved studies have to be done in the single-shot mode. This project is in collaborating with Sylvie Begin's group in IPCMS.

The  $\text{Fe}_2\text{O}_3$  nanoparticles were dispersed by  $\text{CCl}_3$  solvent and sonicated 15 min. Fig. 6.3 presents the image of  $\text{Fe}_2\text{O}_3$  nanoparticles on a pure carbon grid.

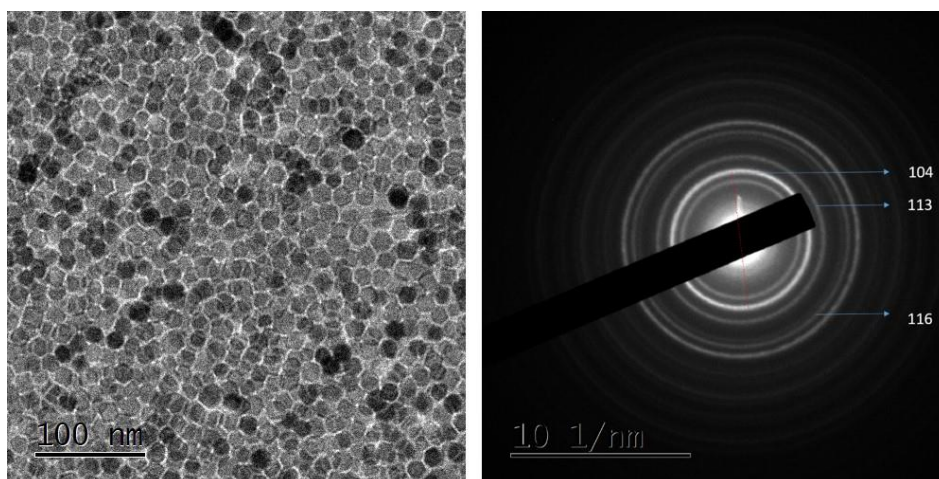


Fig. 6.3  $\text{Fe}_2\text{O}_3$  nanoparticles with 15 nm diameter (left) and the corresponding diffraction pattern (right).

At first, the reduction reaction was observed under a continuous electron beam. Fig. 6.4 (a) shows 15 nm  $\text{Fe}_2\text{O}_3$  nanoparticles before the carbothermal reaction with carbon film after a laser pulse trigger with 100  $\mu\text{J}$  and 1064 nm. Fig. 6.4 (b) shows an image after one laser shot. A larger Fe particle covered by amorphous carbon is visible. The fig. 6.4 (c) and (d) show the corresponding diffraction patterns before and after the reduction reaction, respectively. According to the corresponding EELS, we see that the reaction is finished after one laser shot. Only the Fe particles are left on the carbon grid, as shown in fig. 6.4 (e) and (f). Fig. 6.4 (e) shows an EELS of  $\text{Fe}_2\text{O}_3$ , and fig. 6.4 (f) the same after a laser shot.

In the fig. 6.5 (a) and (c), 5 nm nanoparticles were dispersed on a pure carbon grid. After a laser shot with 95  $\mu\text{J}$ , the resulting Fe crystals are shown in fig. 6.5 (b). In diffraction, the Fe nanoparticle is difficult to localize in fig. 6.5 (d). According to (e) and (f), the full reduction happened under a laser shot, and iron particles are left on the grid.

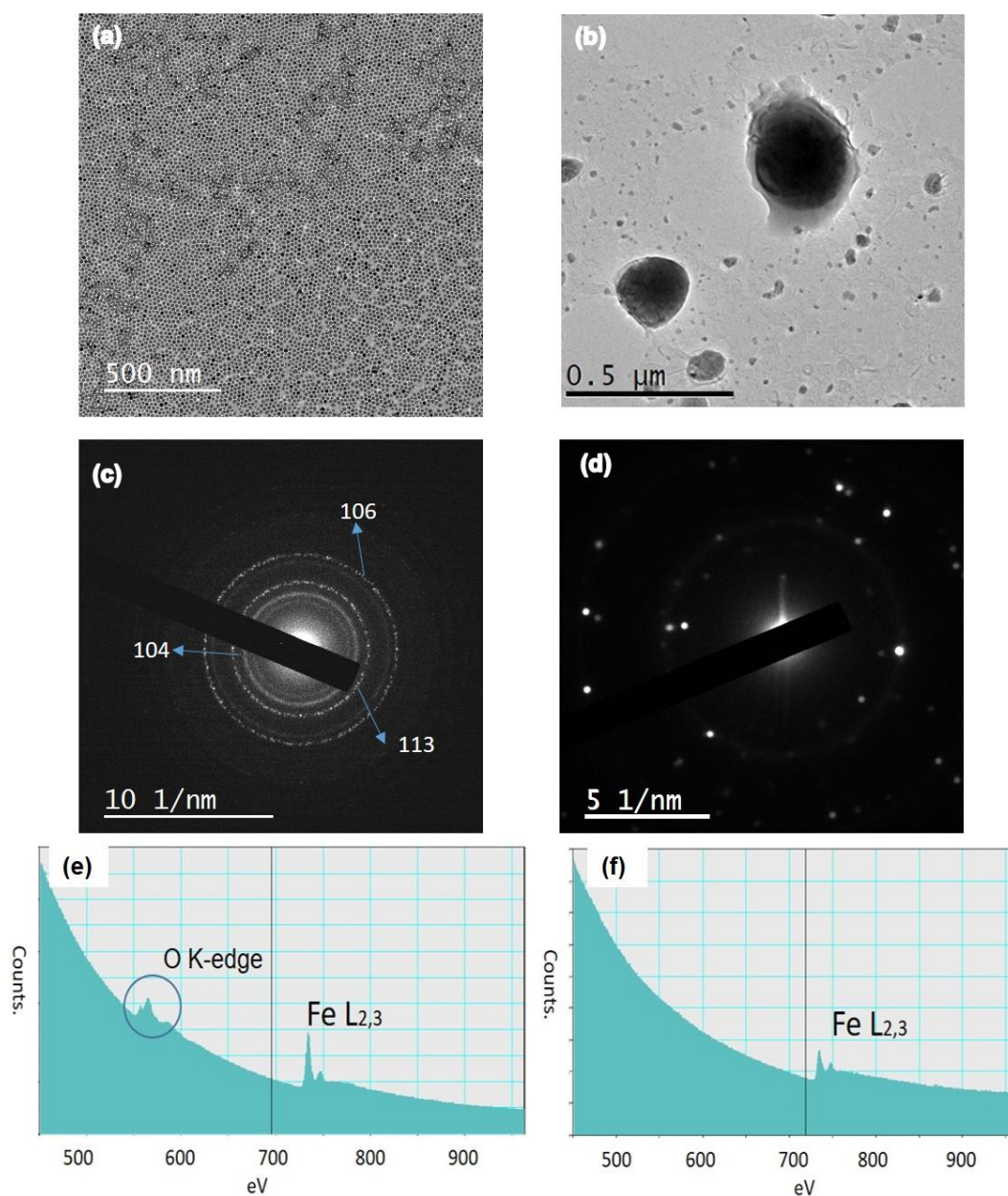


Fig. 6.4 image, diffraction pattern and EELS of Fe<sub>2</sub>O<sub>3</sub> nanoparticles before and after the reaction with the carbon film: (a) image of Fe<sub>2</sub>O<sub>3</sub> nanocrystals; (b) pure Fe crystals after carbothermal reaction; (c) diffraction pattern of Fe<sub>2</sub>O<sub>3</sub> before the reaction; (d) diffraction pattern after the reaction; (e) Fe<sub>2</sub>O<sub>3</sub> nanoparticles EELS before carbothermal reaction; (f) EELS after carbothermal reaction.

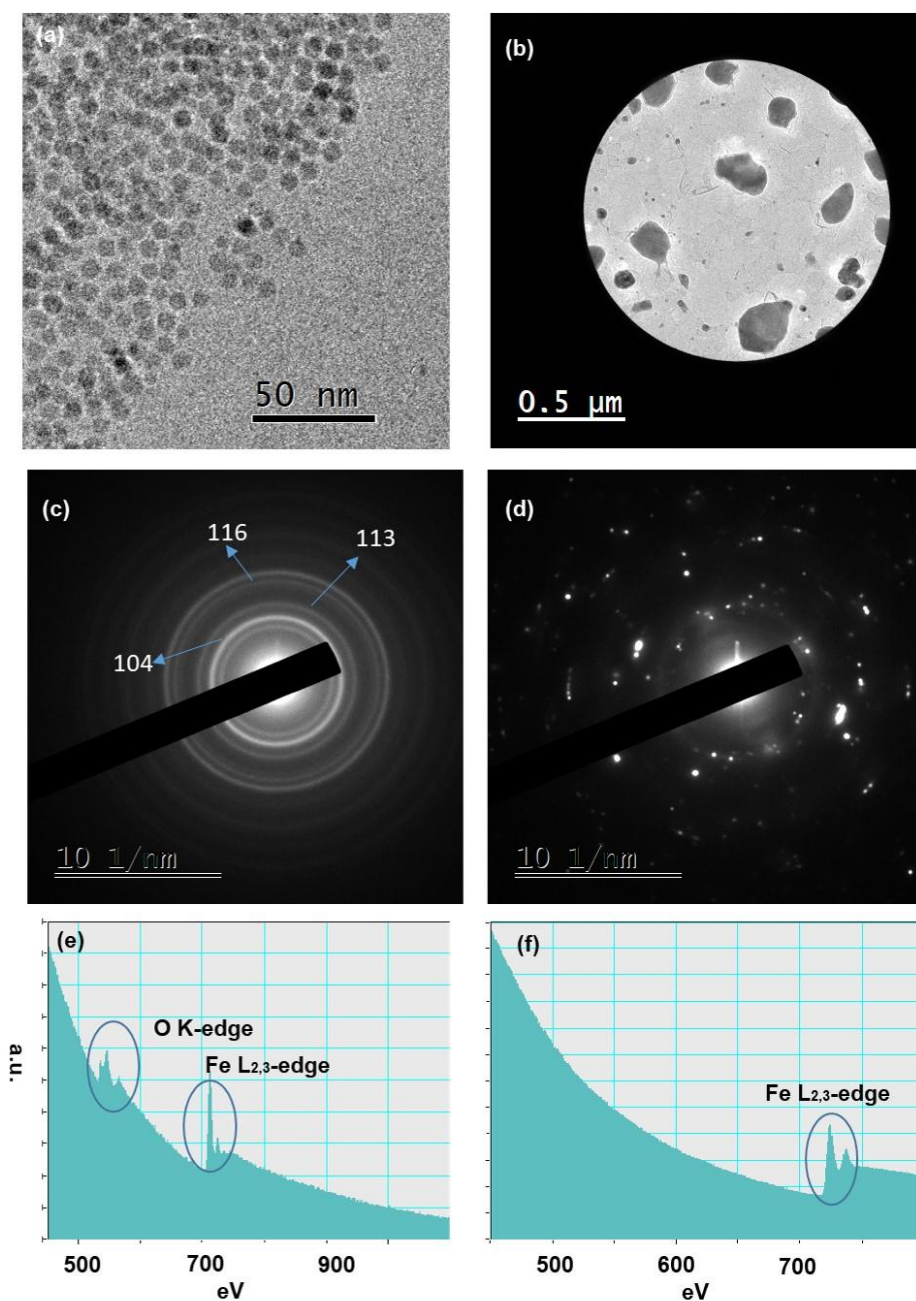


Fig. 6.5 (a) 5 nm ~ 7 nm Fe<sub>2</sub>O<sub>3</sub> nanoparticles before the reaction; (b) image of iron after the laser-induced reaction; (c) diffraction pattern of Fe<sub>2</sub>O<sub>3</sub>; (d) diffraction pattern after a laser shot; (e) and (f) are the EELS before and after reduction.

Fig. 6.6 shows an EELS from Fe<sub>2</sub>O<sub>3</sub> nanoparticles taken with a single-shot electron pulse of 7 ns duration.

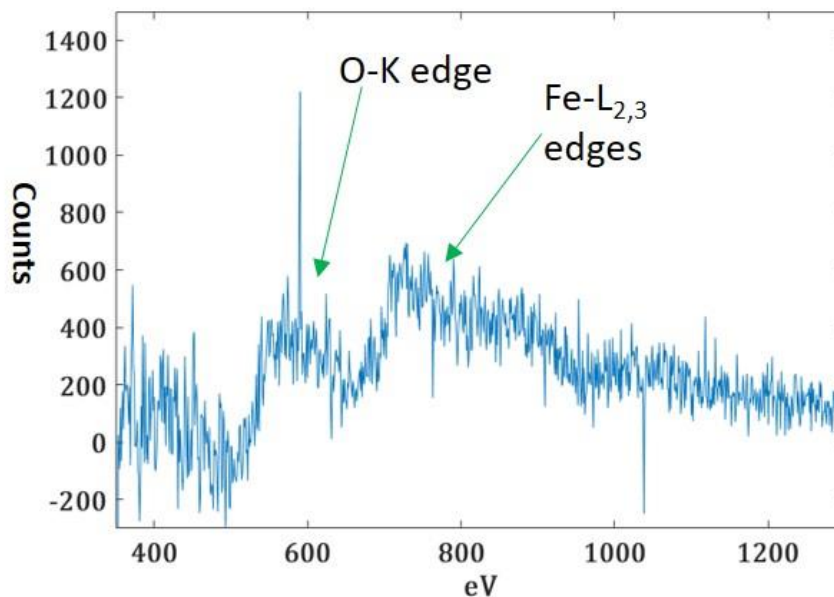


Fig. 6.6 Single-shot nanosecond EELS

The time-resolved measurements in single-shot will need a more careful specimen preparation to allow sufficient signal in the images, diffraction patterns and EELS. This will be time-consuming and finished by my colleagues. The intensity and energy width of the photoelectron pulses still have to be improved. After further instrumental improvements and an optimized Fe<sub>2</sub>O<sub>3</sub> nanoparticle synthesis, reduction reaction in particles with different shapes (hexahedron, sphere and polyhedron) will be measured.

### 6.3 Reversible redox reaction in ceria nanoparticles

Solid oxide fuel cells can provide high energy conversion efficiency at relatively low temperatures (500 °C – 700 °C) [103]. The doped CeO<sub>2</sub> acts as electrolyte in solid oxide fuel cells. The Ce ions are reduced from Ce<sup>4+</sup> to Ce<sup>3+</sup>. The ceria reduction is a reversible process between CeO<sub>2</sub> and Ce<sub>2</sub>O<sub>3</sub>. The stable phase is normally determined by the environment of the ceria particles. Here, we present the reduction of ceria nanoparticles in an in-situ TEM experiment. Fig. 6.7 presents CeO<sub>2</sub> nanoparticles and the corresponding diffraction pattern.

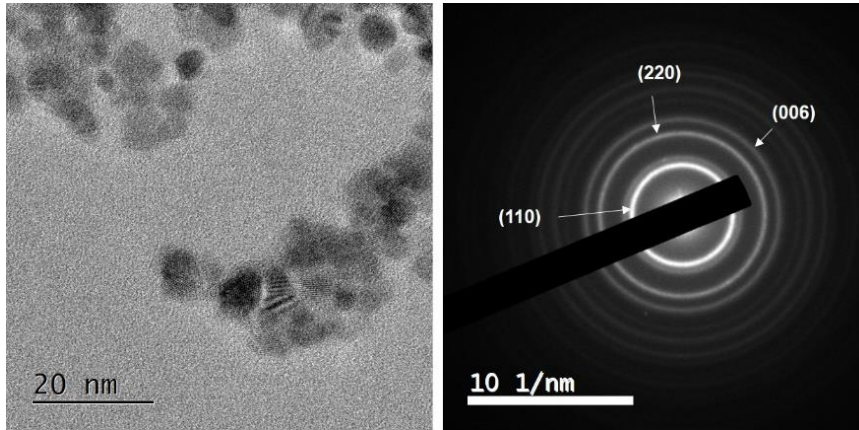


Fig. 6.7 Left: image of CeO<sub>2</sub> particles at room temperature; right: diffraction pattern of CeO<sub>2</sub>.

Fig. 6.8 shows the diffraction peak shift as a function of temperature in thermal equilibrium. The diffraction patterns were taken with a continuous electron beam. The diffraction peak (1 1 1) of CeO<sub>2</sub> changes to Ce<sub>2</sub>O<sub>3</sub> (1 0 0) at 700 °C.

The EELS at two temperatures are shown in fig. 6.9. When the particles are in the CeO<sub>2</sub> state, the M<sub>4</sub> peak is higher than the M<sub>5</sub> peak. The peak of M<sub>5</sub> is higher than M<sub>4</sub> in the Ce<sub>2</sub>O<sub>3</sub> state at a temperature of 700 °C.

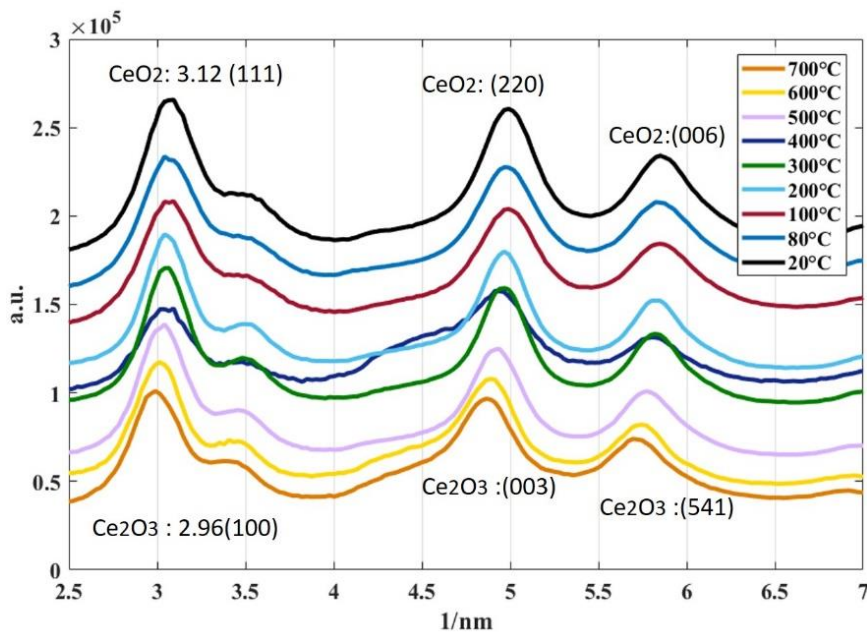


Fig. 6.8 Thermal transition from CeO<sub>2</sub> to Ce<sub>2</sub>O<sub>3</sub>. Diffraction peak shift at different temperatures.

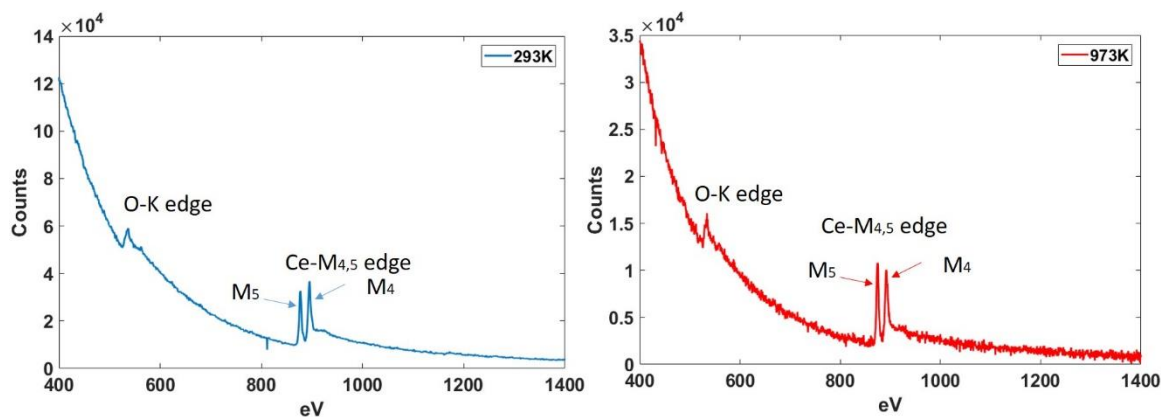


Fig. 6.9 EELS of CeO<sub>2</sub> at 293 K and Ce<sub>2</sub>O<sub>3</sub> at 973 K.

Fig. 6.10 presents the ratio of the M<sub>4</sub>/M<sub>5</sub> edges in EELS as a function of temperature. The redox reaction shows a hysteresis between CeO<sub>2</sub> and Ce<sub>2</sub>O<sub>3</sub>.

In a laser-triggered experiment, this reduction reaction needs an intense laser pulse. Therefore, it takes a long time after a laser shot for cooling back to room temperature. This process normally needs several minutes, making a stroboscopic experiment almost impossible. In future experiments, the redox reaction should be triggered by other methods.

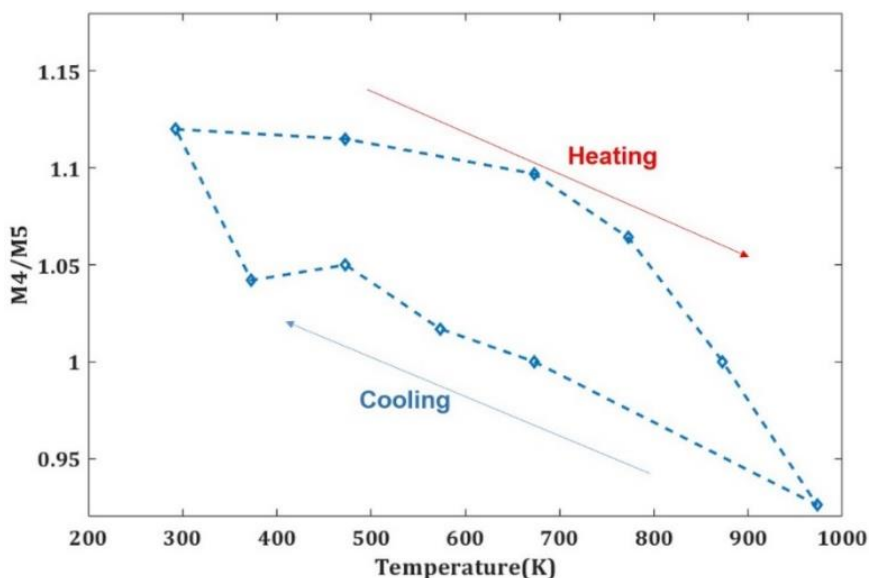


Fig. 6.10. M<sub>4</sub>/M<sub>5</sub> ratio in the EELS of ceria as a function of temperature. A hysteresis appears upon heating and cooling.

## 6.4 Ultrafast TEM using coherent electron pulses

PINEM (see chapter 2) provides a new way to observe transient dynamics of electrons and their coherent coupling to photon fields. Currently, the most reported works are done with field-emission guns with an emission area of less than 10 nm [28, 39 - 46, 104, 105]. Here, we show the PINEM phenomenon based on a thermal gun in photoelectron mode which has a larger emission area and less spatial coherence. Experiments with the PINEM effect were envisaged but not pursued due to other interesting applications of UTEM in materials research that we pursued.

### PINEM experiment

A gold film with 20 nm thickness was deposited on a holey carbon membrane grid. The pump laser with 1.2 eV generated an optical near-field around the gold film by plasmon excitation. Fig. 6.11 shows the result of photon-induced near field microscopy (PINEM) in the UTEM with a thermal gun. In the experiment, the condenser aperture with diameter 20  $\mu\text{m}$  and tip-shaped filament with diameter 20  $\mu\text{m}$  were employed in order to keep the paraxial property of the free electron beam and improve the transverse coherence of source.

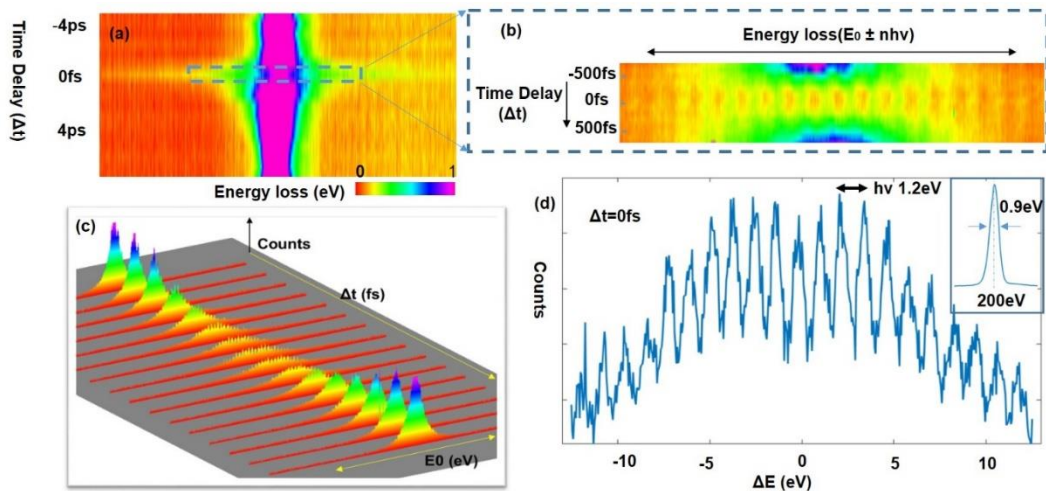


Fig. 6.11 Temporal pulse profile of the EELS around the zero-loss peak: at time-zero the electrons beam interacts with the light field: (a) Electron energy-loss spectra as a function of pump-probe delay; (b)

selected area of (a); (c) three dimensional profile of (b); (d) EEL spectrum at time-zero, and the inserted curve is the initial profile of the zero-loss peak without interaction.

Fig. 6.12 presents the PINEM spectrum when a disc cathode is used. The disc has a diameter of 1 mm. The disc can provide more electrons in the pulse, but the spatial coherence is much lower than of a tip-like filament. The PINEM result from a tip filament can clearly distinguish the sidebands up to  $\pm 11 \hbar\omega$ . But using the disc filament, the negative sideband just shows the  $-\hbar\omega$  peak clearly, and in the positive sideband up to  $1 \sim 5 \hbar\omega$ .

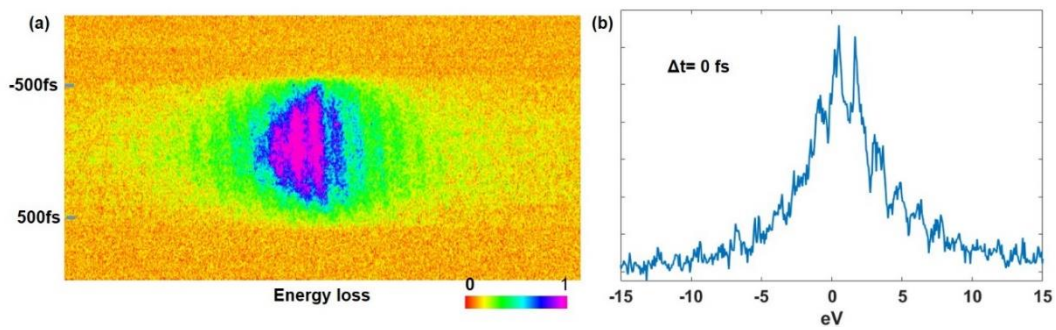


Fig. 6.12. (a) is Electron energy-loss spectra as a function of pump-probe delay; (b) PINEM at time-zero.

## Chapter 7

### Conclusion of this thesis

This chapter summarizes the results of chapters 4 and 5, and discusses their importance in UTEM of nanomaterials. Photo-switching effects, realized by volume changes in nanomaterials under laser pulses are the center of my thesis.

The ultrafast transmission electron microscope (UTEM) at the IPCMS was installed in 2014. Through the following years, the stroboscopic mode was developed. Since 2018, nanosecond electron pulses can be used in both stroboscopic and single-shot for imaging and analytical TEM, resulting from the efforts of my colleagues (Matthieu Picher, Florian Banhart, Kerstin Bückler, Shyam Sinha, and Thomas LaGrange). Based on these achievements, my thesis started from the research of laser-induced phase transitions in nanomaterials. The collaboration with the groups of Guillaume Chastanet (Bordeaux) and Maciej Lorenc (Rennes) were indispensable for the success of this work.

Before time-resolved measurements could be done, the hysteresis curve of the volume change of SCO nanoparticles was observed. In microscopic observations, the expansion ratio of the b-axis of the SCO crystals was the measured parameter, and a maximum elongation of 5.1% was observed. The hysteresis width was around 40 K. In time-resolved experiments, a detailed quantitative study of the response of SCO crystals to laser-induced heat pulses was undertaken. Pure SCO particles require 120 ns to reach their maximum expansion. In order to decrease the switching time and to increase the heating efficiency as well as to expand the absorption spectrum, gold nanoparticles were encapsulated in the SCO particles. The SCO@AuNps reach their maximum expansion already within 20 ns. After 500 ns delay, the SCO particles and their environment reach thermal equilibrium where the expansion of the particles remains in saturation. This state remains 50  $\mu$ s, and then the particles cool and shrink

into their initial size. The relaxation process normally takes 200  $\mu\text{s}$  ~ 500  $\mu\text{s}$  and depends on the thermal diffusion towards the substrate. Graphene substrates were employed in the time-resolved measurements due to the good thermal conductivity and high optical transparency.

Once the laser energy of pulses with 1064 nm wavelength and 150  $\mu\text{m}$  diameter is over 20  $\mu\text{J}$ , there is an obvious oscillation of the length around 5% elongation until they reach the thermal equilibrium where the SCO particle can temporarily reach an elongation of around 6.3%. In the excitation goes beyond the saturation elongation, a transient compression can be observed due to cluster growth of molecules in the high-spin state, causing a successive oscillation of the length. This needs to be further demonstrated by excitation with a green laser, where the SCO particles have a strong absorption around 532 nm. The overshooting expansion is associated with compression and could create seeds for more high-spin molecules in the SCO particle within picoseconds. Heating with green laser pulses would not need heating from the substrate as with 1064 nm laser pulses. If the oscillation still exists after excitation with green light, it should be the competition between LS and HS in the elastic step. If not, it could be related to an unstable thermal transition between SCO and the substrate.

Nanoparticles of  $\text{Ti}_3\text{O}_5$  are a transition metal oxide which shows a reversible phase transition at room temperature under laser pulses. We studied  $\text{Ti}_3\text{O}_5$  particles where the sensitive (2 0 1) reflections appear in the TEM and analyzed the volume expansion as a function of temperature. The particle in the  $\beta$ -phase is the stable ground state at room temperature. After heating to 600 K and cooling back to room temperature, the particle was trapped in the metastable  $\lambda$ -phase where an external excitation is needed to switch the particle back to the more stable  $\beta$ -phase. The particles showed the expected phase transition under infrared (1.2 eV and 7 ns) and green laser pulses (2.33 eV and 7 ns). According to optical measurements, the transition from the  $\beta$ -phase to the  $\lambda$ -phase need 20 ns, but the transition from the  $\lambda$ -phase to the  $\beta$ -phase takes 900 ns. This result will have to be demonstrated and studied in detail by time-resolved measurements in the UTEM.

After the study of these volume changes in photoswitchable materials, i.e., the particle shape and the projected area, the results give useful information for determining crystalline rearrangements and orientation effects. The timescales of switching are highly important in applications as photoswitches or in optoelectronic devices. The volume changes will furthermore cause internal strains in devices and influence their lifetime.

From the instrumental viewpoint, the study of coherent coupling of electron and light fields in nano-optics can be studied by our thermal gun setup in the UTEM. When we employ a tip-like filament and a small condenser aperture, the coherence of the electron beam can be improved. In the future, if the photon-electron interaction is further developed and employed to quantum bit manipulation and computing, electron pulses from a thermal gun-based electron microscope could be a good choice due to its high stability and moderate costs.

### Pending work

At first, the length oscillations of SCO particles will be studied in detail in more experiments using a 532 nm laser. The vibration around the 5% elongation ratio needs further measurements. Green laser excitation produces more excited molecules before the elastic interaction with neighbouring molecules.

Furthermore, time-resolved experiments on  $\text{Ti}_3\text{O}_5$  nanoparticles in the single-shot mode will be done. After further improvement of the photoemission intensity, the single-shot mode should be improved to acquire images with higher spatial resolution. It is important to calculate the projected surface area from time-resolved imaging and to conclude on volume changes during the reversible phase transition between the two phases at room temperature.

While experiments on the length oscillations in SCO particles should be feasible within a short time, measurements on  $\text{Ti}_3\text{O}_5$  will be a more extended project.

## Résumé de thèse en français

Mes projets de recherche s'appuient sur les applications de la microscopie électronique ultrarapide (UTEM) pour étudier des transitions de phase dans des différents nanomatériaux.

Le manuscrit anglais est constituée de six chapitres, incluant une introduction, deux chapitres sur les techniques pompe-sonde, la microscopie électronique ultrarapide et les transitions de phase photo-induites dans certains nouveaux nanomatériaux, ainsi que deux chapitres présentant la dynamique des matériaux du type spin crossover (SCO) et les transitions de phase photo-induites dans un oxyde de titane ( $Ti_3O_5$ ) et un dernier chapitre avec des conclusions.

Ce résumé contient une introduction aux projets de recherche que j'ai pu réaliser dans le cadre de ma thèse, la description de deux projets sur les transitions de phase dans des nanomatériaux qui ont été étudiées par UTEM et une conclusion.

### Introduction

Les microscopes électroniques conventionnels utilisent des faisceaux d'électrons continus pour détecter la morphologie de l'échantillon et ses structures cristallines. Ces électrons en microscopie conventionnelle sont générés par émission thermique à partir d'un filament ou par émission dans un champ électrique. Normalement, ces électrons ont une distribution temporelle aléatoire dans un faisceau d'électrons continu. TEM fournit une résolution spatiale jusqu'à l'échelle de l'atome. Cependant, la rupture ou création de liaisons chimiques; le transfert d'énergie entre les électrons et le réseau cristallin, les transformations magnétiques ou les fluctuations qui favorisent les transitions de phase se produisent sur des échelles de temps ultrarapides, allant de la micro- à la femtoseconde. Aujourd'hui, les lasers pulsés avec des impulsions

ultrabrèves nous donnent la possibilité d'obtenir des impulsions de la nano- à la femtoseconde, voire l'attoseconde, la microscopie électronique résolue en temps (UTEM) combine la résolution spatiale à l'échelle de l'atome avec la résolution temporelle à l'échelle de la picoseconde. Des impulsions ultrabrèves d'électrons sont créés par effet photoélectrique dans la colonne d'un microscope électronique. L'imagerie, la diffraction électronique et la spectroscopie de perte d'énergie des électrons peut ainsi être réalisée par des impulsions d'électrons et permet des études résolues en temps avec une résolution jusqu'à la picoseconde. Cela nous donne la possibilité d'étudier le mouvement collectif des électrons, la vibration du réseau et les transitions de phase rapides bien que les impulsions électroniques subissent un étalement spatial et temporel pendant la propagation dans la colonne du microscope. Dans le cadre de ma thèse, j'ai utilisé le microscope électronique ultrarapide à l'IPCMS pour étudier le comportement temporel de différentes nanoparticules pendant des transformations de phase induites par des impulsions laser. L'intérêt au niveau des applications de ces nanoparticules est le « nano-switching » des particules qui changent leur taille sous éclairage avec la lumière ou sous impulsions thermiques.

### **Dynamique des transformations dans des nanoparticules du type spin-crossover (SCO)**

Les molécules du type spin-crossover changent la longueur des liaisons chimiques entre un atome métallique central et les ligands sous irradiation lumineuse et à température élevée. Ces molécules constituent de nanocristaux qui gonflent sous ces excitations mentionnées dessus. Comme ce processus (gonflement-dégonflement) est réversible, l'échelle temporelle des transformations morphologiques est d'intérêt dans l'optique des applications comme « nano-interrupteurs ». Dans nos expériences, nous mesurons la taille d'une nanoparticule SCO cristalline rectangulaire en fonction de la température et du temps. La longueur nous donne des informations sur l'interaction entre les molécules dans les états low-spin (LS, à basse température) et

high spin (HS, à haute température ou sous lumière) dans les nanoparticules. En mesurant l'échelle temporelle des transitions, on peut donc suivre la concurrence entre les états LS et HS. De plus, nous pouvons suivre l'évolution du cristal après une excitation externe, p. ex. une impulsion laser. Nous avons d'abord étudié la longueur d'une particule SCO individuelle en fonction de la température dans un TEM conventionnel en utilisant un porte-objet chauffant, comme le montre la Fig. 1.

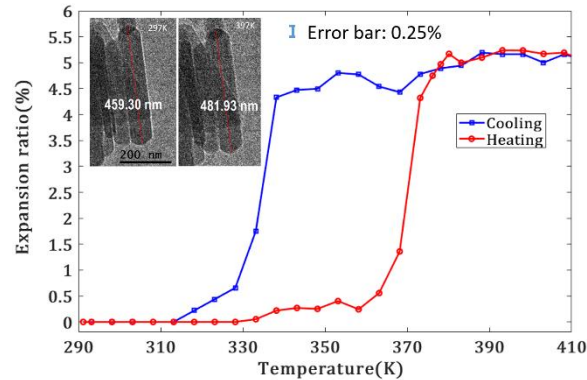


Fig.1 Longueur d'une particule SCO en fonction de la température.

Nous avons ensuite réalisé une étude résolue en temps de l'expansion et contraction des nanoparticules SCO dans un TEM ultrarapide. Des impulsions laser d'une durée de 7 ns et d'une longueur d'onde de 1064 nm ont été utilisées. Les particules SCO ayant une faible absorption dans l'IR, la principale source de chauffage par les impulsions laser est le transfert de chaleur du substrat absorbant (ici un film de carbone) vers les particules. L'expansion d'une particule SCO en fonction du temps est représentée dans la fig. 2. L'allongement des nanoparticules variait avec l'énergie d'impulsion laser appliquée. En comparaison avec des travaux antérieurs sur les particules SCO, on peut conclure que l'excitation des particules comprend quatre étapes. La première étape est la photo-commutation qui est le croisement ultrarapide entre les systèmes, c'est-à-dire une transformation électronique non thermique (sur une échelle fs à ps). Au cours de cette étape, qui n'est pas visible dans nos expériences, la nanoparticule est toujours à volume constant.

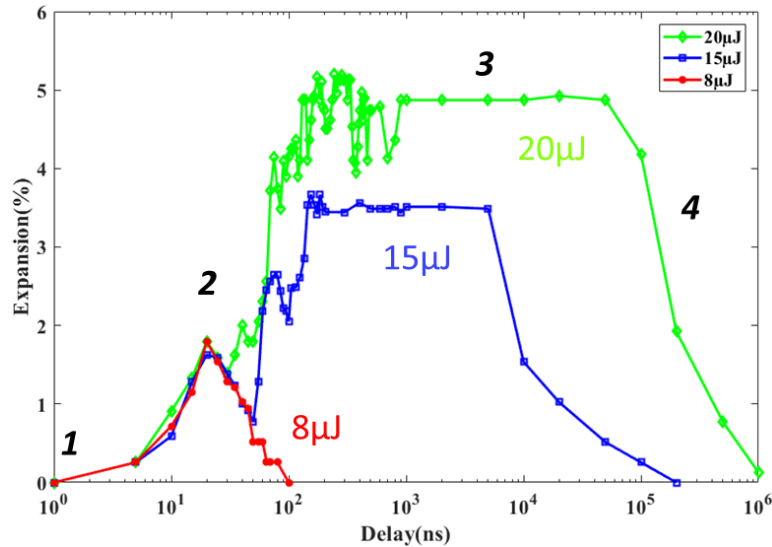


Fig. 2 Expansion d'une nanoparticule SCO pure sous impulsions laser IR en fonction du temps.

La deuxième étape de la transition est l'étape élastique. Le chauffage du réseau entraîne l'expansion du volume (> 1 ns) durant la transition low spin à high spin et établit un équilibre mécanique avec l'environnement. C'est l'expansion visible dans nos expériences (pente de gauche) sur la figure 2. La troisième étape est l'équilibre thermique qui est établi entre la nanoparticule et son environnement (plateau sur la figure 2). La longueur des particules est à saturation et ne change pas de longueur pendant qu'elle refroidit lentement. Au cours de la quatrième étape, la particule se refroidit en dessous du seuil d'expansion maximale et se détend à sa longueur initiale. Le processus est donc réversible.

En collaboration avec l'équipe de Guillaume Chastanet à Bordeaux, des nanobâtonnets d'or ont été encapsulés dans les particules SCO, ce qui induit le chauffage plasmonique de l'or qui transfère efficacement la chaleur à la particule SCO environnante. La particule atteint son allongement maximal en 20 ns environ, comme le montre la fig. 3.

En plus de l'expansion, les nanoparticules SCO montrent aussi une oscillation de leur taille autour la valeur en équilibre après l'excitation avec une impulsion laser. Cet effet n'était pas observé auparavant et montre l'échelle temporelle des interactions collectives, les effets de surface et la réponse élastique des nanoparticules aux

transformations de spin.

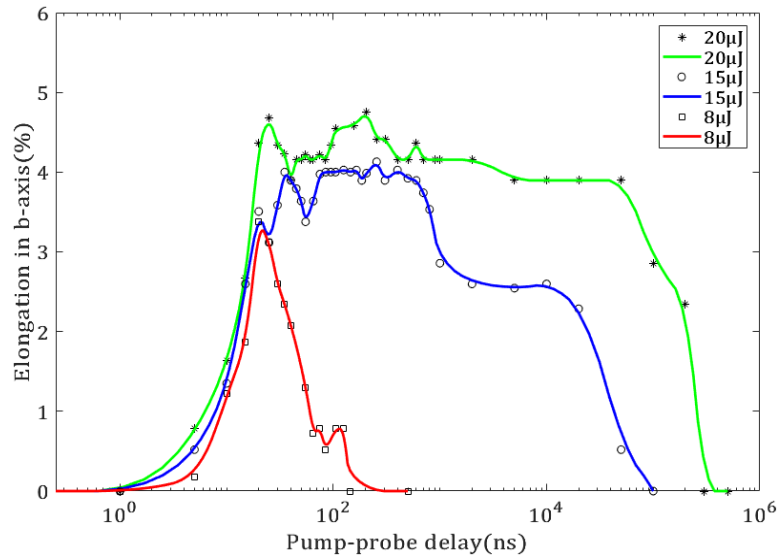


Fig.3 Mesure résolue en temps de l'expansion d'une particule SCO avec 3 nanobâtonnets Au encapsulés, à différentes énergies d'impulsion laser IR.

Le progrès de nos expériences par rapport aux connaissances jusqu'à présent est que nous avons présenté les premières mesures sur des nanoparticules uniques de SCO. Le comportement morphologique à l'échelle de la nanoseconde a été révélé et dynamique collective dans ces nanoparticules montre des effets intéressants.

### Transitions de phase dans $Ti_3O_5$ sous impulsions laser étudiées par microscopie électronique

Cette étude est menée en collaboration avec le groupe de Maciej Lorenc à l'Université de Rennes. Les spécimens livrés par le groupe rennais ont été synthétisés par broyage à billes par le groupe de S. Ohkoshi à l'Université de Tokyo.

Le  $Ti_3O_5$  est le premier oxyde métallique qui a une bistabilité entre deux phases à température ambiante. Sous excitation thermique,  $Ti_3O_5$  montre une transition de phase de  $\beta-Ti_3O_5$ , qui est énergétiquement favorable, à la phase métastable  $\lambda-Ti_3O_5$ . Les paramètres de maille de ces deux phases étant différents, la particule change sa taille pendant la transition. Ce changement de taille a été mesuré en fonction de la

température et sous impulsions laser dans le microscope électronique ultrarapide. La figure 4 montre la taille des nanoparticules avant chauffage et après refroidissement. Les expériences ont été menées avec un porte-objet chauffant en équilibre thermique.

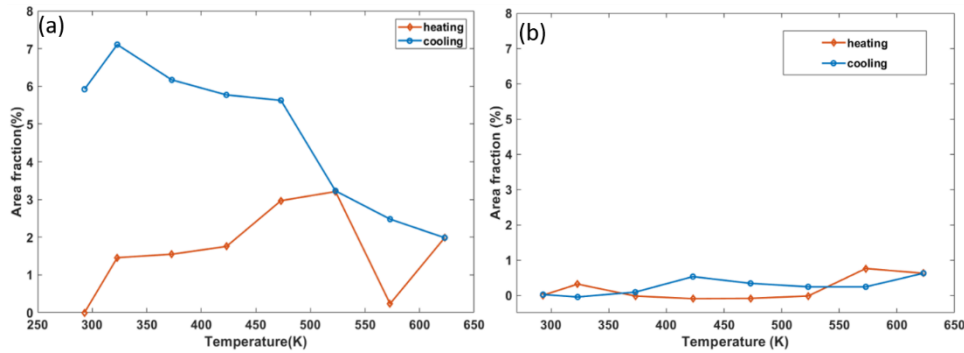


Fig. 4 (a) la surface projetée dans le plan de l'image varie avec la température dans le premier cycle de chauffage ; (b) la surface ne change plus avec la température dans le deuxième cycle de chauffage.

Dans un premier cycle de chauffage, la surface projetée dans le plan image du microscope montre un changement évident. C'est donc la transition entre la phase beta (stable à température ambiante) et la phase lambda (métastable). Après le premier cycle de chauffage, la particule reste piégée dans la phase lambda métastable. Au cours d'un deuxième cycle de chauffage, la particule subit d'abord une transition entre la phase lambda et la phase alpha qui n'est stable qu'à haute température. Néanmoins, la fraction de surface ne montre pas un changement important à cause des paramètres de maille comparable. Après chauffage, la particule revient à la phase lambda où elle reste piégée. Après une impulsion laser avec une puissance  $2.8 \text{ mJ/cm}^2$ , la particule est revenue à l'état d'énergie minimale de la phase beta. On a donc pu montrer que ce processus est réversible. Après une impulsion laser plus faible ( $2.4 \text{ mJ/cm}^2$ ) avec la même longueur d'onde et la même durée, la particule est re-transférée à la phase lambda, comme le montre la fig. 5.

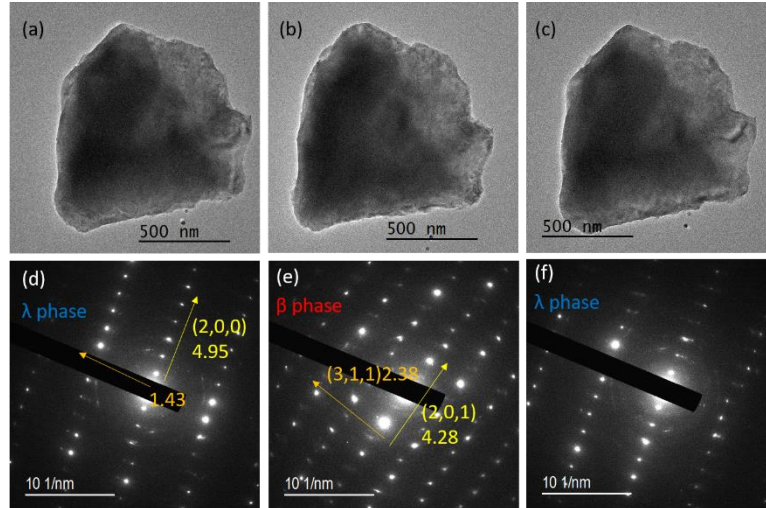


Fig. 5 (a) Transformations en phase dans le  $\text{Ti}_3\text{O}_5$ ; (b) après tir laser avec  $2.8 \text{ mJ/cm}^2$ ,  $1064 \text{ nm}$  et  $7 \text{ ns}$ ; (c) après tir laser avec  $2.4 \text{ mJ/cm}^2$ ,  $1064 \text{ nm}$  et  $7 \text{ ns}$ ; (d)-(f) sont respectivement le diagramme de diffraction de (a)-(c).

Les mesures de la vitesse de transition, ce qui est le but principal de cette étude, sont encore en cours.

## Conclusion

Nous avons étudié la dynamique des nanoparticules uniques de SCO de l'échelle de la nanoseconde à la milliseconde. Les nanoparticules SCO pures nécessitent jusqu'à  $100 \text{ ns}$  pour atteindre leur allongement maximal. Une fois que nous y avons encapsulé des nanoparticules plasmoniques d'or, le temps passera à  $20 \text{ ns}$ . C'est donc une méthode prometteuse pour améliorer le dispositif de commutation photo-induite. Ensuite, nous avons démontré une transition de phase thermo/photo-induite du  $\text{Ti}_3\text{O}_5$  par microscopie électronique. Nous avons également démontré une transition de phase de l'état piégé à l'état d'énergie minimale par déclenchement laser en TEM, ce qui montre que la transformation entre les deux phases à température ambiante est réversible.

**Mots clés : matériaux spin-crossover,  $\text{Ti}_3\text{O}_5$ , transitions de phase, microscopie électronique ultrarapide;**

## References

- [1] Nisoli, M., & Sansone, G. (2009). New frontiers in attosecond science. *Progress in Quantum Electronics*, 33, 17-59.
- [2] Brändén, G., & Neutze, R. (2021). Advances and challenges in time-resolved macromolecular crystallography. *Science*, 373, eaba0954.
- [3] Lloyd-Hughes, J., Oppeneer, P. M., Dos Santos, T. P., Schleife, A., Meng, S., Sentef, M. A., & Hegmann, F. (2021). The 2021 ultrafast spectroscopic probes of condensed matter roadmap. *Journal of Physics: Condensed Matter*, 33, 353001.
- [4] Chen, Z., Luo, J. W., & Wang, L. W. (2019). Revealing angular momentum transfer channels and timescales in the ultrafast demagnetization process of ferromagnetic semiconductors. *Proceedings of the National Academy of Sciences*, 116, 19258-19263.
- [5] Bigot, J. Y., Vomir, M., & Beaurepaire, E. (2009). Coherent ultrafast magnetism induced by femtosecond laser pulses. *Nature Physics*, 5, 515-520.
- [6] De la Torre, A., Kennes, D. M., Claassen, M., Gerber, S., McIver, J. W., & Sentef, M. A. (2021). Nonthermal pathways to ultrafast control in quantum materials. *arXiv preprint arXiv:2103.14888*.
- [7] Sinha, S. K., Khammari, A., Picher, M., Roulland, F., Viart, N., LaGrange, T., & Banhart, F. (2019). Nanosecond electron pulses in the analytical electron microscopy of a fast irreversible chemical reaction. *Nature Communications*, 10, 1-8.
- [8] Zewail, A. H. (1988). Laser femtochemistry. *Science*, 242, 1645-1653.
- [9] Haider, M., Rose, H., Uhlemann, S., Schwan, E., Kabius, B., & Urban, K. (1998). A spherical-aberration-corrected 200 kV transmission electron microscope. *Ultramicroscopy*, 75, 53-60.

- [10] Arbouet, A., Caruso, G. M., & Houdellier, F. (2018). Ultrafast transmission electron microscopy: historical development, instrumentation, and applications. *Advances in imaging and electron physics*, 207, 1-72.
- [11] Barwick, B., Park, H. S., Kwon, O. H., Baskin, J. S., & Zewail, A. H. (2008). 4D imaging of transient structures and morphologies in ultrafast electron microscopy. *Science*, 322, 1227-1231.
- [12] Beaurepaire, E., Merle, J. C., Daunois, A., & Bigot, J. Y. (1996). Ultrafast spin dynamics in ferromagnetic nickel. *Physical Review Letters*, 76, 4250.
- [13] Maehrlein, S. F., Radu, I., Maldonado, P., Paarmann, A., Gensch, M., Kalashnikova, A. M., & Kampfrath, T. (2018). Dissecting spin-phonon equilibration in ferrimagnetic insulators by ultrafast lattice excitation. *Science Advances*, 4, eaar5164.
- [14] Kubacka, T., Johnson, J. A., Hoffmann, M. C., Vicario, C., De Jong, S., Beaud, P., & Staub, U. (2014). Large-amplitude spin dynamics driven by a THz pulse in resonance with an electromagnon. *Science*, 343, 1333-1336.
- [15] Schlauderer, S., Lange, C., Baierl, S., Ebnet, T., Schmid, C. P., Valovcin, D. C., & Huber, R. (2019). Temporal and spectral fingerprints of ultrafast all-coherent spin switching. *Nature*, 569, 383-387.
- [16] Först, M., Manzoni, C., Kaiser, S., Tomioka, Y., Tokura, Y. N., Merlin, R., & Cavalleri, A. (2011). Nonlinear phononics as an ultrafast route to lattice control. *Nature Physics*, 7, 854-856.
- [17] Fausti, D., Tobey, R. I., Dean, N., Kaiser, S., Dienst, A., Hoffmann, M. C., & Cavalleri, A. (2011). Light-induced superconductivity in a stripe-ordered cuprate. *Science*, 331, 189-191.
- [18] Buzzi, M., Först, M., Mankowsky, R., & Cavalleri, A. (2018). Probing dynamics in quantum materials with femtosecond X-rays. *Nature Reviews Materials*, 3, 299-311.

- [19] Murnane, M. M., Kapteyn, H. C., Rosen, M. D., & Falcone, R. W. (1991). Ultrafast x-ray pulses from laser-produced plasmas. *Science*, 251, 531-536.
- [20] Rischel, C., Rousse, A., Uschmann, I., Albouy, P. A., Geindre, J. P., Audebert, P., & Antonetti, A. (1997). Femtosecond time-resolved X-ray diffraction from laser-heated organic films. *Nature*, 390, 490-492.
- [21] Balerna A., & Mobilio S, (2015). Introduction to synchrotron radiation. In *Synchrotron radiation*. Springer, Berlin, Heidelberg, 3-28.
- [22] Hennecke, M., Radu, I., Abrudan, R., Kachel, T., Holldack, K., Mitzner, R., & Eisebitt, S. (2019). Angular momentum flow during ultrafast demagnetization of a ferrimagnet. *Physical Review Letters*, 122, 157202.
- [23] Pellegrini, C., Marinelli, A., & Reiche, S. (2016). The physics of x-ray free-electron lasers. *Reviews of Modern Physics*, 88, 015006.
- [24] Radu, I., Vahaplar, K., Stamm, C., Kachel, T., Pontius, N., Dürr, H. A., & Kimel, A. V. (2011). Transient ferromagnetic-like state mediating ultrafast reversal of antiferromagnetically coupled spins. *Nature*, 472, 205-208.
- [25] Beaud, P., Caviezel, A., Mariager, S. O., Rettig, L., Ingold, G., Dornes, C., Staub, U. (2014). A time-dependent order parameter for ultrafast photoinduced phase transitions. *Nature Materials*, 13, 923-927.
- [26] Urban, K., Kabius, B., Haider, M., & Rose, H. (1999). A way to higher resolution: spherical-aberration correction in a 200 kV transmission electron microscope. *Microscopy*, 48, 821-826.
- [27] Lahme, S., Kealhofer, C., Krausz, F., & Baum, P. (2014). Femtosecond single-electron diffraction. *Structural Dynamics*, 1, 034303.
- [28] Feist, A., Bach, N., da Silva, N. R., Danz, T., Möller, M., Priebe, K. E., & Ropers, C. (2017). Ultrafast transmission electron microscopy using a laser-driven field emitter:

Femtosecond resolution with a high coherence electron beam. *Ultramicroscopy*, 176, 63-73.

[29] Aidelsburger, M., Kirchner, F. O., Krausz, F., & Baum, P. (2010). Single-electron pulses for ultrafast diffraction. *Proceedings of the National Academy of Sciences*, 107, 19714-19719.

[30] Kellenberger, E. (1990). Early Times of Electron Microscopy in Geneva (1944 to 1964). In *History of Electron Microscopy in Switzerland* (pp. 87-109). Birkhäuser Basel.

[31] Bostanjoglo, O., & Liedtke, R. (1980). Tracing fast phase transitions by electron microscopy. *Physica Status Solidi (a)*, 60, 451-455.

[32] Urban, K., Kabius, B., Haider, M., & Rose, H. (1999). A way to higher resolution: spherical-aberration correction in a 200 kV transmission electron microscope. *Microscopy*, 48, 821-826.

[33] Dömer, H., & Bostanjoglo, O. (2003). High-speed transmission electron microscope. *Review of Scientific Instruments*, 74, 4369-4372.

[34] LaGrange, T., Armstrong, M. R., Boyden, K., Brown, C. G., Campbell, G. H., Colvin, J. D., ... & Browning, N. D. (2006). Single-shot dynamic transmission electron microscopy. *Applied Physics Letters*, 89, 044105.

[35] Reed, B. W., LaGrange, T., Shuttlesworth, R. M., Gibson, D. J., Campbell, G. H., & Browning, N. D. (2010). Solving the accelerator-condenser coupling problem in a nanosecond dynamic transmission electron microscope. *Review of Scientific Instruments*, 81, 053706.

[36] LaGrange, T., Reed, B., DeHope, W., Shuttlesworth, R., & Huete, G. (2011). Movie mode dynamic transmission electron microscopy (DTEM): multiple frame movies of transient states in materials with nanosecond time resolution. *Microscopy and Microanalysis*, 17, 458-459.

- [37] LaGrange, T., Reed, B. W., & Masiel, D. J. (2015). Movie-mode dynamic electron microscopy. *MRS Bulletin*, 40, 22-28.
- [38] Park, H. S., Baskin, J. S., Kwon, O. H., & Zewail, A. H. (2007). Atomic-scale imaging in real and energy space developed in ultrafast electron microscopy. *Nano Letters*, 7, 2545-2551.
- [39] Baum, P., Yang, D. S., & Zewail, A. H. (2007). 4D visualization of transitional structures in phase transformations by electron diffraction. *Science*, 318, 788-792.
- [40] Carbone, F., Baum, P., Rudolf, P., & Zewail, A. H. (2008). Structural preablation dynamics of graphite observed by ultrafast electron crystallography. *Physical Review Letters*, 100, 035501.
- [41] Fu, X., Chen, B., Tang, J., Hassan, M. T., & Zewail, A. H. (2017). Imaging rotational dynamics of nanoparticles in liquid by 4D electron microscopy. *Science*, 355, 494-498.
- [42] Lorenz, U. J., & Zewail, A. H. (2014). Observing liquid flow in nanotubes by 4D electron microscopy. *Science*, 344, 1496-1500.
- [43] Vogelgesang, S., Storeck, G., Horstmann, J. G., Diekmann, T., Sivi, M., Schramm, S., & Ropers, C. (2018). Phase ordering of charge density waves traced by ultrafast low-energy electron diffraction. *Nature Physics*, 14, 184-190.
- [44] Danz, T., Domröse, T., & Ropers, C. (2021). Ultrafast nanoimaging of the order parameter in a structural phase transition. *Science*, 371, 371-374.
- [45] Olshin, P. K., Bongiovanni, G., Drabbels, M., & Lorenz, U. J. (2020). Atomic-Resolution Imaging of Fast Nanoscale Dynamics with Bright Microsecond Electron Pulses. *Nano Letters*, 21, 612-618.
- [46] Barwick, B., Flannigan, D. J., & Zewail, A. H. (2009). Photon-induced near-field electron microscopy. *Nature*, 462, 902-906.
- [47] Echtenkamp, K. E., Feist, A., Schäfer, S., & Ropers, C. (2016). Ramsey-type phase control of free-electron beams. *Nature Physics*, 12, 1000-1004.

- [48] Vanacore, G. M., Berruto, G., Madan, I., Pomarico, E., Biagioni, P., Lamb, R. J., & Carbone, F. (2019). Ultrafast generation and control of an electron vortex beam via chiral plasmonic near fields. *Nature Materials*, 18, 573-579.
- [49] Wang, K., Dahan, R., Shentcic, M., Kauffmann, Y., Hayun, A. B., Reinhardt, O., & Kaminer, I. (2020). Coherent interaction between free electrons and a photonic cavity. *Nature*, 582, 50-54.
- [50] Reinhardt, O., Mechel, C., Lynch, M., & Kaminer, I. (2021). Free-Electron Qubits. *Annalen der Physik*, 533, 2000254.
- [51] Dahan, R., Gorlach, A., Haeusler, U., Karnieli, A., Eyal, O., Yousefi, P., & Kaminer, I. (2021). Imprinting the quantum statistics of photons on free electrons. *Science*, 373, eabj7128.
- [52] Carbone, F. (2021). An electron walks into a quantum bar.... *Science*, 373, 1309-1310.
- [53] Kurman, Y., Dahan, R., Sheinfux, H. H., Wang, K., Yannai, M., Adiv, Y., & Kaminer, I. (2021). Spatiotemporal imaging of 2D polariton wave packet dynamics using free electrons. *Science*, 372, 1181-1186.
- [54] Kealhofer, C., Schneider, W., Ehberger, D., Ryabov, A., Krausz, F., & Baum, P. (2016). All-optical control and metrology of electron pulses. *Science*, 352, 429-433.
- [55] Ryabov, A., Thurner, J. W., Nabben, D., Tsarev, M. V., & Baum, P. (2020). Attosecond metrology in a continuous-beam transmission electron microscope. *Science Advances*, 6, eabb1393.
- [56] Cavalleri, A. (2018). Photo-induced superconductivity. *Contemporary Physics*, 59, 31-46.
- [57] Emery, V. J., Kivelson, S. A., & Tranquada, J. M. (1999). Stripe phases in high-temperature superconductors. *Proceedings of the National Academy of Sciences*, 96, 8814-8817.

- [58] Stojchevska, L., Vaskivskiy, I., Mertelj, T., Kusar, P., Svetin, D., Brazovskii, S., & Mihailovic, D. (2014). Ultrafast switching to a stable hidden quantum state in an electronic crystal. *Science*, 344, 177-180.
- [59] Zhang, J., Tan, X., Liu, M., Teitelbaum, S. W., Post, K. W., Jin, F., Averitt, R. D. (2016). Cooperative photoinduced metastable phase control in strained manganite films. *Nature Materials*, 15, 956-960.
- [60] Nakamura, M., Ogimoto, Y., Tamaru, H., Izumi, M., & Miyano, K. (2005). Phase control through anisotropic strain in  $\text{Nd}_{0.5}\text{Sr}_{0.5}\text{MnO}_3$  thin films. *Applied Physics Letters*, 86, 182504.
- [61] Chakhalian, J., Millis, A. J. & Rondinelli, J. (2012). Whither the oxide interface. *Nature Materials*, 11, 92-94.
- [62] McLeod, A. S., Zhang, J., Gu, M. Q., Jin, F., Zhang, G., Post, K. W., & Basov, D. N. (2020). Multi-messenger nanoprobe of hidden magnetism in a strained manganite. *Nature Materials*, 19, 397-404.
- [63] Humphries, S. (2013). Charged particle beams. Courier Corporation.
- [64] Williams, D. B., & Carter, C. B. (1996). The transmission electron microscope. In *Transmission electron microscopy*. Springer, Boston, MA, 3-17.
- [65] DuBridge, L. A. (1933). Theory of the energy distribution of photoelectrons. *Physical Review*, 43, 727.
- [66] Dowell, D. H., & Schmerge, J. F. (2009). Quantum efficiency and thermal emittance of metal photocathodes. *Physical Review Special Topics-Accelerators and Beams*, 12, 074201.
- [67] Strickland, D., & Mourou, G. (1985). Compression of amplified chirped optical pulses. *Optics Communications*, 55, 447-449.
- [68] Treacy, E. (1969). Optical pulse compression with diffraction gratings. *IEEE Journal of Quantum Electronics*, 5, 454-458.

[69] Bücker, K., Picher, M., Crégut, O., LaGrange, T., Reed, B. W., Park, S. T., Banhart, F. (2016). Electron beam dynamics in an ultrafast transmission electron microscope with Wehnelt electrode. *Ultramicroscopy*, 171, 8-18.

[70] Lorenc, M., Balde, C., Kaszub, W., Tissot, A., Moisan, N., Servol, M., Collet, E. (2012). Cascading photoinduced, elastic, and thermal switching of spin states triggered by a femtosecond laser pulse in an Fe (III) molecular crystal. *Physical Review B*, 85, 054302.

[71] Picher, M., Bücker, K., LaGrange, T., & Banhart, F. (2018). Imaging and electron energy-loss spectroscopy using single nanosecond electron pulses. *Ultramicroscopy*, 188, 41-47.

[72] Nicolazzi, W., & Bousseksou, A. (2018). Thermodynamical aspects of the spin crossover phenomenon. *Comptes Rendus Chimie*, 21, 1060-1074.

[73] Bertoni, R., Lorenc, M., Graber, T., Henning, R., Moffat, K., Létard, J. F. & Collet E. (2016). Cooperative elastic switching vs. laser heating in [Fe (phen) 2 (NCS) 2] spin-crossover crystals excited by a laser pulse. *CrystEngComm*, 18, 7269-7275.

[74] Bertoni, R., Lorenc, M., Cailleau, H., Tissot, A., Laisney, J., Boillot & Collet E. (2016) Elastically driven cooperative response of a molecular material impacted by a laser pulse. *Nature Materials*, 15, 606-610.

[75] Stoleriu, L., Chakraborty, P., Hauser, A., Stancu, A. & Enachescu, C. (2011). Thermal hysteresis in spin-crossover compounds studied within the mechanoelastic model and its potential application to nanoparticles. *Physical Review B*, 84, 134102.

[76] Krivokapic, I., Zerara, M., Daku, M. L., Vargas, A., Enachescu, C., Ambrus, C., & Hauser, A. (2007). Spin-crossover in cobalt (II) imine complexes. *Coordination Chemistry Reviews*, 251, 364-378.

[77] Bressler, C., Milne, C., Pham, V. T., ElNahas, A., van der Veen, R. M., Gawelda, W., & Chergui, M. (2009). Femtosecond XANES study of the light-induced spin crossover dynamics in an iron (II) complex. *Science*, 323, 489-492.

- [78] Auböck, G., & Chergui, M. (2015). Sub-50-fs photoinduced spin crossover in [Fe(bpy)<sub>3</sub>]<sup>2+</sup>. *Nature Chemistry*, 7, 629-633.
- [79] Grosjean, A., Négrier, P., Bordet, P., Etrillard, C., Mondieig, D., Pechev, S. & Guionneau, P. (2013). Crystal structures and spin crossover in the polymeric material [Fe(Htrz)<sub>2</sub>(trz)](BF<sub>4</sub>) including coherent-domain size reduction effects. *European Journal of Inorganic Chemistry*, 2013, 796-802.
- [80] Van Der Veen, R. M., Kwon, O. H., Tissot, A., Hauser, A., & Zewail, A. H. (2013). Single-nanoparticle phase transitions visualized by four-dimensional electron microscopy. *Nature Chemistry*, 5, 395-402.
- [81] Linares, J., Spiering, H., & Varret, F. (1999). Analytical solution of 1D Ising-like systems modified by weak long range interaction. *The European Physical Journal B-Condensed Matter and Complex Systems*, 10, 271-275.
- [82] Linares, J., Cazelles, C., Dahoo, P. R., & Boukheddaden, K. (2021). A First Order Phase Transition Studied by an Ising-Like Model Solved by Entropic Sampling Monte Carlo Method. *Symmetry*, 13, 587.
- [83] Enachescu, C., & Nicolazzi, W. (2018). Elastic models, lattice dynamics and finite size effects in molecular spin crossover systems. *Comptes Rendus Chimie*, 21, 1179-1195.
- [84] Enachescu, C., Stoleriu, L., Stancu, A., & Hauser, A. (2009). Model for elastic relaxation phenomena in finite 2D hexagonal molecular lattices. *Physical Review Letters*, 102, 257204.
- [85] Cailleau, H., Lorenc, M., Guérin, L., Servol, M., Collet, E., & Cointe, B. L. (2010). Structural dynamics of photoinduced molecular switching in the solid state. *Acta Crystallographica Section A: Foundations of Crystallography*, 66, 189-197.
- [86] Palluel, M., Tran, N. M., Daro, N., Buffière, S., Mornet, S., Freysz, E., & Chastanet, G. (2020). The Interplay between Surface Plasmon Resonance and Switching

Properties in Gold@ Spin Crossover Nanocomposites. *Advanced Functional Materials*, 30, 2000447.

[87] Hu, Y., Picher, M., Tran, N. M., Palluel, M., Stoleriu, L., Daro, N., Mornet, S., Enachescu, C., Freysz, E., Banhart, F. & Chastanet, G. (2021). Photo-Thermal Switching of Individual Plasmonically Activated Spin Crossover Nanoparticle Imaged by Ultrafast Transmission Electron Microscopy. *Advanced Materials*, 33, 2105586.

[88] Pavlik, J., & Linares, J. (2018). Microscopic models of spin crossover. *Comptes Rendus Chimie*, 21, 1170-1178.

[89] Félix, G., Mikolasek, M., Peng, H., Nicolazzi, W., Molnár, G., Chumakov, A. I., & Bousseksou, A. (2015). Lattice dynamics in spin-crossover nanoparticles through nuclear inelastic scattering. *Physical Review B*, 91, 024422.

[90] Ohkoshi, S. I., Tsunobuchi, Y., Matsuda, T., Hashimoto, K., Namai, A., Hakoe, F., & Tokoro, H. (2010). Synthesis of a metal oxide with a room-temperature photoreversible phase transition. *Nature Chemistry*, 2, 539-545.

[91] Ohkoshi, S. I., Tokoro, H., Nakagawa, K., Yoshikiyo, M., Jia, F., & Namai, A. (2019). Low-pressure-responsive heat-storage ceramics for automobiles. *Scientific Reports*, 9, 1-8.

[92] Rao, C. N. R., Ramdas, S., Loehman, R. E., & Honig, J. M. (1971). Semiconductor-metal transition in  $Ti_3O_5$ . *Journal of Solid State Chemistry*, 3, 83-88.

[93] Onoda, M. (1998). Phase transitions of  $Ti_3O_5$ . *Journal of Solid State Chemistry*, 136, 67-73.

[94] Mariette, C., Lorenc, M., Cailleau, H., Collet, E., Guérin, L., Volte, A., Trzop, E., Bertoni, R., Dong, X., Lépine, B., Hernandez, O., Janod, E., Cario, L., Ta Phuoc, V., Ohkoshi, S., Tokoro, H., Patthey, L., Babic, A., Usov, I., Ozerov, D., Sala, L., Ebner, S., Böhler, P., Keller, A., Oggenfuss, A., Zmofing, T., Redford, S., Vetter, S., Follath, R., Juranic, P., Schreiber, A., Beaud, P., Esposito, V., Deng, Y., Ingold, G., Chergui, M., Mancini, G. F., Mankowsky, R., Svetina, C., Zerdane, S., Mozzanica, A., Bosak,

A., Wulff, M., Levantino, M., Lemke, H., & Cammarata, M. (2021). Strain wave pathway to semiconductor-to-metal transition revealed by time-resolved X-ray powder diffraction. *Nature Communications*, 12, 1-11.

[95] Ould-Hamouda, A., Tokoro, H., Ohkoshi, S. I., & Freysz, E. (2014). Single-shot time resolved study of the photo-reversible phase transition induced in flakes of Ti<sub>3</sub>O<sub>5</sub> nanoparticles at room temperature. *Chemical Physics Letters*, 608, 106-112.

[96] Tokoro, H., Yoshikiyo, M., Imoto, K., Namai, A., Nasu, T., Nakagawa, K., & Ohkoshi, S. I. (2015). External stimulation-controllable heat-storage ceramics. *Nature Communications*, 6, 1-8.

[97] Liu, R., & Shang, J. X. (2012). First-principles study of thermal properties and phase transition between  $\beta$ -Ti<sub>3</sub>O<sub>5</sub> and  $\lambda$ -Ti<sub>3</sub>O<sub>5</sub>. *Modelling and Simulation in Materials Science and Engineering*, 20, 035020.

[98] Schick, D., Herzog, M., Bojahr, A., Leitenberger, W., Hertwig, A., Shayduk, R., & Bargheer, M. (2014). Ultrafast lattice response of photoexcited thin films studied by X-ray diffraction. *Structural Dynamics*, 1, 064501.

[99] Hakoe, F., Tokoro, H., & Ohkoshi, S. I. (2017). Dielectric and optical constants of  $\lambda$ -Ti<sub>3</sub>O<sub>5</sub> film measured by spectroscopic ellipsometry. *Materials Letters*, 188, 8-12.

[100] Mo, M. Z., Chen, Z., Li, R. K., Dunning, M., Witte, B. B. L., Baldwin, J. K., & Glenzer, S. H. (2018). Heterogeneous to homogeneous melting transition visualized with ultrafast electron diffraction. *Science*, 360, 1451-1455.

[101] Banhart, F., & Ajayan, P. M. (1996). Carbon onions as nanoscopic pressure cells for diamond formation. *Nature*, 382, 433-435.

[102] Banhart, F. (1999). Irradiation effects in carbon nanostructures. *Reports on Progress in Physics*, 62, 1181.

[103] Song, K., Schmid, H., Srot, V., Gilardi, E., Gregori, G., Du, K., & van Aken, P. A. (2014). Cerium reduction at the interface between ceria and yttria-stabilised zirconia and implications for interfacial oxygen non-stoichiometry. *APL Materials*, 2, 032104.

[104] Ben Hayun, A., Reinhardt, O., Nemirovsky, J., Karnieli, A., Rivera, N., & Kaminer, I. (2021). Shaping quantum photonic states using free electrons. *Science Advances*, 7, eabe4270.

[105] Scully, M. O., & Zubairy, M. S. (1997). *Quantum Optics*. Cambridge University Press.

**Publications:**

**Hu, Y.**, Picher, M., Tran, N. M., Palluel, M., Stoleriu, L., Daro, N., Mornet S., Enachescu C., Freysz E., Banhart F. & Chastanet, G. (2021). Photo-Thermal Switching of Individual Plasmonically Activated Spin Crossover Nanoparticle Imaged by Ultrafast Transmission Electron Microscopy. *Advanced Materials*.

DOI: 10.1002/adma.202105586

**Publications Under Preparation (preliminary titles) :**

Yaowei Hu et al., Size oscillations of individual spin-crossover particles after laser pulses

Yaowei Hu et al., Photoreversible phase transitions in individual Ti<sub>3</sub>O<sub>5</sub> nanocrystals studied by electron microscopy

**Conference Oral Presentations**

“Photoswitching of spin-crossover nanoparticles in an ultrafast electron microscope”, 17èmes journées de la matière condensée (JMC17); **Yaowei Hu**, Matthieu Picher, Marlène Palluel, Eric Freysz, Guillaume Chastanet, Florian Banhart, Rennes, France, 2021. (on-line)

“Photoswitching of spin-crossover nanoparticles in an ultrafast electron microscope”, Le Congrès des doctorants; **Yaowei Hu**, Matthieu Picher, Marlène Palluel, Eric Freysz, Guillaume Chastanet, Florian Banhart Strasbourg, France, 2021. (on-line)

## Microscopie électronique ultrarapide des états transitoires dans les nanomatériaux

### Résumé

Le projet de recherche de cette thèse est focalisé sur l'application de la microscopie électronique à transmission ultrarapide (UTEM) à l'étude des transitions de phase dans différents nanomatériaux. Des impulsions laser ultracourtes sont utilisées pour déclencher des transitions électroniques et/ou structurales, dont l'évolution temporelle est étudiée grâce à des impulsions électroniques ultracourtes. Grâce à cette méthode « pompe-sonde », le comportement de nanoparticules individuelles peut ainsi être étudié avec des résolutions spatiale et temporelle élevées pour évaluer le potentiel de ces matériaux en tant que photo-commutateurs rapides à l'échelle nanométrique.

Dans la première partie de la thèse, la dynamique d'élongation associée au changement de spin de nanoparticules à commutation de spin (dits « spin cross-over », SCO), déclenchée par impulsion laser, est étudiée avec une résolution nanoseconde. Il est démontré que la présence dans ces SCO de nanobâtonnets d'or plasmoniquement actifs permet d'augmenter l'efficacité et la vitesse de commutation de ces nanodispositifs. Dans la deuxième partie, il est question de transformations de phase induites par des impulsions laser dans des nanocristaux de  $Ti_3O_5$ . L'existence d'une bistabilité entre deux phases à température ambiante a permis une commutation réversible par impulsions laser.

Mots clés : matériaux à commutation de spin,  $Ti_3O_5$ , transitions de phase, microscopie électronique ultrarapide;

### Résumé en anglais

The research projects of this thesis are based on the applications of ultrafast transmission electron microscopy (UTEM) to the study of phase transitions in different nanomaterials. Ultrashort laser pulses are used for inducing electronic and structural transitions whose temporal evolution is studied with ultrashort electron pulses. The behaviour of individual nanoparticles is studied with high spatial and high temporal resolution to evaluate the potential of these materials as fast photoswitches at the nanoscale.

In the first part of the thesis, reversible length changes of spin-crossover (SCO) nanoparticles under laser pulses are studied with nanosecond resolution. Plasmonically active gold nanorods that are embedded into the SCO particles are found to increase the efficiency and to speed up the expansion process of SCO under laser pulses. In the second part, phase transformations in  $Ti_3O_5$  nanocrystals were induced by laser pulses. A bistability between two phases at room temperature allowed reversible switching between the phases with laser pulses.

Keywords : spin-crossover materials,  $Ti_3O_5$ , phase transitions, ultrafast electron microscopy